DISTRIBUTION AGREEMENT

Signature:

____ _______________________
Kazem V. Edmond Date

The Glass Transition: Rotational & Translational Decoupling and the Confinement Effect

By

Kazem V. Edmond
Doctor of Philosophy

Physics

Prof. Eric R. Weeks
Advisor

Prof. Stefan Boettcher
Committee Member

Prof. Connie Roth
Committee Member

Prof. Alberto Fernandez-Nieves
Committee Member

Prof. Victor Breedveld
Committee Member

Accepted:

Lisa A. Tedesco, Ph. D.
Dean of the James T. Laney School of Graduate Studies

Date

The Colloidal Glass Transition:
Rotational & Translational Decoupling and the Confinement Effect

By

Kazem Vafai Edmond
B.Sc., University of Massachusetts Amherst, 2004

Advisor: Eric Richard Weeks, PhD.

An abstract of
A dissertation submitted to the Faculty of the
James T. Laney School of Graduate Studies of Emory University
in partial fulfillment of the requirements for the degree of
Doctor of Philosophy
in Physics

Summer, 2011

Abstract

The Colloidal Glass Transition: Rotational & Translational Decoupling and the Confinement Effect

By Kazem Vafai Edmond

We study the microscopic properties of two phenomena related to the glass transition: the decoupling of diffusion from a glass-forming material's viscosity as it is cooled and the effect of confinement on the volume fraction that the glass transition occurs. We use colloidal suspensions of microspheres to physically model the glass transition. Colloids are a good approximation of hard-sphere fluids, where particle concentration effectively models a fluid's temperature. Using a high-speed confocal microscope, we rapidly visualize microscopic structural and dynamical processes in three dimensions.

We probe the colloidal fluid's rotational and translational dynamics with ordered clusters of microspheres. Far from the fluid's glass transition, both rotational and translational motion of the clusters are purely Brownian. However, in the liquid's supercooled regime, we observe a decoupling between the two types of motion: as the glass transition is approached, rotational diffusion slows down even more than translational diffusion. Our observation supports the notion that supercooled fluids are not merely fluids with large viscosities but that diffusion takes place by fundamentally changed mechanisms.

The effect of confinement on a fluid's glass transition temperature is the focus of our other experimental investigation. Confining a fluid to a small volume can either increase or decrease the glass transition temperature; in some cases confinement has no effect at all. The effect is strongly dependent on the properties of the boundaries confining the material. We directly observe the three-dimensional dynamical processes of confined colloidal suspensions of microspheres, while systematically varying the confinement volume and the suspension's concentration. The experiments find that confinement induces glassy behavior in a sample that is a fluid when not confined. Like particles in an unconfined near-glassy system, groups of particles in our confined system move together cooperatively. Normally these groups would be spatially isotropic. However, confinement induces a layering of the particles, which modifies the shape of the mobile groups so that they are more planar. The planar restriction helps to explain the sample's glassiness.

The Colloidal Glass Transition:
Rotational & Translational Decoupling and the Confinement Effect

By

Kazem Vafai Edmond
B.Sc., University of Massachusetts Amherst, 2004

Advisor: Eric Richard Weeks, PhD.

A dissertation submitted to the Faculty of the
James T. Laney School of Graduate Studies of Emory University
in partial fulfillment of the requirements for the degree of
Doctor of Philosophy
in Physics

Summer, 2011

Contents

Abstract Cover Page i
Abstract ii
Cover Page iii
Table of Contents iv
List of Figures vii
List of Tables ix
Citations to Previously Published Work x
Acknowledgments xi
Dedication xiii

1 Introduction 1
1.1 The Glass Transition 1
1.2 Fragile and Strong 2
1.3 Hard Sphere Model 3
    1.3.1 Fluid Phases 4
    1.3.2 Diffusion 4
    1.3.3 Dynamic Arrest and Cooperative Rearrangements 5
1.4 Summary of Major Results 5
1.5 Dissertation Structure Overview 6

I Background 8

2 Suspensions of Fluorescent Colloidal Particles 9
2.1 Introduction 9
2.2 Synthesis of Colloidal Particles 10
    2.2.1 Core-shell Particles 13
    2.2.2 Synthesis of Colloidal Clusters 16
2.3 Fluorescence 16

3 Confocal microscopy 21
3.1 Introduction 21
3.2 High Speed Laser Scanning 23

3.3 Instrumentation 24
    3.3.1 Scanning 25
    3.3.2 Light Filtration 28

II Methods 32

4 Sample Preparation and Data Acquisition 33
4.1 Colloidal Solvents 33
    4.1.1 Screening of charges 34
    4.1.2 Solvent Transfer 35
4.2 Bidisperse Suspensions 36
    4.2.1 Density-matching 38
4.3 Sample Chambers 38
    4.3.1 Wedge-Shaped Cells 39
    4.3.2 Rectangular Capillaries 41
4.4 Data Acquisition 41
    4.4.1 Resolution 42

5 Computational Analysis 46
5.1 Particle Tracking 46
5.2 Tracking Clusters 48
    5.2.1 Challis' Procedure for Coordinate Transformations 49
    5.2.2 Application to Colloidal Clusters 50
5.3 Analysis of Motion 51
    5.3.1 Mean Square Displacement 51
    5.3.2 Quantifying Noise 53
    5.3.3 Identification of Cage-Breaking Events 57
    5.3.4 Significance of Cage-Breaking 63

III Experimental Findings 64

6 Confinement 65
6.1 Introduction 65
6.2 Background 66
6.3 Experimental Methods 67
    6.3.1 Stuck Particles 69
6.4 Results 71
    6.4.1 Wall-induced structure 71
    6.4.2 Sample-averaged dynamics 75
    6.4.3 Confinement Length Scale 78
    6.4.4 Defining cooperatively rearranging regions 81

6.4.5 Hypothesized Behavior of Cooperatively Rearranging Regions 87
6.4.6 Shapes and Sizes of Cooperatively Rearranging Regions . . . 88
6.4.7 Dynamics Within Cooperatively Rearranging Regions 92
6.4.8 Conclusion 96
6.5 Influence of boundary roughness 97
6.5.1 Results 99
6.5.2 Conclusion 106

7 Rotational Diffusion 108
7.1 Introduction 108
7.2 Background 109
7.2.1 Rotational and translational diffusion 109
7.2.2 Colloidal glass transition 111
7.3 Sample preparation 112
7.4 Data acquisition 113
7.5 Tracking cluster trajectories 113
7.6 Mean square displacement and diffusion 114
7.7 Diffusive decoupling 118

8 Summary of Work and Outlook 125
8.1 Summary 125
8.1.1 The Confinement Effect 125
8.1.2 Rotational Diffusion 126
8.2 Impact and Outlook 126
8.2.1 The Confinement Effect 126
8.2.2 Rotational Diffusion 127

List of Figures

1.1 Cartoon schematic of dynamical heterogeneities. 2

2.1 Photograph of apparatus used for colloidal particle synthesis. 11
2.2 Schematic depicting self-assembly of ordered packings of microspheres. 15
2.3 Schematic of self-assembled clusters of various sizes. 17
2.4 Simplified Jablonski diagram, of fluorescent excitation and emission. . 18
2.5 Fluorescence spectra of a colloidal suspensions. 18
2.6 DIC and fluorescence micrographs of colloidal particles. 20

3.1 Schematic diagram of a confocal microscope's light-path. 22
3.2 Schematic of raster scanning apparatus of laser-scanning confocal. . . 26
3.3 Fluorescence spectra of two colloidal suspensions, compared to a filter. 30

4.1 Confocal micrographs of charged and screened colloidal particles. . . . 36
4.2 Schematic of wedge-shaped sample volume. 40
4.3 Diagrams of rectangular glass capillaries used for colloidal samples. . 41
4.4 Optical microscopy with and without immersion fluid. 43

5.1 Micrographs detailing particle tracking procedure. 47
5.2 Visualizations of a tetrahedral colloidal cluster. 49
5.3 Particle diffusing on surface of unit sphere. 55
5.4 Description of relationship between MSD plots and particle trajectories. 56
5.5 Distribution from pair correlation function. 60
5.6 Plots describing the IBS algorithm. 62

6.1 Confocal micrograph of particles at boundary. 71
6.2 Comparison of confined particles with Faxen's Law. 72
6.3 Particle number densities of stuck and mobile particles. 73
6.4 Particle number densities of particles at different thicknesses. 74
6.5 Plots of the MSD and non-Gaussian parameter for different thicknesses. 76
6.6 Plot of MSD for different samples for a number of thicknesses. 80
6.7 Particle number density and mobility between a narrow gap. 82
6.8 Particle number density and mobility between a wide gap. 83

6.9 Pair correlation distribution for number of thicknesses. 85
6.10 Diagram of three hypotheses regarding confinement experiments. . . . 87
6.11 Plots comparing dynamic time-scales and length-scales. 89
6.12 Three-dimensional renderings of the most mobile confined particles. . 90
6.13 Extent of mobile groups of particles. 93
6.14 Distributions of directions of particle displacements. 94
6.15 Images depicting stuck/immobile particles at boundaries. 98
6.16 Average particle mobility parallel and perpendicular to boundaries. . 100
6.17 Sketch of typical boundary conditions. 101
6.18 Particle mobility in terms of distance from stuck particles. 103
6.19 Images comparing relative roughness of boundaries. 104
6.20 Mobility gradients near rougher boundaries. 105

7.1 Visualizations of a tetrahedral colloidal cluster. 114
7.2 Translational and rotational trajectories of clusters. 116
7.3 Translational and rotational mobility for number of volume fractions. 117
7.4 Diffusion coefficients of tracer clusters. 120
7.5 Viscosity of monodisperse colloid for broad range of ϕ. 121
7.6 Comparison of translational and rotational displacements. 123

List of Tables

6.1 Characteristics of four confinement samples. 68
6.2 Thickness and small particle volume fraction for each data set. 79

Citations to Previously Published Work

Portions of Chapter 5 and Chapter 7 appear in the following manuscript, which has been submitted:

> “Tracking the rotational diffusion of colloidal clusters”,
> Gary L. Hunter, Kazem V. Edmond, Mark T. Elsesser, David J. Pine, and Eric R. Weeks,
> Submitted to *Optics Express*, Summer 2011
> arXiv:1107.2614v1 [cond-mat.soft]

Large portions of Chapter 6 have appeared in the following papers:

> “Colloidal glass transition observed in confinement”,
> Carolyn R. Nugent, Kazem V. Edmond, Hetal N. Patel, and Eric R. Weeks,
> *Physical Review Letters*, **99**(2):025702, 2007

> “Local influence of boundary conditions on a confined supercooled colloidal liquid”,
> K. V. Edmond, C. R. Nugent, and E. R. Weeks,
> *The European Physical Journal - Special Topics* **189**(1):83-93, March 2010

> “Influence of confinement on dynamical heterogeneities in dense colloidal samples”,
> K. V. Edmond, C. R. Nugent, and E. R. Weeks,
> arXiv:1003.0856, March 2010, to be resubmitted to *Physical Review E*

Large portions of Chapter 7 have appeared in the following paper and manuscript:

> “Large Core Shell poly(methyl methacrylate) colloidal clusters: Synthesis, characterization, and tracking”,
> Mark T. Elsesser, Andrew D. Hollingsworth, Kazem V. Edmond, and David J. Pine
> *Langmuir*, **27**(3):917927, February 2011.

> “Decoupling of Rotational and Translational Diffusion in Supercooled Colloidal Fluids”,
> Kazem V. Edmond, Gary L. Hunter, Mark T. Elsesser, David J. Pine, and Eric R. Weeks,
> In preparation, to be submitted Summer 2011.

Acknowledgments

Above all else, thanks for **Eric Weeks** for being an amazing advisor and mentor. Eric's optimism, sharp insight, unwaivering support, and dorky sense of humor made by six years better than I could have ever hoped. The quality of my work is the direct result of Eric demanding care and thoroughness at every step of the process. Also, he enthusiastically supported my pursuit of the rotational diffusion projects, helping me start a collaboration with **Mark Elsesser** and **David Pine** at NYU. This collaboration has resulted in strong personal and professional relationships with Mark and others at NYU, in addition to a post-doctoral position that I will start this fall. All of this is due to Eric's committed support, and for that I will be forever grateful.

My committee members, **Victor Breedveld**, **Alberto Fernandez-Nieves**, and **Connie Roth**, have been an incredible combination of mentors. Victor's good-natured scrutiny has kept me on my toes ever since handing him my PhD qualification proposal. His comments and criticisms have pushed me to develop a more thorough understanding of my experiments. Alberto's intense but boundless enthusiasm reminded me why we are in this business and inspired me to get that data, no matter what. Connie provided both scientific and professional guidance. That, and her optimism, always helped me maintain perspective on the fact that there is a life beyond graduate school.

I was very fortunate continue an experiment started by **Carrie Nugent**, so a thanks to her. By completing her initial work, leveraging my substantial experience with colloids, I was able to quickly get my own research underway in little time.

A thanks to **David Lynn**, for pushing me to be a better communicator, teacher, and scientist. David taught me that you don't always have to work so hard to get the best results.

Many thanks to **Jason Boss**, our lab's IT administrator. It always seemed like the smooth operation of our lab was in Jason's best interest. Being a thoughtful person, Jason was happy to learn the basics about our research in order to better serve our computational needs. The lab is always indebted to Jason's hard work.

Many, many thanks to **Gianguido Cianci**. Before he graduated from the lab, he endowed the rest of us with knowledge and experience that carried us forward for years, some still to come. He was the first person I met when I visited the Weeks Lab as a prospective, highlighting that it would be a great place to work. His advice, support, and hilarious jokes during my first few years here were a pleasure. I also greatly appreciate working with the amazing **Gary Hunter**, because without him my brain was stuck in neutral. Gary's focus, grounded nature, and profound insight served as an enormous catalyst in all of my work.

Finally, a big thanks to everybody who helped with their encouragement, support, and friendship. A special thanks to **Julie Coats**, who taught me how to never stop running, thunderstorms be damned. Thanks to **Kate Tomlinson**, for her patience, understanding, optimism and tireless support during these intense times. Also, I will never forget the support and devotion that I have received for the past nine years from **Angela "Murph" Huffaker**. She believed in me when no one else did.

Most importantly, thanks to my parents. Thanks to my father for inspiring greatness, in all things. Thanks to my mother for having faith in me, at all times.

Financial support for this research was provided by the National Science Foundation Grants DMR-0804174 and CHE-0910707, and also from the ORDER fellowship for teacher-scholars, organized by David Lynn.

Dedicated to my late father John,
my mother Massoudeh,
my brother Ramin,
and Buster the cat.

Chapter 1

Introduction

My research has focused on two specific phenomena of complex fluids: 1) the confinement effect and 2) decoupling between viscosity and diffusion. These seemingly disparate areas of research are actually fundamentally related in that they highlight the underlying nature of dynamical heterogeneities in supercooled glass-forming fluids. What follows is my dissertation, where I will introduce and discuss the scientific problems that were encountered and addressed by my work. In this brief introductory chapter, I provide some basic context for these problems and summarize the major results.

1.1 The Glass Transition

Glass, in basic terms, is a liquid that has lost its ability to flow. While behaving mechanically like a solid, glasses have an amorphous molecular structure that is indistinguishable from that of a liquid. How can this be? The answer to this question has been a major pursuit of physicists, chemists, material scientists, engineers for quite some time.

Since glass is being used almost everywhere, in a myriad of forms, working to understand its underlying physical behavior may seem like an arbitrary academic pursuit. In the physical sciences, however, ‘glass’ does not simply refer to window glass. Generally, the term ‘glass’ can refer to a much broader set of amorphous solids, including plastics and gels. Broader still, understanding the underlying physics of the transition from liquid to glass has diverse applicability in both science and technology. For example, the glass transition and its associated diffusive slowdown is critical in the preservation of foods, the suspension of desert insect life during drought, the stabilization of biochemicals, in the production of photovoltaics, the synthesis of advanced plastics or other composites, the production of optical fibers, and the fabrication of certain metallic alloys [1, 2].

Rapidly cooling some liquids results in the glass transition: the formation of a

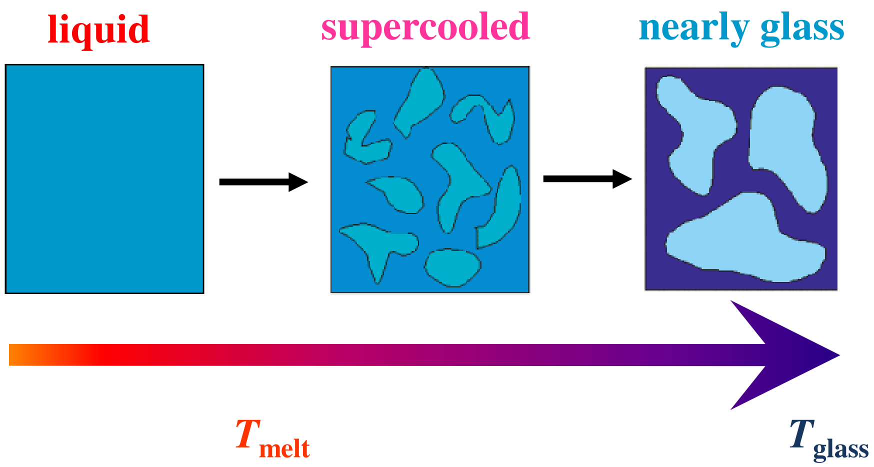

Figure 1.1: As a liquid is supercooled, molecules must move together in groups in order to diffuse or flow. Further cooling of the liquid reduces the thermal energy available to each molecule, requiring ever-larger groups to facilitate any kind of diffusive motion. The lighter colored blobs in each square signify cooperatively rearranging groups of molecules.

disordered solid from a liquid [1, 3–5]. Decreasing the temperature of the material below its melting point, so that it is supercooled, increases the viscosity smoothly but rapidly, however there is little apparent change in its microscopic structure [1, 3–9]. Since no structural mechanisms to explain this transition have been found, many explanations rely on dynamic mechanisms. Many theories use the concept of dynamical heterogeneities to explain the dramatic rise in the material's viscosity [10–15] The concept behind a dynamical heterogeneity is that for any one molecule to move, all molecules within the surrounding region must cooperatively facilitate this movement. As the liquid is deeply supercooled and the glass transition is approached, the size and duration of these regions grows, causing a rise in the material's viscosity [15]. A cartoon in Fig. 1.1 describes the concept of dynamical heterogeneity. While generally accepted, there are many details of this conceptual explanation that remain in debate [10–12]. The following dissertation discusses two investigations of the role of dynamical heterogeneities in glass forming systems.

1.2 Fragile and Strong

The glass transition of many materials is described as being "fragile" in that a small variation in temperature can result in a smooth but dramatic increase of viscosity. In contrast to the rapid rise in viscosity inherent to fragile glass formers is the more predictable increase in viscosity found in "strong" glass formers. Plotting a strong glass-former's viscosity in terms of temperature on a log-log plot would produce a very linear curve.

The linearity of strong liquids is indicative of a temperature-independent activation energy, meaning the energy required by a molecule to rearrange. The effective activation energy of fragile liquids increases as temperature decreases. At sufficiently low temperatures, molecular rearrangements can only be facilitated by the combined energies of cooperative rearrangements [2].

The work described here focuses specifically on fragile glass formers; colloids accurately model increased molecular crowding, where individual particles necessitate cooperative rearrangements with neighboring particles to undergo structural relaxation.

1.3 Hard Sphere Model

Dynamic molecular interactions within a liquid's bulk are inaccessible to experiments, meaning that any investigation of a material's microscopic behavior must be done with computer simulations or via physical model systems. Hard sphere models are one such physical system, exhibiting either crystalline or disordered structure in addition to its own glass transition, complete with dynamical heterogeneities. Particles in the hard sphere model, be they marbles, grains of sand, microscopic particles, etc., neither attract nor repel over greater distances than their diameter, but cannot interpenetrate. In other words, two hard sphere particles of radius a have an infinite repulsion if their center-to-center separation r is less than $2a$, but zero otherwise [16]:

$$U(r \leq 2a) = \infty \tag{1.1}$$

$$U(r > 2a) = 0. \tag{1.2}$$

Therefore, the free energy $U - TS$ is entirely driven by the particles' entropic contribution: the particles must move to increase their local free volume, maximizing the number of spatial configurations that they can occupy. The only control parameter in this system is the overall particle concentration, or volume fraction ϕ: the total volume of spheres divided by the total volume of the system. We say that temperature is modeled by ϕ, where a true hard sphere system is *athermal* since the actual temperature does not play a role.

Perhaps the most powerful examples of hard sphere systems are colloidal suspensions, where microscopic particles are dispersed in a liquid. Colloidal particles are large enough that they are directly observable via microscopy, but small enough that they exhibit Brownian diffusion. The random diffusion of the particles, in some ways, mimics the random diffusive behavior of liquid molecules. The colloid's liquid can be density-matched to the particles, negating motion due to sedimentation and focusing on purely diffusive interactions. The index of refraction of the liquid can also be matched to the particles', allowing direct observation of particle interactions deep within the sample's volume. Colloids were used in all of the work described here to carefully study the dynamical processes at play during the glass transition.

1.3.1 Fluid Phases

For $\phi \leq 0.49$, the hard sphere system is a fluid. For $0.54 \leq \phi \leq 0.74$, the equilibrium state of the system is a face-centered cubic (FCC) crystal. At a given ϕ, the system realizes higher configurational entropy when crystallized than when it is disordered. Crystals maximize the local available volume for all of the system's particles, therefore increasing the system's total number of spatial configurations. The maximum possible volume fraction is $\phi = 0.74$, the limit of close-packed spheres. A coexistence phase exists for $0.49 \leq \phi \leq 0.54$, where particles are free to exchange between crystalline and fluid domains, minimizing the system's free energy.

1.3.2 Diffusion

The dynamic processes of a hard sphere fluid are considered ergodic, where particles will traverse all points in a finite volume in a finite time determined by their rate of diffusion. Consider a particle in the dilute limit, where $\phi \sim 0$. The rate of translational diffusion of a spherical particle in an inviscid fluid is described accurately by the Stokes-Einstein-Sutherland equation:

$$D_{\mathrm{T}} = \frac{k_{\mathrm{B}} T}{6\pi\eta a}, \tag{1.3}$$

where a is the particle's radius, k_{B} is Boltzman's constant, T is the fluid's temperature, η is its viscosity, and D_{T} is the translational diffusion coefficient.

We can quantify the average distance displaced by particles using an ensemble-averaged mean-squared displacement (MSD):

$$\langle \Delta\vec{r}(\Delta t)^2 \rangle = \langle [\vec{r}(t + \Delta t) - \vec{r}(t)]^2 \rangle, \tag{1.4}$$

where $\Delta\vec{r}$ is the displacement vector of a particle over a time interval Δt, starting at some time t. The MSD grows monotonically for particles in a liquid. For particles at or near the glass transition, the MSD will plateau for the average period of time that particles remain caged, and upturn at the approximate time that cage-breaking tends to occur. Equations 1.3 and 1.4 are related as follows:

$$\langle \Delta\vec{r}(\Delta t)^2 \rangle = 6 D_{\mathrm{T}} \Delta t. \tag{1.5}$$

The details of these relationships will be discussed extensively in Chapter 5.

1.3.3 Dynamic Arrest and Cooperative Rearrangements

At higher particle volume fractions, well beyond the dilute limit, particles begin to crowd one another, effectively feeling one another's presence. If the nucleation of crystalline domains is avoided, the system appears to dynamically arrest and forms a solid at $\phi \approx 0.58$. The particles do not eventually crystallize, but remain disordered. In fact, the system is structurally indistinguishable from a liquid and frozen in place as a glass. We call this point the glass transition, denoted by T_{G} in molecular systems and ϕ_{G} in hard sphere systems.

Below the melting point, but before the glass transition, particles move together cooperatively over increasingly large dynamic length-scales. Cage-breaking events are the mechanism at the heart of cooperative rearrangements, where particles that comprise a cage must rearrange to allow a caged particle to displace. At higher densities, increasingly large numbers of particles must cooperate for these rearrangements to occur and therefore require greater periods of time to occur. The divergent dynamic length scales and time scales of these rearrangements indicates that supercooling a fluid does not simply increase its viscosity. Rather, the prevalence of cooperative rearrangements indicates a fundamental change in the nature of diffusion within the fluid.

Cooperative rearrangements in deeply supercooled samples, for $T_{\mathrm{G}} \leq T \leq 1.2\ T_{\mathrm{G}}$, can be as much as two orders of magnitude faster than what would be predicted by eq. 1.3, given the supercooled fluid's viscosity η. Such decoupling of translational diffusion from viscosity has been observed in molecular glass formers, computer simulations, and also colloids [10, 17]. A more subtle observation, however, has been that the rotational diffusion actually remains coupled to viscosity [10, 18]. Seemingly, the same dynamical heterogeneities that facilitate faster translational displacements do not have the same affect on rotational motion.

Here, we arrive at the work described in this dissertation, where we investigate two aspects of CRRs. First, we probe the dynamic length scales of supercooled colloidal fluids by confining them to volumes that are comparable to the size of their CRRs. Second, we study the rotational and translational diffusion of clusters of colloidal particles dispersed within dense colloidal suspensions.

1.4 Summary of Major Results

The following dissertation will present contributions to the understanding of 1) confinement of colloidal systems and 2) the decoupling between translational and rotational diffusion in colloidal supercooled fluids.

In chapter 6 of this dissertation, we show that confining dense colloidal suspensions between mostly smooth quasi-parallel walls induces glassy behavior for $\phi < \phi_{\mathrm{G}}$. The length scale over which the dynamic arrest is induced is the largest length scale ever observed in a colloidal suspension. We go on to demonstrate that roughness along the sample's boundary results in slower dynamics than along a smoother wall. Finally, we describe how the structural variations induced by confinement cause a change in morphology of the colloid's CRRs, providing an explanation for the early onset of glassy dynamics. The contents of chapter 6 are published as [19, 20]. Contents of this chapter also include substantial work that will be resubmitted for publication in *Physical Review E* [21].

In Chapter 7 we demonstrate that the rotational diffusion of colloidal clusters remain coupled to viscosity, even in deeply supercooled colloidal fluids, while the translational diffusion strongly decouples. The decoupling observed here is analogous to behavior observed in molecular glass formers. The cage-trapping dynamics inherent to translational motion are seemingly absent from the rotational motion of the clusters, providing insight into the underlying mechanics of diffusive decoupling. The work in Chapter 7 would not be possible without significant advances in colloidal synthesis made by Dr. Mark T. Elsesser and our other collaborators at the Center for Soft Matter Research at the New York University. Discussion regarding their work on the synthesis of colloidal clusters has been published in [22], where I contributed a small section demonstrating the capabilities of their materials. The rest, and majority, of the contents of this chapter have been drafted in a manuscript regarding the decoupling between translational and rotational diffusion of these clusters in dense suspensions. The manuscript has been read critically by my adviser Professor Eric R. Weeks and our collaborator Professor David J. Pine, but has yet to be submitted.

The following chapters also describe, in detail, the necessary technical developments that were necessary to complete these scientific investigations. Specifically, in Chapter 4 I discuss various difficulties encountered in sample preparation that are relevant to the experimental outcomes and the accuracy of our results. The various data analysis techniques used are discussed in Chapter 5.

1.5 Dissertation Structure Overview

The dissertation is organized into three major sections, or parts, each of which has two or three chapters. Part I, the Background, provides general background information on colloidal particles and fluorescence (Chapter 2) and confocal microscopy (Chapter 3).

Most of Chapter 2's contents, which describes the protocol for the synthesis of monodisperse colloidal particles made of poly(methyl methacrylate) (PMMA), were either included in a packet used at a University of Michigan workshop on colloidal synthesis or published, with significant improvements, in Ref. [22]. The contributions made by Ref. [22], including the synthesis of core-shell particles and colloidal clusters, are discussed in some detail. Most of the original work regarding particle synthesis was accomplished by collaborators at the New York University's Center for Soft Matter Research (NYU, CSMR). These techniques were critical to the successful completion of the experiments in Chapter 7, and are therefore worth discussing. In addition, I have developed in-depth knowledge of colloidal synthesis, having produced colloid used by my colleagues and my work with them, although this work is not discussed here. A general discussion regarding colloidal synthesis protocols is provided. The final section of Chapter 2 provides a detailed discussion about fluorescent dyes and their use in optical microscopy and how they are used to label colloidal particles. Chapter 3 will provide general background information regarding confocal microscopy. Specifically I focus on laser-scanning confocal microscopes, and how they are able to achieve the high acquisition rates required to observe dynamical processes.

Part II focuses on the various technical methods used to complete the work presented here, including both experimental techniques (Chapter 4) and methods of computational analysis (Chapter 5). For example, a methods paper I am working on with Gary L. Hunter, where we describe how to track the rotational diffusion of colloidal clusters, is being drafted and will be submitted soon [23]. We will most likely submit it to *Optics Express*.

The scientific contributions made by my work are discussed in Part III. We find that confining dense colloidal suspensions induces a glass transition, where cooperatively rearranging groups of particles exhibit unique morphologies, becoming planar in shape (discussed in Chapter 6). In our investigations of rotational diffusion, we find that the rotational diffusion of colloidal tetrahedral clusters remains closely coupled with the colloid's viscosity as ϕ_{G} is approached. The cluster's translational diffusion, however, decouples from the fluid's viscosity (discussed in Chapter 7).

Part I

Background

Chapter 2

Suspensions of Fluorescent Colloidal Particles

Dispersions of microspheres in a fluid phase, a colloid, have been used to serve as a good approximation of the hard-sphere model, showing a fascinating variety of complex phase behavior that can mimic that of simple atomic liquids and solids. To date, the most popular class of colloid to serve this purpose have been poly(methyl methacrylate) (PMMA) microspheres suspended in mixtures of organic solvents that have been index- and density-matched to the PMMA. While conceptually simple, colloid of this type have inherent complexities that must be taken into consideration to produce consistent and reliable results. Recent focus on this area, from researchers in the physical sciences and chemical engineering, have helped to address these concerns and further increase the complexity and utility of these systems.

2.1 Introduction

For decades, scientists and engineers have studied the structure and assembly of materials formed from colloidal suspensions of isotropic, spherically shaped particles. The ability to synthesize large quantities of pure highly monodisperse particles has led to great insight into the structure and dynamics of simple atomic systems. Pusey and van Megen first mapped the phase diagram of hard-sphere colloids using refractive index-matched suspensions of sterically stabilized poly(methyl methacrylate) (PMMA) spheres [24]. With the emergence of high speed confocal microscopy [25, 26], discussed in the next chapter, colloidal systems can be directly visualized in three dimensions to study dynamic phenomena such as the glass transition [17] and crystal nucleation [27].

While colloidal dispersions with myriad shapes and properties have been produced, only dispersions of sterically stabilized PMMA microspheres in mixtures of organic solvents have been able to meet the stringent requirements of a fully visualizable three-dimensional hard-sphere model. Organic solvents can be index- and density-matched to PMMA, the particles can be fluorescently labeled, and undesirable charge interactions can be minimized [28], if not eliminated altogether [29]. Colloidal microspheres can be self-assembled into complex shapes [30, 31] and highly ordered packings [22, 32]. The aim of our work is to model and visualize hard-sphere phase behavior in three dimensions, specifically focusing on cooperative particle rearrangements in addition to the reorientation of individual packings of microspheres.

2.2 Synthesis of Colloidal Particles

Through my own research and experiences, I have developed an in-depth knowledge of the colloidal synthesis process. I have used a number of different techniques to synthesize monodisperse suspensions of PMMA microspheres, stabilized with polyhydroxystearic acid (PHSA). Generally, each technique is a variation of the same basic procedure and protocol, which I provide in general terms below in order to help familiarize the reader with the process. I have synthesized a number of different batches of colloid, which have been routinely used by my colleagues for their own experiments. While I collaborate with them on a few of these experiments, none are reported here. That is, none of the results discussed in Chapters 6 and 7 used particles that I synthesized.

Due to their nearly hard-sphere-like pair potential, concentrated suspensions of PHSA-stabilized PMMA microspheres have been used extensively for academic studies of their structure, dynamics, and phase behavior [24]. Without the PHSA stabilizer, the PMMA particles would have a higher affinity for one another due to van der Waals attraction, meaning the particles would rapidly aggregate. The PHSA can be imagined as a short layer of polymer chains that stick out from the surface of the PMMA sphere, similar in scale to the fuzz covering a tennis ball. However, the PHSA is not adhered to the bead's surface like some sort of coating.

The PMMA particles themselves are, generally speaking, a very long polymer chain. When dispersed in an immiscible solvent the chain compresses into a spherical random coil in order to minimize its exposure to the solvent, having a higher affinity to itself. Therefore, the desirable architecture of a colloidal particle's stabilizer consists of randomly incorporated side chains that have an affinity for the dispersion medium, which are chemically attached to an anchor polymer. The insoluble anchor polymer tends to associate with the PMMA chain's backbone via physical adsorption or formation of a covalent bond. The geometry of PHSA side chains across the PMMA is referred to as a "comb-graft" copolymer, and they serve as effective steric stabilizers and are necessary for the synthesis of monodisperse colloidal microspheres.

A protocol for reliably producing sufficient quantities of PHSA was not widely known until 2006, when a workshop was held at the University of Michigan, where the synthesis procedure for PHSA and PMMA colloid was demonstrated. Even then,

Figure 2.1: Photograph of flask and condenser used to polymerize methylmethacrylate into coiled, spherical polymer chains. The sample is bright pink because it is saturated with fluorescent dyes, guaranteeing homogenously dyed, bright fluorescent spherical particles.

the procedure to produce the PHSA required 2-3 days to complete and produced very inconsistent results, working only half of the time under the best of conditions, and each successful batch would produce colloidal particles with different levels of stability and types of electrostatic interaction. Additionally, the particle synthesis procedure required several involved steps and took almost 24 hours to complete.

Recent publications in 2010 [33] and 2011 [22] by my collaborators in the Center for Soft Matter Research at NYU significantly improved matters, however. Their method reliably produces abundant amounts of PHSA stabilizer–about a liter–in addition to a protocol for the synthesis of highly monodisperse PMMA microspheres, the latter of which can be completed within a single afternoon of work. Of note, a similar method for synthesizing colloidal particles of this type is explained in Ref. [34], significant for their use of a dye that is optimal for use in confocal microscopy. The method used in Ref. [34] is a modified version of Ref. [35], which is heavily cited.

Very briefly, I would like to outline the steps of a typical particle synthesis procedure here. The steps here are simply to give the inexperienced reader a rough idea of what to expect during a typical particle synthesis procedure. For actual details and methods, please see Refs. [34], [36] or [22].

1. Add solvent mixture, by mass, into a flask.
2. Add and dissolve stabilizer (PHSA in our case) to the solvent mixture.
3. Set up the flask, oil bath, and vapor condenser. Example shown in Fig. 2.1.
4. Heat mixture for some period of time: the period of time varies with procedure.
5. Prepare separate solution of monomers with dye and other required chemicals.
    - Methylmethacrylate (MMA), for example, are monomers of PMMA.
6. Add monomer solution to heated flask of solvent mixture.
7. React for 2 hours, inspect product under microscope for spherical particles.
8. Wash product, replacing supernatant with a pure solvent.
9. Return product to the reaction flask.
10. Raise temperature and add a chemical catalyst.
    - Temperature and catalyst serves to lock PHSA to PMMA backbone.
11. Cook for 2 hours, then cool for 2 hours.
12. Clean particles **thoroughly**.

Charge interactions between particles are a common occurrence for both aqueous and organic solvent based colloids. Through the measured addition of ionic salts these interactions can be carefully tuned, or even screened away completely [28, 37]. Section 4.1 features a more in-depth discussion of the role of ions and solvents.

Typically, PMMA microspheres are dispersed in solvents that are immiscible with PMMA, meaning that the particles absorb very little of the solvent and therefore swell very little. We say that these are poor solvents for PMMA, and in these types of samples the random coil configuration of the particle is adequate. However, dispersing the particles in a miscible solvent such as toluene or acetone, good solvents for PMMA, the particles will unravel and eventually dissolve. To prevent this, and retain a spherical shape even in a highly miscible phase, it is possible to cross-link the PMMA with itself. Imagine the PMMA particle as a tangled web of criss-crossing molecular strands, referred to as the polymer matrix. It is possible to use an additional cross-linking chemical element during the particle synthesis procedure that will covalently link these intersecting molecular strands within the polymer matrix. In a very good solvent like toluene, the spherical particle can swell by up to seven times its own diameter [38].

In the experiments described in this dissertation, Chapters 6 and 7, the solvent mixture is ∼85/15 (w/w) decahydronaphthalene (decalin, DCL) and cyclohexyl bromide (CXB). We add ionic salt, tetrabutylammonium bromide, to the solvent used in the rotational diffusion experiments of Chapter 7, which serves to screen the Coulombic interactions between the particles. See Chapter 4.1 for a more thorough discussion regarding solvents and salts. For the experiments described in Chapter 6, we used particles produced by Andrew Schofield (University of Edinburgh, UK). Multiple batches of colloid that I have made is routinely used in a significant number of experiments in our lab, but their results are not reported here. Mark Elsesser (New York University) made the particles that were used for the experiments discussed in Chapter 7. Some of M. Elsesser's particles were cross-linked, allowing them to be clustered, a procedure discussed in Sec. 2.2.2 and in Ref. [22].

Colloidal particles can be fluorescently dyed during or after the synthesis procedure, but in practice it is easiest to dye them during synthesis. Figure 2.1 is a photograph of flask, submerged in a heated oil bath, as it cooks the components that form PMMA-PHSA colloidal particles. A fluorescent dye known as Nile Red has been added to this solution, resulting in the bright orange color in this photo but is bright pink in reality. The solution's natural color is clear, becoming milky white as the particles form. Details regarding fluorescent dyes and confocal microscopy are discussed in section 2.3. Homogeneously dyed or blank particles will suffice for the vast majority of experiments. However, in certain situations, dyeing only the core of the particle is desirable, but has proven to be an exceedingly challenging and arduous procedure.

2.2.1 Core-shell Particles

A significant short-coming in optical microscopy is the poor resolution along the optical axis, usually defined as the z-axis of a Cartesian coordinate system (discussed in Chapter 3). In dense suspensions of fluorescently labeled particles, even microscopes with the highest optical and image resolutions may have difficulties distinguishing particles from one another. In some situations, as was the case with our confinement experiments (see Chapter 8), use of high resolution optics may not be an option. Deep within dense suspensions light will scatter, despite the very best index-matching efforts, giving separate particles that happen to be collinear with the optical axis a conjoined appearance. To work within these limitations, it is helpful to increase the perceived separation between particles by fluorescently labeling only the particle's core; a fluorescent microsphere surrounded by a non-fluorescent shell.

Successful synthesis of core-shell PMMA-PHSA particles has proven to be elusive. Their synthesis was first reported in 2003 [38] and again in a 2006 review [36] by the same authors. Reproduction of these type of colloid has proven to be very challenging.

Mark Elsesser, at NYU, developed a variation of this technique that is more easily reproduced [22]. The Elsesser technique works well, producing particles of sufficient size, stability and brightness, as demonstrated in Ref. [22] and again in Chapter 7.

Very briefly, I will describe the technique typically used to produce core-shell particles. Both Dullens [36, 38] and Elsesser [22] follow a standard particle synthesis routine (see section 2.2), but taking the additional step of cross-linking the particle's polymer matrix. A general description of cross-linking is described above, and there is a good paper discussing how to make cross-linked PMMA particles here [39]. Once cross-linked, subsequent steps are followed until a shell of non-fluorescent PMMA is "grown" onto the surface of the cross-linked cores. The cross-linking of the core is required as the subsequent growth steps occur in good PMMA solvents, which would dissolve or otherwise damage the core. The entire procedure can be very arduous and has been known to reduce the brightness of the fluorescent dye.

It is important to note that all core-shell synthesis methods to date are very limited in the type of fluorescent dyes that they are compatible with. The restriction is due in part to the electrostatic charge of fluorescent dyes and details involving the various chemical interactions of the procedure. The limitation on dyes is in addition to the already limited number of fluorophores that work with organic solvents.

As an abstraction of material structure and dynamics, the hard-sphere model continues to provide a wealth of information, especially regarding glass forming materials. However, molecules are not spherical in shape. While taking molecular anisotropies into account is not critical for a certain level of fundamental understanding, experiments that did so would produce a wealth of complex dynamic phenomena and rich phase behavior. In a way, anisotropic particles, such as ellipsoidal rods, clusters, and other shapes could extend aspects of the hard-sphere model into new areas [40]. Of these shapes, dense packings of microspheres, or clusters, are perhaps the most compatible with existing methods: their size, shape, and behavior are similar to suspensions of spherical particles, and the confocal imaging and tracking of fluorescent spherical particles is well understood (see Chapter 6).

The formation of clusters is achieved via an emulsion drying technique, where a colloidal suspension of microspheres is emulsified with an immiscible aqueous phase, resulting in emulsion droplets containing some number of particles. The emulsion is heated so that the droplet phase evaporates, forcing the particles together so that their van der Waals attraction permanently binds them together. The process is depicted in the top of Fig. 2.2. The result is a colloid of ordered packings of colloidal microspheres, diffusing both translationally and rotationally. The novelty of this method is that the configuration of any n particles in a cluster is repeatable. For example, any cluster with $n = 4$ particles will be a tetrahedron The ordering of the clusters is a helpful feature when studying the dynamics of a single cluster type. A map of different cluster types and their confocal cross-sections, depicting the ability to clearly image them, is in Fig. 2.3.

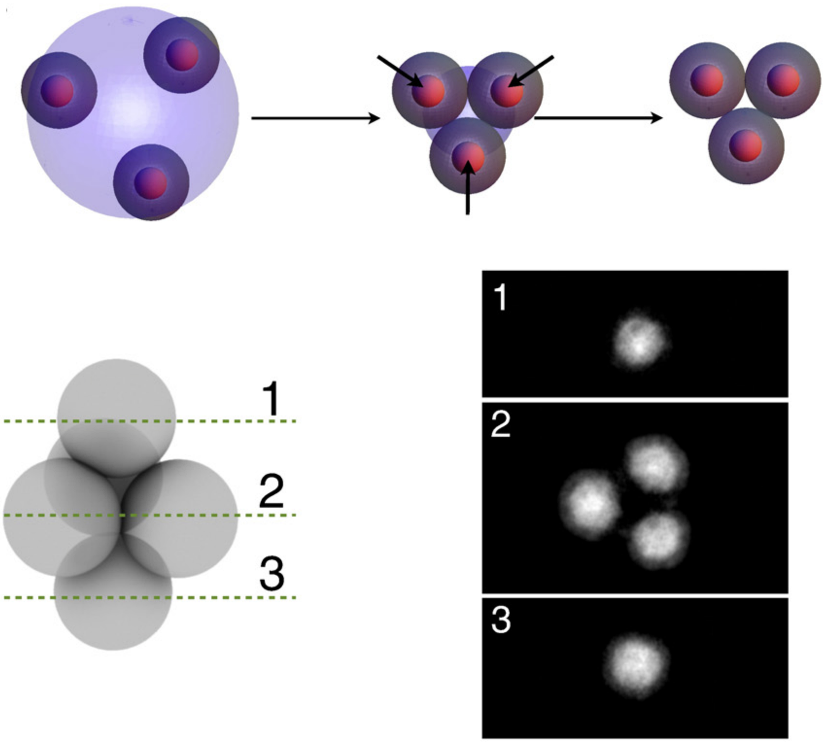

Figure 2.2: Schematic describing self-assembly of ordered clusters. Top, scheme illustrating the emulsion drying procedure used to prepare clusters from fluorescently, core-shell spheres. Below, experimental confocal images displaying three different ‘xy’ planes of a triangular dipyramid (pentamer) [22, 40].

2.2.2 Synthesis of Colloidal Clusters

A microscope's poor z-resolution, as mentioned in the prior section, in addition to fast dynamics can make it difficult to distinguish homogeneously dyed particles within a cluster from one another. It is advantageous to use core-shell particles instead, where the non-fluorescent shells provide several hundred nanometers of separation between the fluorescent cores within the cluster [22]. The increased image clarity afforded by core-shell particles made the experiments investigating rotational diffusion possible, discussed in Chapter 9.

2.3 Fluorescence

To image the colloidal particles used in our experiments, we label the particles with fluorescent probes, or dyes. Generally speaking, fluorescence is the emission of light by a substance that has absorbed light of a different wavelength. The process, as described in Fig. 2.4, relies on the energetic excitation of fluorescent dye molecules via the absorption of incident photons. An energetically excited dye molecule will release its energy via an emitted photon as the molecule returns to its energetic ground state, but not before losing a relatively small amount of energy via heat or some other energetic relaxation process. Having lost energy to this interim energetic relaxation step, the emission light has a longer wave-length than the excitation light, meaning that the emission light has red-shifted. The red-shift from excitation to emission light allows us to distinguish between the two; we view the sample via a filter that passes only light over the range of emission wave lengths. Unfortunately, for a population of identical dye molecules, there is a distribution of observed lifetimes: the time before excitations cease to render emitted photons. The decay in emissions is known as photobleaching.

The specific details of photobleaching are not relevant to the findings of this dissertation, only that it limits the duration of our experiments, so its specifics will not be discussed here. Note that in certain specialized experiments the reverse of red-shifting, blue-shifting, can actually occur [41]. Also worth noting is that fluorescence works with other kinds of electromagnetic radiation, but neither are relevant to our experiments and will therefore not be discussed here.

An optical micrograph of fluorescent colloidal particles is shown in Fig. 2.6. It may not be immediately apparent, when looking at the fluorescent micrograph on the right, that the process of fluorescent illumination is best described in terms of a series of probability distributions. However, it is after all a quantum mechanical process. There are finite probabilities that a given photon will be absorbed by a fluorescent dye molecule; that the molecule will be energetically excited by the photon; that the excitation will produce a fluorescent emission; that the emitted photon will be emitted in the direction of our eye-piece, camera, or detector. Plots of the excitation and emission distributions are shown in Fig. 2.5.

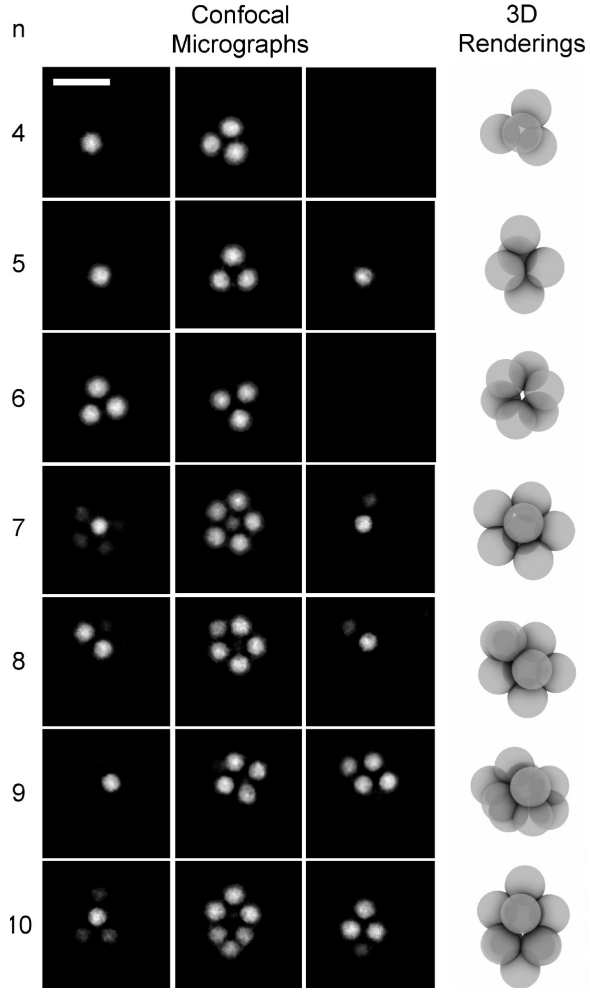

Figure 2.3: Spatially smoothed confocal micrographs displaying three different 'xy' planes of seven cluster types. The final column shows 3D renderings created using the coordinates of the clusters constituent particles determined via particle tracking algorithms. The particles' core-shell morphology makes it easy to distinguish individual particles within a cluster. Scale bar is 5 μm. This figure has been reproduced from Ref. [22].

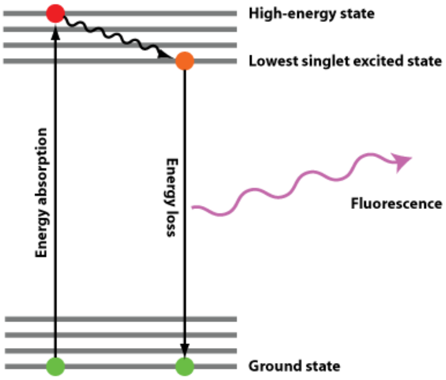

Figure 2.4: Excitation and emission distributions for a sample of fluorescently labeled colloidal particles. (This is temporary. I will relabel the axes, and make this more formal.)

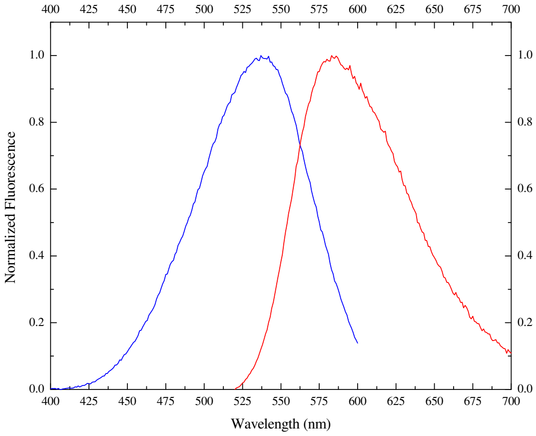

Figure 2.5: Excitation and emission distributions for a sample of fluorescently labeled colloidal particles. These fluorescent spectra were measured from a suspension of colloidal particles using a Horiba FluoroMax 4 fluorometer. The particles were $\sim$ 2.0 μm in diameter, dyed with Nile Red, and suspended in a mixture of index- and density-matched solvents.

The fluorescent spectra, used to produce the plots in Fig. 2.5, were measured from a fluorescently labeled colloidal suspension using a fluorometer. The fluorometer transmits light over a range of wavelengths in 1 nm increments, and then measures the excitation and emission response from the sample. The distributions on the left and right side of the plot in Fig. 2.5 describe the likelihood of fluorescent dye molecules being excited for a range of wavelengths of light and a corresponding distribution of probabilities that a given wavelength of light could be emitted, respectively. The peaks in the distributions tell us that this sample has the highest probability of being fluorescently excited by light with a wavelength of $\lambda_{\text{ex}} = 537\ nm$ and the highest probability of emitting light with a wavelength of $\lambda_{\text{em}} = 583\ nm$. These are the excitation and emission wavelengths, λ_{ex} and λ_{em} respectively.

Being distributions, the spectra give us an idea of how likely an excitation or emission is to occur. Instead of the normalized distributions, it is helpful to consider the original fluorescent spectra, where the area under the emission spectra represents the total number of emitted photons incident upon the detector. Therefore, for most colloidal experiments, it would be ideal for the separation between the excitation and emission spectra to be well separated. The more well-separated the spectra, the easier it is to distinguish between the two types of light and collect the broadest range of emitted light, providing the brightest and most well-defined images. The optical filtration process is discussed in detail in sec. 3.3.2.

There are two ways that we fluorescently label colloidal particles: 1) with a dye swelling procedure where the particles are swollen with a solution of dye and solvent that is miscible with PMMA or 2) by covalently binding the fluorescent probes to the PMMA backbone during the particle synthesis procedure [22]. Bonded probes are subsequently termed fluorophores. The dye swelling procedure is described in detail in Chapter 5. There are advantages and disadvantages to both dyeing techniques.

In our experience, dye swelling loads particles with appreciably more dye than using fluorophores alone. We speculated that the limited absorption of fluorophores is due to limited availability of space along the PMMA backbone. The PHSA stabilizer, as discussed in a prior section, occupies an appreciable amount of space along the PMMA chains. Additionally, there may be some kind of slight electrostatic repulsion between the anchored PHSA and the probes, since dye molecules are known to have some charge of their own.

As the name suggests, the dye swelling process works by swelling the particle in a good solvent, expanding the polymer matrix, allowing dye to diffuse within only to be trapped when the solvent is removed. The dye-swelling procedure is clearly explained in Ref. [25]. The particles used in Chapter 6 were dye-swelled with Rhodamine 6G. The core-shell particles, used for the work described in Chapter 7, were both dye-swelled and chemically labeled with RAS fluorophore.

Unlike fluorophores, which are physically bound to the polymer matrix, dye molecules that have been absorbed into the particle via a swelling procedure can "leak" into the outer phase. While leakage of dye has the obvious effect of making

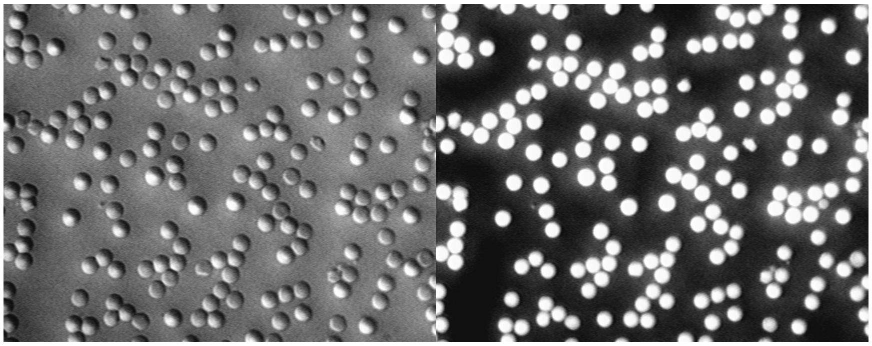

Figure 2.6: Left: Bright field DIC micrograph of 2 μm beads. Right: Fluorescent image of the same particles, same field of view.

the particles appear dimmer, the dispersion of the leaked dye into the outer phase is the most significant problem, producing fluorescent emissions throughout the sample. The resulting background emissions would mean that the contrast between bright white particles and black solvent is significantly reduced, substantially increasing the noise and systematic uncertainty of the experimental results. We “clean” the solvent of the leaked dye by replacing the solvent with new clear solution. A pair of optical micrographs are shown in Fig. 2.6, with a bright field image of colloidal particles on the left and a fluorescent image of the same particles on the right. Notice the high contrast afforded by fluorescence illumination.

Chapter 3

Confocal microscopy

Confocal microscopy is used to acquire high resolution, high contrast images of fluorescently labeled colloidal particles. Not only does use of this technique allow for visualizing particles deep within a sample, but also for the three-dimensional reconstruction of microscopic dynamical processes. The three-dimensional movies produced with this technique, paired with particle tracking algorithms, allow for an unrivaled level of understanding of structural relaxation processes in glassy systems.

3.1 Introduction

A confocal scanning optical microscope is a method of microscopic imaging that can be added to existing optical microscopy equipment. Confocal microscopy overcomes some of the key limitations of conventional wide-field fluorescence microscopy. With wide-field fluorescence microscopy, the entire volume of the sample within the beam path is illuminated at once. Thus, a significant number of the detected fluorescent emissions originate from portions of the sample volume that are out of focus, to the detriment of image clarity. In addition to being out of focus and not directly useful, these portions of the sample are photo-bleached over time.

The key feature of confocal microscopy is its ability to reject light from outside of the focal plane. Isolating the source of light to a thin slice within a volume, an optical cross-section, goes a long way toward reducing noise and producing images with both high contrast and high resolution. We collect series, or stacks, of cross-sections of a sample by scanning the microscope's focal plane through the sample's depth. The stack of cross-sections can be used to reconstruct a three-dimensional image of a given sample. The downside of accepting light from such a narrow region is a loss of pixel intensity or brightness, reducing the signal to noise ratio.

A schematic of a typical confocal is given in Fig. 3.1. The basic features are a light source, either a laser or high power lamp; a dichroic, a combination of a mirror and filter that reflects or passes certain ranges of light; and a pinhole aperture, which

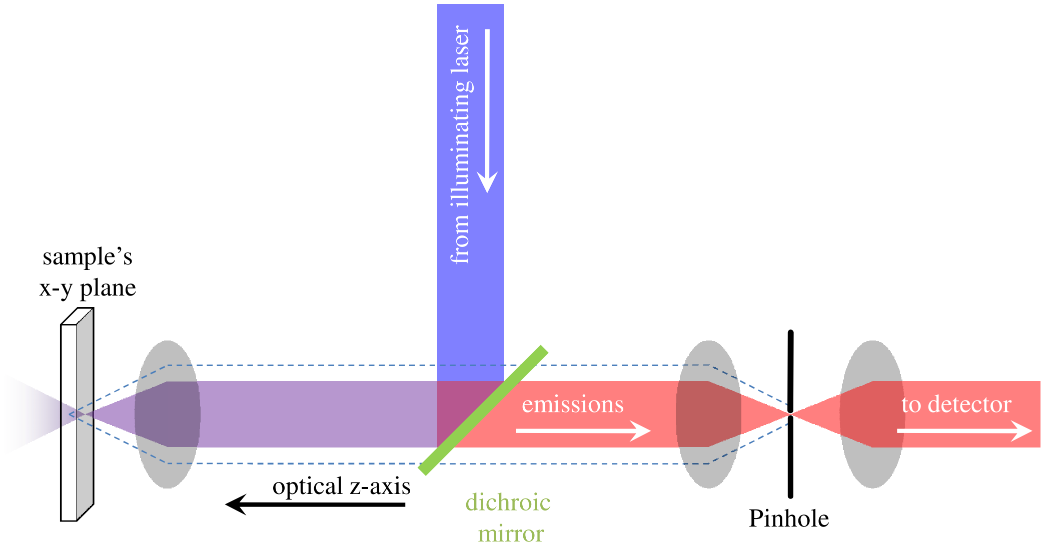

Figure 3.1: Schematic diagram of a confocal microscope. Laser light (blue) is reflected by the dichroic mirror and illuminates the sample at the focus of the microscope objective. The laser light excites a fluorescence emission, emitted as a longer wavelength of light (red). The emitted light passes back through the objective, passes through the dichroic, and then is focused to a pinhole. The pinhole rejects light that falls outside of the objective's focal plane, such as light along the dashed blue line.

blocks out of focus light from reaching the detector. The 'detector' can be a camera, a photo-multiplier, or just an eye-piece, depending on the type of confocal microscope. A convenience of confocal microscope systems is that they use traditional optical microscopes, so they usually augment existing systems.

There are two primary types of fluorecence confocal microscopes, "spinning disk" and "laser scanning", and there are a number of ways to implement each, all with their distinct advantages. Briefly, the spinning disk technique uses a pair of rotating disks that contain thousands of holes, where one set of holes serve to illuminate the sample in a series of concentric rings, and the other set serve as the confocal's pinholes. Spinning disk systems can use ordinary light sources, such as an arc-lamp, to illuminate the sample. It is therefore relatively simple to implement a spinning disk system within an existing optical microscope setup.

The laser scanning method is a radically different approach, where the light source is instead a laser that scans the sample over a series of parallel lines within each focal plane, a process known as raster scanning. The emitted photons are then "descanned" by the same optics that scanned the laser beam. The laser-scanning method was used for all of the image acquisition discussed in this dissertation.

3.2 High Speed Laser Scanning

The process of a laser-scanning confocal microscope (LSCM) is best understood by following the schematic in Fig. 3.1. We call the optical axis of the microscope objective the z-axis and the plane normal to this axis the x-y plane, or the focal plane. Light from a laser beam is reflected by a dichroic and focused with a microscope objective to a point within the sample's volume, somewhere along the x-y plane. In the event that the laser light is focused on some number of fluorescent probes, a portion of their fluorescent emissions may emit back toward and then through the microscope objective. As discussed in Sec. 2.3, the emitted photons have a longer wavelength than the laser light, which allows them to pass through the dichroic filter. Any reflected laser light is deflected by the dichroic. After passing the dichroic, the emitted photons are focused onto a point surrounded by a pinhole aperture that is confocal with the objective's focal point within the sample, before finally being absorbed by the detector.

The focused laser beam will have passed through and illuminated a significant portion of the sample before reaching the focal point. In a conventional optical microscope, the fluorescent emissions from these out-of-focus regions would manifest as blurriness in the acquired image. However, in a confocal microscope, the pinhole aperture blocks most light originating from beyond the focal point of the objective, so that only light originating from the illumination volume is detected. This ability of the confocal to produce clear images from deep within a sample is known as optical sectioning.

An image is produced by scanning the laser across the full area of the focal plane, providing a point-by-point reconstruction imaging of that particular cross-section of the sample. By repeatedly shifting the position of the focal plane and repeating the scanning process, and creating a stack of consecutive cross-sections, we can reconstruct a full three-dimensional image. Modern LSCMs can scan roughly 100 focal planes every second, binned into 256 by 256 pixels. Scanning approximately 100 such planes, each separated by 0.250 μm in the z-direction, an $80 \times 80 \times 25$ μm^3 volume can be acquired in roughly 1 second. The dimensions of the x-y plane naturally depend on the magnification of the objection and the size of the region being scanned.

To lend some intuition to the reader, a colloidal particle with a 1 μm radius takes on the order of ten seconds to diffuse its own diameter in clear open solvent, meaning that 1 second is sufficient to acquire an accurate three-dimensional trajectory describing the path it diffuses along. In a dense suspension of particles, where individual particle displacements can take on the order of 10 to 100 seconds, we consider 1 second to be a “real time” rate of acquisition.

3.3 Instrumentation

In this section I will discuss various mechanisms used by laser-scanning confocal microscopes to perform 1) the raster scanning of samples and 2) the filtration of light. As mentioned in the prior section, laser-scanning confocal microscopes are capable of acquiring hundreds of frames per second, depending on the image dimensions. For a rigorous understanding of experimental capabilities, sources of error, and just a general sense of appreciation for technology, it is critical to understand how confocal microscope systems are able to achieve such high standards.

Equally fundamental to the design and conducting of quality microscopy experiments, confocal or otherwise, is a working knowledge of the intricacies of light filtration. For example, the laser light that is used to excite fluorophores in a sample will reflect back toward the detector, along with the fluorescent emissions. Optical filters, of various complexities, are used to allow the detection of emitted light but the rejection of reflected light.

To learn significantly more about these topics than what is covered here, with purely a colloidal physics focus, I direct the reader to the “MicroscopyU” website, located at http://www.microscopyu.com. It serves as an encyclopedia of microscopy information, including full diagrams and interactive animated schematics. I have personally referred to it for my own understanding ever since 2002, when I first began using optical microscopes.

3.3.1 Scanning

In order to appreciate the high speeds of acquisition necessary for our experiments, it is worth considering the different ways of performing a scan with a confocal microscope. Generally, a confocal microscope scans an image, or frame, progressively in a bidirectional orientation, meaning that odd lines are left-to-right and even lines are right-to-left. Scanning a rectangular path in this way is often termed a raster scan, shown in the inset of Fig. 3.2.

The simplest means of completing a scan is by keeping the optics fixed, but translating the sample itself. Piezo actuators, and to a greater extent galvanometers, can be used to very precisely and repeatably move microscope stages by several nanometers in the x, y, and z directions. By moving the sample, instead of moving the optics to scan, the optical path can be highly optimized through the removal of specific optical distortions and aberrations. In this way, very high image quality can be achieved. However, scanning by translation of the sample is far slower than scanning the laser beam.

There are a number of ways to scan a beam, with variations of each method patented by various competing corporations. A simple and versatile technique uses two oscillating mirrors, controlled by galvanometers, to scan the beam in the x- and y-directions. The same mirrors "descan" the emitted photons, returning them to the detector, an elegant means of reconstructing the two-dimensional cross-section. Again, refer to Fig. 3.1 for a schematic of the confocal's beam path utilizing this method. Conventionally, the oscillation of the mirrors are controlled by a servo-controlled galvanometers that are driven with a linear saw-tooth control signal at the rate of several microseconds per pixel. The scanning speed of the galvanometers are limited due to inertia and, therefore, can only raster-scan a specimen at image acquisition rates that typically range from 1 to 5 images per second at standard frame sizes These acquisition rates are insufficient to properly observe the three-dimensional microscopic dynamical processes of colloidal systems.

To overcome these inherently slow speeds, advanced scanning scenarios have been devised by confocal manufacturers. One technique, employed by the confocal microscopes used to acquire data in our confinement experiments (see Chapter 6), is to replace one of the galvanometers with an acousto-optical device (AOD), a solid-state crystal that serves as a tunable diffraction grating. The angle over which the laser light is diffracted can be tuned with high frequency sound waves, thus used to scan across a one-dimensional line. With no moving parts, the AOD is capable of very fast speeds. In this scheme, the AOD rapidly scans the laser in x-direction, the galvanometer steps the laser down in the y-direction for the next row of pixels, and the AOD sweeps the laser back in the opposite direction completing the next scan. See the raster path in Fig. 3.2, keeping in mind that scans in the x-direction are significantly faster than in the y direction.

The trouble with this technique is that the AOD is a non-linear optical device,

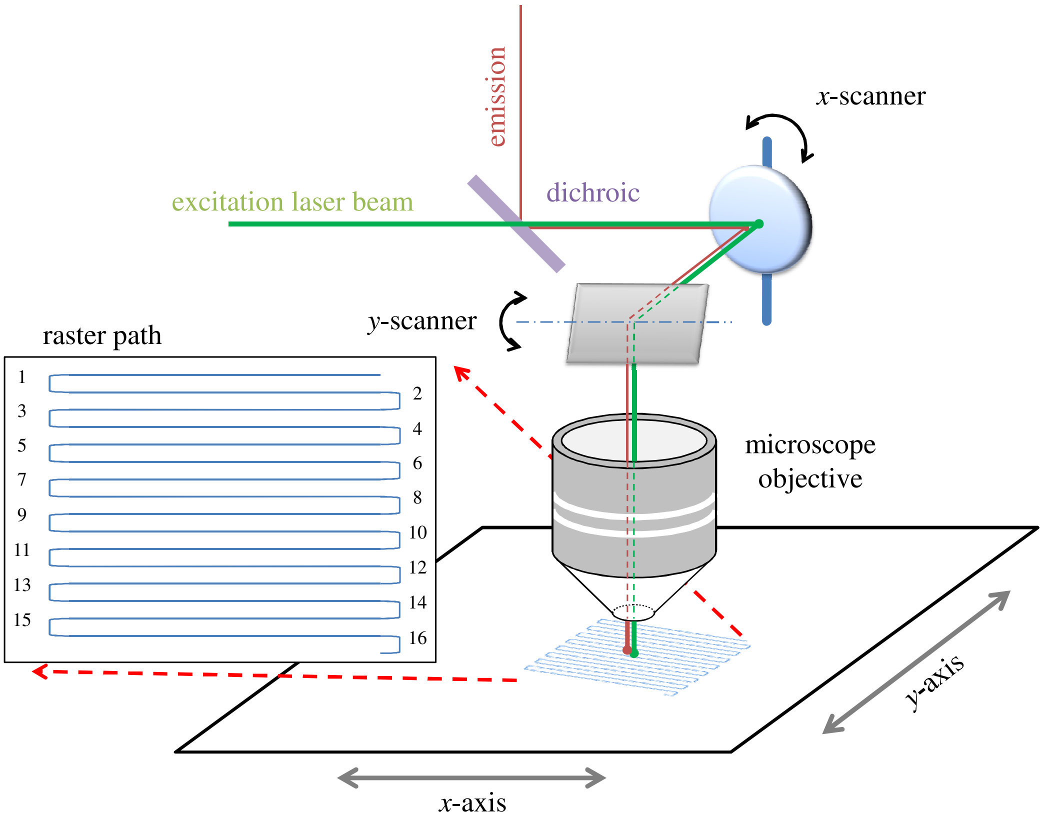

Figure 3.2: Schematic diagram of laser-scanning confocal. The inset details the raster-scanning pattern, with alternating row numbers. Typical frame dimensions in our experiments were 256 × 256 pixels, meaning 128 even and odd rows, and 256 columns. The x-scanner and y-scanner can both be operated in the same way, two galvanometers for example, or a galvanometer can be used to operate x while an alternative device, such as an AOD or resonant scanner, can be used for y. Not shown, typically the objective or the stage can be translated in the z-direction as well.

meaning that it cannot “descan” the emitted photons as can be done with the dual galvanometer technique. Therefore, the pinhole aperture used to reject out of focus light is actually a slit, not a symmetrical hole, which introduces an optical distortion to the detected light. The AOD scanner degrades the quality of the beam in additional ways, and the image quality correspondingly suffers. But for high speed image acquisition of micrometer sized particles, image quality is sacrificed for high speeds, which is somewhat acceptable for colloidal experiments where the particles are relatively large compared to λ_{ex}, and likewise produce a significant amount of fluorescent emission.

To achieve acquisition rates comparable to a video, without the distortions inherent to an AOD, the horizontal line scanning galvanometer can be replaced with a much faster resonant scanning galvanometer. The resonant scanners are the rotational equivalent of a tuning fork, where the energy stored in a torsion spring or rod assembly are used to oscillate a mirror sinusoidally. Scan rates of about 8,000 Hertz are used to acquire 512 lines, resulting in thirty 512×512 frames acquired per second. This type of scanning is found in the Leica Microsystems SP5 II confocal system, which was used to acquire the data for the rotational diffusion experiments (see Chapter 7).

Scanning in the z-direction

To acquire a series of optical cross-sections to perform a three-dimensional reconstruction, the focal plane must scan in the z-direction, along the optical axis. In a typical experiment the focal plane is shifted some distance, after the completion of a single raster scan. The subsequent raster is completed before the focal plane is shifted again, and so on. There are a number of factors worth discussing, warranting this separate subsection.

The primary distinction of scanning in the z-direction is weight. That is to say that sweeping a laser beam is done via small rapid motions of small mirrors. Shifting the focal plane requires the motion of either the microscope objective or the microscope stage, both of which are weighty objects prohibiting rapid sudden displacements.

A piezo-electric actuators can be used as stage for the microscope objective, capable of fine control of the objective’s position. Feeding electrical current into a piezo material changes its size in very small increments, usually accurate to about 10 nm. However, these materials do have a non-linear, often parabolic response to electrical current. As a result, piezo objective stages use sensors to gauge the amount of displacement. The use of sensors, however, does result in a sort of “shudder” when making rapid displacements. For example, an experiment could be scanning a volume that is $20 \times 20 \times 20$ μm^3 in size. When completing a 20 μm vertical sweep, the objective must make a sudden stop and change of direction, resulting in a “shudder” or rapid vibration in the objective. The amplitude of this vibration is on the order of 1 μm or less, but is significant enough to distort results. The vibrations can be avoided by slowing the scan rate, or simply waiting at the end of each scan, giving the piezo's sensors time to align.

Alternatively, a stage can be translated in all three directions, x, y and z, using galvanometric actuators. Galvanometers are exceedingly precise, providing very fine control of the amount and timing of displacements. In fact, galvanometers are used to position the read/write head of hard disk drives. Galvanometric actuators are an excellent means of shifting the microscope stage vertically in between rasters of each focal plane. Due to size and weight of the stage, these incremental shifts cannot be less than 200 nm in size. The relatively large step-size results in voxels shaped like rectangular prisms, rather than an ideal cube. Surely the dimensions of the raster or the objective's magnification can both be adjusted, producing voxels that are 200 nm cubes. However, doing so sacrifices pixel-resolution and possibly tracking precision in the horizontal plane, an issue discussed in Chapter 5.

It is true that the anisotropic nature of voxel sizes runs against the grain of typical colloidal experiments, where the samples are density-matched and the dynamics are stochastic and therefore generally isotropic over time: there is no "up" or "down". However, anisotropic voxels are accommodated when completing analysis of the acquired images. As long as the voxel dimensions are well defined, images can be recalibrated correctly. Admittedly, optical resolution along the z-axis is generally very poor, so in a sense stretched voxels are conforming to this and not exacerbating it to a significant extent. More often than not, clear vibration-free images acquired at a high rate trump anisotropic voxels.

In the interest of maintaining high acquisition rates, of paramount importance when observing dynamical processes, it makes sense to perform every odd z-scan in the reverse direction. Instead of taking the time to return the objective or stage to the starting point or "top" of the sample volume, the volume can be scanned in reverse. By doing a bidirectional z-scan in the same way that the raster does, illustrated by the inset of Fig. 3.2, the lag-time between stacks can be further reduced. However, while insignificant when raster scanning, a significant temporal shift is observed in the vertical scan of data. For example, acquisition of a $20 \times 20 \times 20$ μm^3 volume takes approximately 0.80 s with a high speed resonant scanner. Scanning in reverse therefore reverses this temporal shift, meaning that the stacks of data must be split into two separate data sets: one for even stacks and the other for odds. The lag-time between stacks is effectively doubled by doing this. The statistics acquired from each set can be averaged together. A discussion regarding the output of bidirectional scanning is including in Chapter 5.

3.3.2 Light Filtration

As depicted in Figs. 3.1 and 3.2, a simple dichroic is a single piece of treated glass that transmits all of the excitation light, but deflects the returning emissions. The dichroic serves as a filter, where light is either rejected or transmitted, depending on the wavelength of the light. The overwhelming majority of colloidal experiments discussed in the literature use this method.

It is possible to use more complex band-pass filters, or two different long-pass filters in rapid succession, to detect emissions from two different types of fluorescent dyes in the same sample. Multiple channels of light could be useful, for example, when studying colloidal suspensions containing multiple particle species: different shapes, sizes, interactions, etc. The use of multiple light channels is commonplace in microbiology, so modern confocal devices are well-suited for the task. However, in colloidal experiments that use organic solvents, finding dyes that are chemically compatible in addition to having uniquely defined fluorescence excitation spectra is a challenge.

Consider again our fluorescent distributions in Figs. 3.3(a) and (b). To detect fluorescent emissions efficiently, the fluorescent dye must be excited with minimal damage while collecting as much of the emitted light as possible. The excitation distribution tells us that peak fluorescent excitation occurs at $\lambda_{\text{ex}} \approx 537$ nm. Ideally, a laser with exactly this wavelength should be used. For some experiments, we use a 532 nm laser, indicated by the vertical green arrow in Fig. 3.3. By exciting the sample at this wavelength, each absorbed photon has the highest probability of inducing fluorescence, increasing the longevity of each fluorophore before photobleaching sets in. To make the most of each emission, we want to use a long-pass filter that collects the broadest range of emitted light as possible. Notice that there is minimal overlap between the distributions in Fig. 3.3(a) and most importantly the peak excitation just barely overlaps with the emission spectra. Therefore, a long-pass filter that transmits light with $\lambda \gtrsim 540$ nm is desirable.

In Fig. 3.3 we plot the transmission rates for one such filter in orange. The filter used in this case is of a particularly high quality: it has a very steep transition at ∼540 nm and transmits over 95% of incident light. The transmission curve of an ideal filter would be a simple binary step, from 0 to 100% transmission. Naturally, higher quality filters come at a higher financial cost.

However, if we consider two distributions that have significant overlap, the situation becomes more complicated. Figure 3.3(b) shows data from a different sample from (a). Two potential problems are immediately apparent from the distributions in Fig. 3.3(b). First, the excitation distribution overlaps significantly with the emission distribution. Second, the peak excitation wavelength falls within the distribution of wavelengths that the emitted photons are most likely to have.

We must choose a filter whose threshold falls as close to the laser's wavelength as possible, typically $7 - 10$ nm is considered a safe distance before some amount of scattered or reflected laser light will be transmitted. The peak emission wavelength is approximately 560 nm. Using a laser with a similar wavelength, for the most efficient fluorescence, would require the use of a long-pass filter that rejects a majority of the emissions. Using a 532 nm laser is much less efficient, but allows the use of a filter that transmits most of the emitted light. Optimal fluorescence imaging is often a

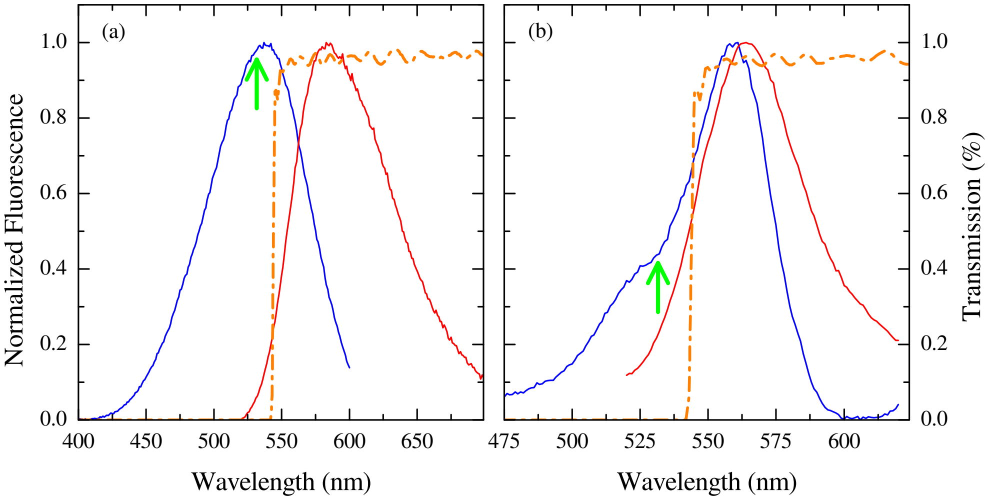

Figure 3.3: Fluorescence excitation and emission spectra with transmission percentage of long-pass filter. (a) Data for ∼2.0 μm PMMA colloidal particles, dyed with Nile Red. (b) Data for PMMA clusters from NYU, dyed with RSA dye. These fluorescent spectra were measured from a suspension of colloidal particles using a Horiba FluoroMax 4 fluorometer.

balancing act between optimal excitation and transmitting the most emitted light, however finding a good balance can sometimes become prohibitively expensive.

Solid-state lasers can be reliable, high quality, and affordable, but produce only a single wavelength of light. Likewise, optical light filters can be precise instruments, but their parameters are also fixed. Alternatively, both tunable lasers and tunable optical filters are both available options, but come at a high price. Tunable lasers can also be very expensive and not as reliable as solid state lasers. Tunable filters are sometimes included in advance confocal microscope systems, such as the Leica SP5 II, used to acquire the data in Chapter 7. Tunable filters use Fabrey-Perot interferometers, which produce multiple wave interference, serving as a variable band-pass filter.

Multi-Channel Fluorescence

The ideal fluorescent dye produces well-separated excitation and emission spectra. A catalog of dyes, the norm for the aqueous samples used in microbiology experiments, allows greater flexibility in the design of experiments. For example, in our experimental studies of the rotational diffusion of clusters amidst dense suspensions of individual particles (Chapter 7), it would be ideal for the clusters and particles to have separate excitation spectra. Multi-channel confocal systems are able to perform two raster scans using two different lasers, in rapid succession, before shifting the focal plane. In this way, two stacks of cross-sections are produced simultaneously, but of two different particle species that have been fluoresced independently from one another. During analysis, the data from each set can be recombined in order to understand structural and dynamical relationships between the clusters and surrounding particles.

Another example of experiments that would benefit from multi-channel fluorescence are those using suspensions of particles with multiple particle size distributions, where a unique dye would be used for each particle size. The confinement experiments, discussed in Chapter 6, used two different particle sizes in order to frustrate structural ordering. However, in order to accurately track the particles, only the larger species of particles were dyed. Observation of both particles, via two separate dyes, would have made a significant amount of valuable data available for more in-depth analysis.

As discussed in section 2.3, dye does tend to leak from particles and into the solvent. It is relatively common for dyes from different particle species to leak, be reabsorbed by different species, and produce mixed channels of fluorescence. In other words, fluorescing one channel would actually illuminate both species of particles.

Part II

Methods

Chapter 4

Sample Preparation and Data Acquisition

Careful preparation of samples is perhaps the fundamentally most important step of any series of experiments. Each sample must be prepared with care, because it is impossible in advance to know which one will produce the data that ends up being published. The discussion in Chapter 2 highlights the complexities inherent to colloidal systems, despite their relatively simple application as a hard-sphere model. Numerous factors are at play in most colloidal systems, including electrostatic interactions, organic chemistry, and issues with fluorescent dyes.

4.1 Colloidal Solvents

To visualize particles deep within dense samples, while also avoiding density gradients resulting from sedimentation, we use a mixture of solvents whose refractive index and density matches that of the PMMA particles. An added benefit of index-matching is that it minimizes interparticle attractions due to van der Waals forces, ensuring nearly hard sphere behavior. Various different solvent mixtures have been shown to work well with PMMA systems. The most common is a mixture of ∼85/15 (w/w) decahydronaphthalene (decalin, DCL) and cyclohexyl bromide (CXB). Similarly, cycloheptyl bromide (CHB) can be used instead of CXB. The CHB solvent is compatible with certain polymers used to induce depletion interactions, a topic not explored or discussed in this dissertation. CHB is also known to be less stable than CXB. Dry-cleaning fluid, tetrachloroethylene (TCE), can also be used in place of CXB or CHB.

While not used in the experiments presented in this dissertation, TCE is noteworthy in that it is induces a smaller charge than CXB and is much more stable [29]. Mixtures of TCE and DCL result in a very good approximation of hard-sphere behavior among PMMA particles. The one negative of TCE is that its consumption, even via the skin or inhalation, results in inheritable genetic defects. Studies have suggested that exposure to TCE can result in a nine-fold increase in developing Parkinson's disease later in life. As such, it is a solvent that must be used with extreme care, if at all.

Decalin comes in both *cis* and *trans* forms, where the *trans* form is energetically more stable. However, neither form of decalin should be considered structurally unstable and typically the *cis* form is used in our experiments. Decalin, either the *cis* or *trans* variation, is known to be a non-swelling solvent for PMMA particles. Its stability and inability to swell PMMA makes it a good solvent for storing colloidal particles in for an extended period of time.

Conversely, cyclohexyl bromide does slightly swell PMMA particles as it is slightly miscible with PMMA. Also, the carbon ring in CXB is unstable, resulting in separation of the Bromine ion. Bromine is yellow in color and this will often be apparent in fresh bottles of CXB, from Aldrich for example, which may have an amber tint. In its purest form, the CXB solvent induces a charge on the surface of the PMMA particles. Electrostatic interactions can be screened through the addition of ions to the solvent, further discussed in Sec. 4.1.1. In a way, the decay of CXB into bromine ions serves this purpose, screening the charge it itself induces on the particles. For better control of the solvent's ionic content, CXB is purified and then saturated with ionic salt.

Note that the breakdown of CXB to bromine is inevitable, but is greatly accelerated by exposure to light, high frequency noise or vibrations, and air. As such, samples should be stored in cool, dark, and quiet places. Also, to reduce exposure to air, the solvent should be stored either in an inert environment or under a nitrogen pad.

4.1.1 Screening of charges

As noted above and in Sec. 2.2, dispersing colloidal PMMA particles in CXB induces a surface charge. In addition, as noted in Sec. 2.3, fluorescent dye molecules themselves are charged in solvent, which can be due to the solvent's low dielectric constant and low concentration of free ions. While the interaction energy is weak, perhaps less than $k_B T$ in near contact, the repulsion length can be long, much greater than a particle diameter. Through the addition of ionic salts, we can screen these charge interactions to great effect. It is possible to tune the strength of the interaction by carefully adjusting the concentration of free ions in the solvent [37], but the aim of the experiments presented here was to approximate the hard-sphere model as closely as possible. To these ends, we saturate the solvents used in our rotational diffusion experiments, see Chapter 7, with ionic salts. The experiments on the confinement effect, see Chapter 6, did not use salt, but instead trace amounts of Bromine provide sufficient screening.

Despite its charge-screening effects, excess bromine should be removed from solvents prior to use for the sake of reliable and consistent experiments. The extent to which ions screen charge is known as the Debye length, whose measurement is described in the literature [42]. It is very useful to know, and subsequently be able to report, the Debye screening length between particles for a given experiment. Consider that the Debye length can shift the phase space of the hard sphere model; Dinsmore, et al. observed crystal nucleation for $\phi > 0.4$, which is below the hard-sphere freezing point of $\phi = 0.494$ [25]. It is not a minor thing to wave off.

Filtering the CXB through activated alumina is the best means of eliminating as many of the free ions as possible. Activated alumina can be difficult to acquire and also must be used in a glove box, an inert environment. Alternatively, in our experience, filtration via alumina oxide appears to do a good job of removing a majority of the bromine. An affective and popular ionic salt is tetrabutylammonium bromide (TBAB) [28]. The CXB solvent is not highly miscible with TBAB, therefore requiring roughly 24 hours of thorough mixing for full saturation. Any salt that is not absorbed floats to the surface and is removed prior to use.

Consider Fig. 4.1, which shows confocal micrographs of a suspension of ∼2.0 μm PMMA particles in a mixture of 85/15 (w/w) CXB/DCL. Figure 4.1(a) shows a colloid whose solvent has been filtered through alumina oxide, removing most of the bromine ions. As a result, the particles are charged and have a significant screening length, preventing hard-sphere-like behavior. The charge repulsion is evident in Fig. 4.1(a), where the particles are spaced roughly uniformly, almost as a lattice, with a spacing of roughly two particle diameters. Figure 4.1(b) shows an image of the same colloid, but the solvent in (b) has been saturated with TBAB. The TBAB ions screen the repulsive charge interaction between the particles, allowing the particles to sterically interact. In Fig. 4.1(b) we see far less order than in (a); many of the particles in (b) are very close to one another, almost touching in some cases. The interactions in Fig. 4.1(b) more accurately model a hard-sphere fluid.

4.1.2 Solvent Transfer

After synthesizing colloidal particles (see Chapter 2), we either stored them in an inert solvent, such as dodecane, or completely dried out and store as a powder. Dodecane is stable, does not swell the particles and does not induce particle aggregation. Particles can be stored for an indefinite period of time in dodecane. Alternatively, an advantage of working with powdered particles is the ability to accurately measure their mass, which can be used to determine a sample's solid particle volume fraction ϕ.

However, regardless of initial form, particles swell a significant amount when transferred to CXB. While not a good solvent for PMMA, CXB molecules will diffuse their way to within the PMMA polymer matrix to some extent, resulting in some amount of swelling. Thorough absorption of CXB significantly improves density- and index-matching, and is a critical step before initiating any experiment. Absorption of CXB

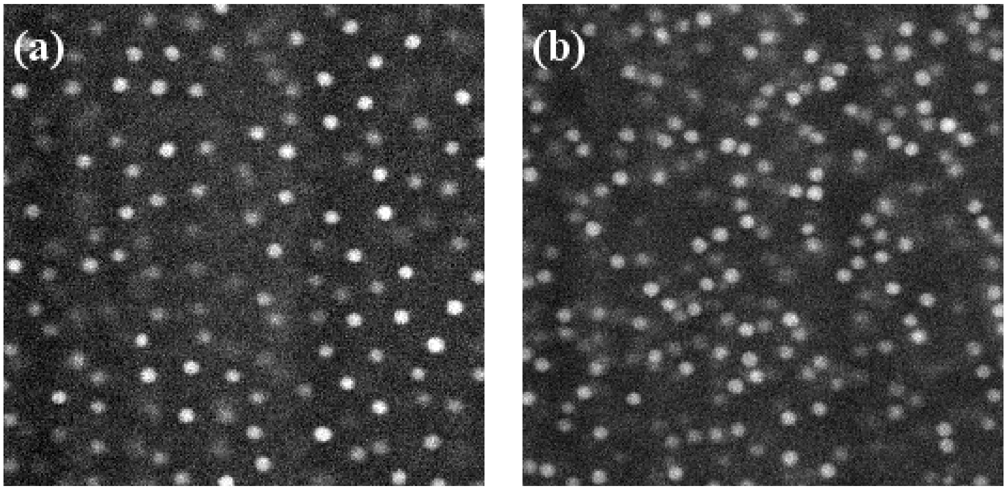

Figure 4.1: Confocal micrographs of a suspension of ~2.0 μm PMMA particles in a mixture of 85/15 (w/w) CXB/DCL. (a) The CXB solvent is pure, with a very low ionic content. (b) The CXB has been saturated with TBAB.

can be accelerated through heating the sample to $40 - 50^\circ\ C$, along with gentle mixing. L. Kaufman, *et al.* describe this procedure as a "heat-shock" to the particles; placing the colloid in an oven at $80^\circ\ C$ for several hours [43]. The particles used in Ref. [43] were not fluorescently dyed, however. We have observed that heating at temperatures greater than $60^\circ\ C$ can damage some fluorescent dyes.

As discussed in Sec. 2.3, fluorescent dye molecules will leak out from PMMA particles as they swell with CXB. The effect can be dramatic, giving the solvent phase a bright orange or red hue. To maintain high image contrast, where only the particles are fluorescently labeled, the dye-laden solvent must be thoroughly cleaned. Cleaning is achieved by repeatedly sedimenting the particles with centrifugation, removing the supernatant, and diluting with a fresh clear mixture of solvents and TBAB. It is best to prepare a large batch of TBAB saturated 85/15 solvent. The process can be repeated five to eight times over the course of a few days for the best effect. The aim is to get as much of the loosely absorbed dye out of the particles as possible so that there is minimal leakage during the course of an experiment.

4.2 Bidisperse Suspensions

Over time, dense suspensions of monodisperse particles will equilibrate by crystallizing, which is prohibitive to studying non-equilibrium fluid dynamics. Exacerbating this hurdle are the smooth glass slides and coverslips that are the sample's boundaries, which serve as a sort of template that readily induce crystallization. Therefore, it is particularly important to make all experimental observations far from sample boundaries. Typically, $30 - 40$ μm is considered a safe distance, but the deeper into the bulk the better. The better index-matched a sample, the deeper the particles can be imaged.

Mixing the sample immediately prior to experiments can break up crystallites. We can seal a small piece of wire within the sample chamber and use it to shear and mix the colloid using a strong external magnet. Depending on polydispersity and the value of ϕ, it can take some time for crystallites to reform. Recent work studying particle dynamics of deeply glassy systems has found that polydisperse particle size distributions, say greater than 10% [44], can be a very effective means of delaying crystallization for months, while still effectively modeling a hard-sphere fluid. Additional studies of colloidal particle dynamics in glassy bidisperse suspensions, with a particle size ratio of approximately 3 to 1, found that smaller particles act to "lubricate" the structural rearrangements of the larger particles [45, 46].

In our confinement experiments, discussed in Chapter 6, the close proximity of the sample boundaries posed a significant problem. The range of confinement thicknesses reached down to a single particle diameter, where crystallization is virtually guaranteed [47–50]. To frustrate crystallization, we use a binary distribution of particle sizes: approximately 1.18 μm and 1.55 μm in radius, with equal volume fractions of each [19–21]. A small size ratio can make visually distinguishing the two species a particular challenge, but depending on the experiment, differentiation may not be necessary.

When preparing a bidisperse suspension, the number ratio between two species can be defined by measuring each component's mass. Since the colloid is density-matched, mass and volume ratios are equivalent. Naturally, the mass of both species can most directly be determined when both are a dry powder. Comparing the mass between two dispersions, however, is only useful if the solvent mixture of each is completely identical.

For our rotational diffusion experiments, our particles were totally dried out, having the consistency of confectionery sugar. Being dry, it was relatively easy to accurately mass both particle species. A large batch of TBAB saturated 85/15 (w/w) CXB/DCL solvent mixture was prepared, added to a vial, and then carefully massed. We then gradually dispersed the dried particles into the solvent and then thoroughly stirred the dispersion while slightly heating it in order to accelerate absorption of solvent. The dried particles swelled in size significantly, by roughly 20% in volume. It is important to add excessive solvent in order to allow for swelling and proper dispersion.

The colloid in our confinement experiments were already dispersed in clean, density-matched 85/15 solution. To produce roughly equal ϕ of each, we visually counted particles in dilute dispersions with the aid of particle tracking software, and added one species or the other accordingly.

4.2.1 Density-matching

In reality, the 85/15 mass ratio of solvents is a close approximation of a PMMA density-matched solution. The actual solvent ratio necessary to density-match the suspension can vary with temperature. Also, different batches of PMMA particles will absorb different amounts of CXB. Both contribute to variations in density, and can be addressed through addition of the appropriate solvent.

For example, if after a brief period of centrifugation the particles sediment, we add some relatively small volume of CXB, and centrifuge for a longer period, and continue until adequate density-matching is achieved. Standard centrifuges may rise in temperature after roughly $20 - 30$ minutes of continuous operation. As mention above, temperature changes the miscibility of CXB with PMMA, and will therefore change the effective difference between solvent and particle densities. It is best to use a temperature-controlled centrifuge, set to whatever temperature the experiment will be conducted at. Ideally, the microscope stage itself should be temperature controlled as well, particularly for experiments lasting multiple hours.

In both of our studies, we are investigating a single type of colloidal suspension over a range of ϕ. We produce a number of samples with different ϕ by producing a dense colloidal glass, and then diluting with solvent by finite increments, producing slides from the reference sample at each dilution. To produce a glass, we strongly centrifuge a nearly density-matched colloid for many hours. We calculate its ϕ by microscopically observing a sub-volume of the sample, using our particle tracking software to count the number of particles:

$$\phi = \frac{V_p}{V_T} = \frac{N_p(\frac{4}{3}\pi\overline{a}^3)}{XYZ}, \tag{4.1}$$

where V_p is the total volume occupied by particles, V_T is the total observed volume, N_p is the total number of counted particles, $\overline{a}$ is the mean particle radius, and x, y, and z are the Cartesian dimensions of the observed volume.

4.3 Sample Chambers

A number of different sample chambers were constructed and used for the work of this dissertation. I will briefly summarize advantages and disadvantages of each, before focusing specifically the ones used for the experiments of Chapters 6 and 7. Regardless of the experiment's requirements, a standard microscope objective is designed to look through a cover-slip of a given thickness. Cover-slip thicknesses are denoted by a rating or number, where "#1.5" is the standard, which has a thickness that ranges from 160 to 190 μm. Standard sample chambers are a scaffold of cover-slips sealed together with low viscosity UV-curable optical epoxy (Norland, Inc.) atop a glass slide, typically ∼1.2 mm thick. While affordable and highly customizable, these sample chambers expose the colloid to a significant amount of epoxy, which can lead to particle aggregation.

Particle aggregation does not occur if the Norland epoxy has been fully cured, which requires 24-48 hours at room temperature. The curing process can be shortened to 12 hours by being baked at 80° *C*. However, sealing the colloid within the slide means that there is a significant probability that the colloid will interface with the epoxy as it is curing, despite great precautions. Also, heating the colloid to 80° *C* can damage the fluorescent dye, as discussed in Sec. 4.1.2.

Rectangular glass capillaries provide a ready-made alternative (VitroCom, Inc.). Capillaries are available in a range of dimensions, with sufficiently thin walls for optical microscopy, and capable of being sealed with little to no contact between colloid and epoxy. Capillaries, while not expensive, do come at a price and cannot be custom tailored.

4.3.1 Wedge-Shaped Cells

For our confinement experiments, in Chapter 6, we must efficiently measure particle dynamics at a given ϕ for a range of volumes. We focus on “thin film-like” confinement between two flat surfaces. We achieve this by constructing a wedge shaped sample chamber, as shown in Fig. 4.2. We build the chamber using a glass slide, a rectangular glass cover-slip, and a narrow piece of a ~60 μm thick Mylar film, employing a method similar to the one used by Refs. [47, 51].

Using UV-curing epoxy (Norland No. 68) we attach the Mylar film near one end of one side of the glass slide so that it runs perpendicular to the slide’s length. Next, the glass cover-slip is laid across the slide so that one end is raised up by the Mylar film. Meanwhile, the cover-slip’s opposite end is clamped down, ensuring the thinnest gap size possible. We seal the sample chamber shut with epoxy, except for two small air holes; the sample is added via one while air escapes via the other. After adding the sample, the two openings are sealed with epoxy. The chamber’s shape is described in Fig. 4.2: a very long chamber with a broad range of thicknesses. Due to the Mylar film, the glass surfaces are not parallel but very slightly angled at 0.4° relative to one another.

Within our field of view, the change in our sample’s thickness due to our sample chamber’s slight taper is less than 0.3 μm, which is negligible for all but the thinnest regions. We do not see any influence of the taper in any of our results, dicussed in Chapter 6, suggesting it is reasonable to consider the two boundaries as locally quasi-parallel. We define y as the direction along which H varies.

A shortcoming of this method is that even the slight pressure of immersion oil against the wide cover-slip, periodically being pushed by the scanning of the microscope objective, is enough to induce drift within the colloid. Generally, ‘drift’ in a sample is the flow of the colloidal suspension; particles in an entire field of view displace by the same amount, in the same direction, over some interval of time. Es-

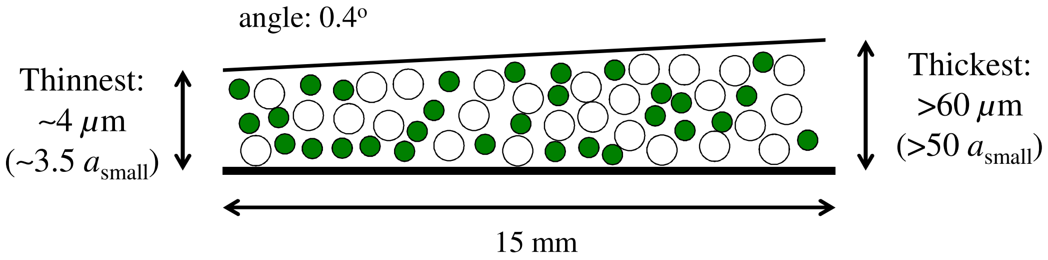

Figure 4.2: Schematic of the wedge-shaped sample volume used to study the effect of confining bidisperse colloidal suspensions. The circles represent the colloidal particles, with the smaller circles colored green for their fluorescent labeling, while the larger ones are white for they are unlabeled and therefore invisible to the confocal microscope. The cell's dimensions are not drawn to scale, the relative diameters of the beads are. The small and large particles are 1.18 μm and 1.55 μm in radius, respectively. The top is a rectangular cover-slip, indicated by the thinner line, and the bottom is a wide glass slide, both made of borosilicate glass (Corning). The two surfaces are "quasi-parallel" in that the inclination is significantly less than a particle radius over the experiment's field of view, approximately 50×50 μm^2.

pecially when slow, drift can be removed from an ensemble of particle displacements, leaving individual particle rearrangements intact, which are more relevant to the structural relaxation processes being studied.

The close proximity of the glass boundaries in the wedge-shaped chamber can induce extraneous structural rearrangements within the colloid. Normally, cover-slips are not inclined and are very narrow, making them far stiffer and unable to buckle when being pressed by immersion oil. The cover-slip's flexibility prohibits the use of three-dimensional image acquisition with high-resolution oil objectives. Instead, we use air objectives and compensated for their relatively low optical resolution by only dyeing the smaller particles in the bidisperse colloid. As a result, the fluorescently labeled tracer particles could be visualized in three dimensions with adequate contrast for accurate tracking.

The colloid is loaded into the chamber using a standard micropipetter to slowly pump the colloid into an inlet along the cover-slip's edge. Loading higher ϕ colloid into the wedge-shaped volume proved to be a challenge due to its very high viscosity. To aid the loading process, at each of the cover-slip's four corners small gaps in the glue were left open to the air. These outlets allowed air to be easily displaced as the colloid gradually filled the chamber. Flowing colloid into narrow channels can result in a phase separation between the particles and solvent phase. Injecting the colloid very slowly into the wedge allowed time for the particles to diffuse throughout the fluid phase, resulting in very uniform density-distributions along the length of the wedge.

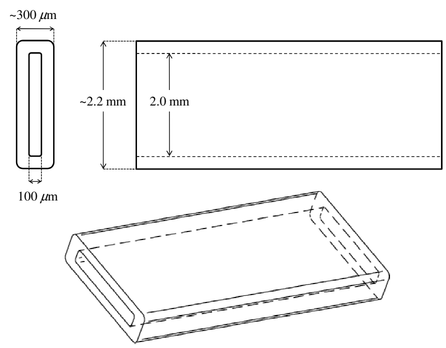

Figure 4.3: A rectangular glass capillary for microscopy of colloidal samples (VitroCom Product #RT5012). The capillary is made of borosilicate glass, with $n \sim 1.5$. The diagram is for illustrative purposes only as it is not to scale. The cross-sectional dimensions are relevant to optical microscopy requirements, but the length of the capillary is arbitrary, ranging from 1 to 2 cm.

4.3.2 Rectangular Capillaries

Our experiments on rotational diffusion required a single type of sample, observed over a broad range of ϕ. Instead, we used many rectangular capillaries, with a cross-sectional area of 0.1×2.0 mm^2, 1-2 cm in length, and $\sim$100 μm thick walls, thinner than the walls of a standard No. 1.5 cover-slip. A diagram of a rectangular capillary is shown in Fig. 4.3. The capillaries were filled by simply dipping one end into the colloid, which would be slowly drawn up into the tube. The colloid would be given a few days to diffuse throughout the volume since the laminar capillary flow can produce cumbersome density gradients, particularly in denser samples.

The ends of the tubes were sealed using UV-curable Norland epoxy, allowing for a pad of air between the colloid and the glue, and glued against a standard sized glass slide for convenient positioning in the microscope stage. When curing the glue under a UV lamp, I was careful to wrap the colloid-filled portions of the tube with aluminum foil. Bright light, from the sun, lamp, or otherwise, can quickly photo-bleach the fluorescent dye. At times, light also seems to affect the electrostatic interactions of the colloidal particles themselves, perhaps through the accelerated breakdown of the CXB solvent.

4.4 Data Acquisition

The "raw data" from our experiments are the original series of confocal micrographs depicting the motion of the colloidal particles in their respective samples. Our data are only as useful as our ability to track the particle displacements, a process that is explained in Chapter 5. The tracking algorithms that we use are designed to identify bright white "blobs" against black backgrounds, meaning that our acquired images must have a high contrast to produce accurate and robust date, with minimal pixel noise or optical distortions, and adequate resolution allowing clear differentiation of particle centers.

4.4.1 Resolution

In microscopy, 'data' is light and so our goal is to gather as much of it as quickly as possible. Therefore, using microscope objectives with the largest possible numerical aperture (NA) is desirable. An objective's NA is a dimensionless number that characterizes the range of angles over which light can be accepted or emitted:

$$\mathrm{NA} = n \sin\theta \tag{4.2}$$

where n is the index of refraction of the medium in which the lens is working. Refer to Fig. 4.4 for a definition of θ.

Increasing the index of refraction of the medium between the objective and the sample increases the objective's effective NA, increasing its optical resolution, the minimal distance that two objects can be optically discerned from one another. We can express this minimal distance in terms of the NA as

$$\delta = \frac{\lambda}{\mathrm{NA}} \tag{4.3}$$

where λ is the wavelength of the light.

To increase n, we use immersion oil whenever possible. An added benefit of using immersion oil is that it produces a uniform medium, from colloid to cover-slip and finally the oil. The uniformity of n between the objective and the sample improves clarity by minimizing the diffraction effect of medium interfaces. A schematic, detailing the improvements in NA from using immersion oil is shown in Fig. 4.4.

The immersion oil, borosilicate glass of the cover-slip, and the colloid all have roughly the same index-of-refraction, with $n \sim 1.5$. An oil immersion lens, with a 63× magnification and an NA of 1.4 was used for our rotational diffusion experiments, discussed in Chapter 7. Due to the flimsy nature of the wedge-shaped samples (See 4.3.1) used for the confinement experiments (see Chapter 6) we were forced to use air objectives to gather three-dimensional data.

Our air objective has a 63× magnification and an NA of 0.7.

Once a good optical resolution is established with the microscope, a corresponding pixel resolution must be set with the confocal. The pixel resolution is defined in terms of the total pixel area of an imaging frame and the real spatial area that it is being used to visualize. The more pixels used to image a particle, the more accurately its

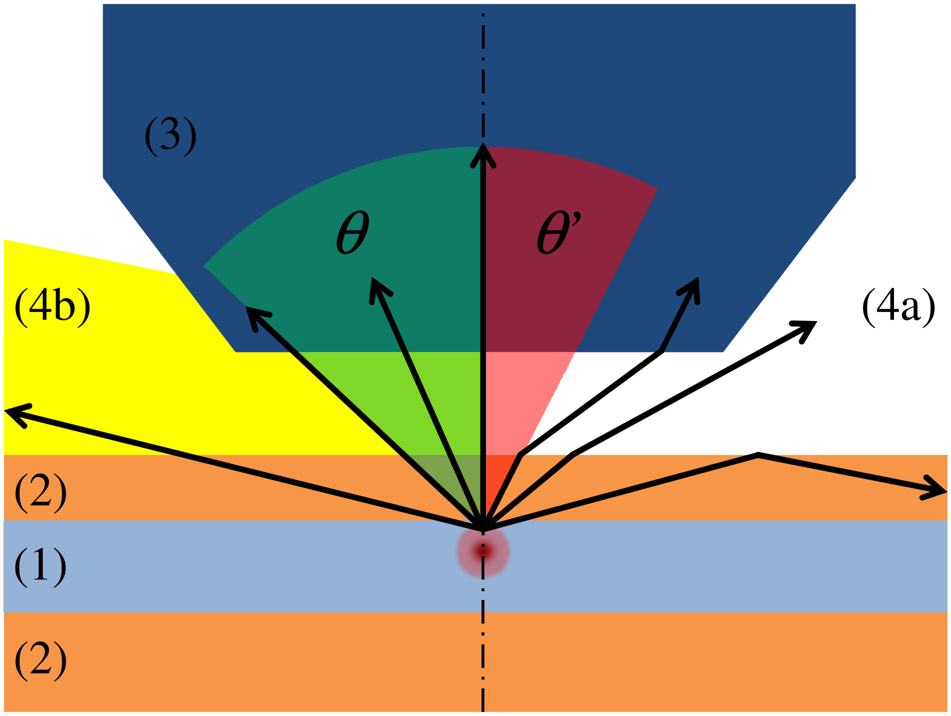

Figure 4.4: Principle of microscopy with immersion fluid. 1) Colloidal suspension. 2) Glass cover-slip or slide. 3) Microscope objective lens. 4) Media between sample and objective; (a) oil or water immersion fluid; (b) air. Path of rays with (left half) and without (right half) immersion medium (yellow). Fluorescent light (black) emitting from the object (red) at a certain angle and going through the cover-slip (orange, same as the slide at the bottom) can enter the objective (dark blue) only when an immersion fluid is used. Otherwise, the refraction at the cover-slip-air interface causes the ray to miss the objective and its information is lost. The angle θ is equated to NA in equation 4.2. The angle θ' denotes the angle over which light is accepted into this same lens if an immersion fluid were not used.

center can be resolved, but the longer it will take for the confocal to raster scan it. Scanning a moving particle too slowly can produce smeared or blurry images, as the particle moves before a single raster scan is completed, negating the benefits of a high pixel resolution [52]. The minimum average pixel-diameter needed for accurate particle tracking can vary, depending on fluorescent emission intensity, general image contrast, and the level of index-matching.

While the number of pixels per frame determine the scan-speed per frame, adjusting the height of the volume to be scanned and the number of frames to scan in the z-direction can dramatically change the rate of acquiring three-dimensional data. In our rotational diffusion experiments, the direction of translational motion of the individual tracer clusters should be isotropic over time. Therefore, in most experiments we would set the acquisition volume to be approximately a 25 μm cube. The step-size between each focal plane is set independently from the width of each pixel, as discussed in Chapter 3. The clustered particles have a diameter of roughly 2.5 μm, so a step-size of 0.2 μm should provide a sufficient number of cross-sections to accurately reconstruct a three-dimensional image of each spherical particle. A larger step-size, meaning fewer scans over the volume's 25 μm height, would translate to a faster acquisition rate but with greater uncertainty in the cluster's z-position.

As discussed in Chapter 3, three-dimensional acquisition rates can be improved by scanning bidirectionally in the z-direction. With bidirectional scanning, cross-sections are acquired in alternating order, meaning that the objective's focal plane does not have to be reset to its starting point after each scan. Instead, odd stacks are scanned in the reverse order of the even stacks. Bidirectional scanning reduces the lag-time Δt, the time between consecutive stacks, but means that the even and odd datasets are unique and must be handled separately. For example, a particle displacing through a scanned volume has its top scanned before its bottom in even stacks, while the reverse is true in odd stacks.

With these various techniques, bidirectional scanning, pixel-resolution and optimizing the dimensions of the acquisition volume, the rate of image acquisition should be such that particles move no more than a single particle radius between consecutive frames. We achieve this through our intuition regarding these colloidal systems, and some trial and error. Specifically, past experience and rough calculations using the Stokes-Einstein-Sutherland models can give us an approximation of how fast a particle will displace its own diameter over some time interval Δt. A final physical constraint on image acquisition rates to be discussed here is fluorescent photo-bleaching. As discussed in Sec. 2.3, fluorescent dye slightly photo-bleaches with each fluorescent emission, and as such there is a finite number of emissions, or raster scans, that colloidal particles can be clearly visualized for. For example, the fluorescently labeled clusters used in our rotational diffusion experiments can be clearly visualized for approximately 500 stacks. A limited number of stacks, coupled against a limitation on viable acquisition rates, limits the experiment's total duration, restricting the number of dynamical events or processes we can observe in our data. Again, as noted in

Chapter 3, data acquisition with confocal microscopy is a balancing act between a significant number of competing parameters.

Chapter 5

Computational Analysis

Micron sized particles suspended in a fluid undergo random motion. This process is known as diffusion and was first observed by Brown in 1827 [53]. In 1905, Einstein derived an analytic solution that accurately predicts the average particle motion [54]. Accurate tracking of the 2D or 3D trajectories of individual colloidal particles allows us to develop an understanding of the microscopic behavior of colloidal materials. By considering an ensemble of these trajectories over a whole sample volume for extended periods of time, we are able to develop relationships between a material's microscopic behavior and macroscopic behavior. It is through particle tracking and statistical analysis that the true strength of colloidal systems is brought to the fore.

5.1 Particle Tracking

We accomplish the computational intensive task of particle tracking using publicly available algorithms first developed by John C. Crocker and David G. Grier, and then modified by Eric R. Weeks [55]. The tracking algorithms, and a majority of all analysis, are done in the IDL programming environment. Typically, for either 2D or 3D data, the particle tracking process follows these 3 basic steps:

1. Spatial band-pass filtration of each image
2. Centroid identification (termed "pretracking")
3. Linking centroids between consecutive frames ("tracking")

The first two steps are depicted by Fig. 5.1, where the raw data is filtered and then the particle centers are identified. Clearly, in Fig. 5.1(b) there are bright white spots without circles, having not been identified as particles. These white spots are smaller since they identify out-of-focus particles in the foreground or background of the rastered focal plane. We can omit these particles through a simple process of thresholding, whether by overall intensity or size.

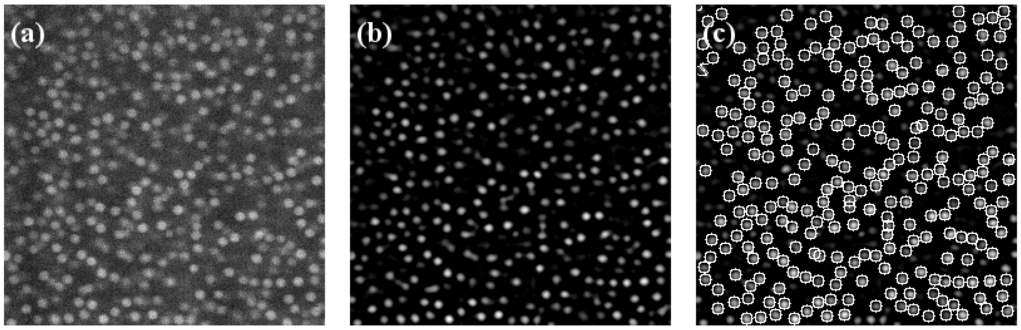

Figure 5.1: Identification of particle centers. (a) Original confocal micrograph of ∼2 μm particles. (b) Filtered by a spatial band-pass, removing the background noise. (c) Particle centers are identified as Gaussian distributions of pixel intensity.

There are a number of parameters that are involved with particle identification. For the band-pass filtration, we define upper and lower spatial extents to smooth over, which correspond to the average pixel-diameter of the particles and the random pixel noise, respectively. The centroid-finding software searches for Gaussian-like distributions of brightness of a given size against a black background. We define the width of the Gaussian fit as an additional parameter, typically the same as the pixel-diameter of the particles. More minor parameters include brightness and minimum separation thresholds, which omit small or excessively dim objects and particles that are overlapping one another due to being in different focal planes.

Before linking the particle centers into trajectories, we must ensure that the positions of the particle centers are not biased by position of the pixels. The particle identification algorithm can identify particles with sub-pixel accuracy, the result of performing a convolution with a Gaussian distribution on the white blobs of light (see Fig. 5.1(b)) rather than simply identifying the blob's peak, or brightest pixel. Therefore, the physical distribution of particle positions should be random, meaning that a histogram of the fractional component of all particle coordinates should be roughly flat. We carefully adjust the above described parameters to overcome pixel-biasing. If pixel-biasing were not accounted for, the particle trajectories would look grid-like, as defined by the pixels.

Having established the accuracy of the coordinates of the particle centers, we may track their paths through the sample. Tracking assigns a unique identification number to each particle for the duration of the series. For tracking to be robust, the particles must not move more than a single radii between successive frames, as discussed in Section 4.4. A particle that moves a significant distance between two consecutive frames could be mistaken for a unique particle, and therefore be assigned a new identification number. We avoid this problem by reducing the lag-time between consecutive images, either 2D or 3D, using the methods detailed in Section 4.4.

The biggest hurdle to overcome in conventional particle tracking is the uncertainty inherent in locating a particle. Typical microscopy experiments combine high magnification optics with CCD cameras to record raw digital images. In the absence of other sources of noise, the uncertainty in particle position, i.e. the minimum noise level, depends on the optical resolution [pixels/distance] of the instrumentation and the size [pixels] of the object being tracked. Standard image processing and particle tracking techniques can locate the centers of particles to within $\approx 1/N$ of a pixel, where N is the width of the object in pixels. Optical resolution varies between experimental set-ups but is typically in the range of 0.2 μm/pixel. The minimum uncertainty in particle position is the product of these factors. For example, observing a 10 pixel wide object with an optical resolution of 0.2 μm/pixel leads to a lower limit of $\approx$ 20 nm uncertainty in particle position. Other sources of noise, such as stray light entering the microscope, noise within the CCD camera itself, and so forth, all contribute to slightly increase the uncertainty in particle position and further limit particle tracking resolution. A thorough discussion of the robustness of tracking rotational diffusion against experimental noise is made in Ref. [23], work that is currently in preparation.

5.2 Tracking Clusters

For the work described in Chapter 7, we track the rotational diffusion of dense clusters of colloidal particles. The dynamics of anisotropic particles has gathered significant interest in recent years, with many studies focusing on ellipsoidal rods, platelets, and an assortment of other unique shapes [40]. However, over the past 15 years, the tracking procedures for spheres described in the prior section have proven to be quite robust. We chose to exploit this strength by using clusters of fluorescently labeled spherical particles to study rotational dynamics in colloidal fluids, rather than developing new algorithms to track totally unique shapes, such as ellipsoids.

The clusters are dense ordered packings of fluorescently labeled core-shell spherical PMMA particles, described in Sec. 2.2.2 and shown in Fig. 5.2. In the same way that we track individual particles, we are able to track these clustered particles as they translationally and rotationally diffuse through a solvent or among other colloidal particles. To calculate a cluster's angular displacement, we define a 3D rotation matrix for a cluster of n particles rotating about their center between times t and $t+1$.

Our procedure for calculating rotational displacements of clusters is based on a method by Challis for determining rigid body transformations between reference frames [56]. In close collaboration with Gary Hunter, I adapted Challis' procedure to measure rotational dynamics. First, we give a brief reprise of Challis' method, and then describe how it is used to study the rotational dynamics of colloidal clusters.

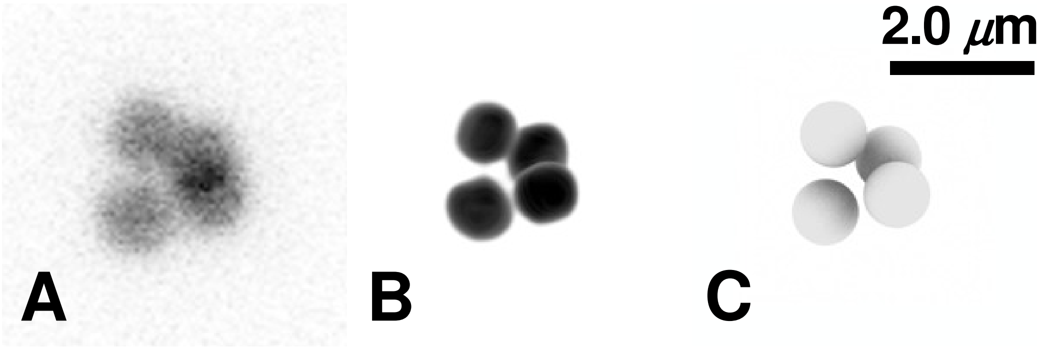

Figure 5.2: Visualizations of a tetrahedral colloidal cluster. (a) Composite of confocal micrographs of tetrahedral cluster of 2.5 μm core-shell particles. (b) Three-dimensional reconstruction of the colloidal cluster. (c) Three-dimensional computer generated rendering of the particle coordinates, defined by particle tracking software [55]. Images A and B have been inverted for clarity.

5.2.1 Challis' Procedure for Coordinate Transformations

Given a set of points which have coordinates $\{\mathbf{x}_i\}$ measured in one reference frame and coordinates $\{\mathbf{y}_i\}$ measured in a second frame, there exists a transformation

$$\mathbf{y}_i = s\mathbf{R}\mathbf{x}_i + \mathbf{v}, \tag{5.1}$$

where subscript i refers to the i-th point in the set, s is a scale factor, $\mathbf{R}$ is a rotation matrix, and $\mathbf{v}$ is the vector separation of the two reference frames. For our purposes, we may set the scale factor to unity and assume that both coordinate frames share a common origin, thereby setting all elements of $\mathbf{v}$ to zero.

We are therefore left with

$$\mathbf{y}_i = \mathbf{R}\mathbf{x}_i, \tag{5.2}$$

and only the rotation matrix to describe the transformation between coordinate frames. The rotation matrix is an orthonormal matrix with the properties

$$\mathbf{R}\mathbf{R}^{-1} = \mathbf{R}\mathbf{R}^{\mathrm{T}} = \mathbf{R}^{\mathrm{T}}\mathbf{R} = \mathbf{E}, \tag{5.3}$$

$$\det(\mathbf{R}) = +1, \tag{5.4}$$

where $\mathbf{E}$ is the identity matrix and $\det()$ denotes the determinant.

For a set of n points, $\mathbf{R}$ can be calculated using a least squares approach. This method minimizes the quantity

$$\frac{1}{n}\sum_{i=1}^{n}\left[\mathbf{y}_i - \mathbf{R}\mathbf{x}_i\right]^{\mathrm{T}}\left[\mathbf{y}_i - \mathbf{R}\mathbf{x}_i\right]. \tag{5.5}$$

Expanding Eq. (5.5) yields

$$\frac{1}{n}\sum_{i=1}^{n}(\mathbf{y}_i)^{\mathrm{T}}\mathbf{y}_i + (\mathbf{x}_i)^{\mathrm{T}}\mathbf{x}_i - 2(\mathbf{y}_i)^{\mathrm{T}}\mathbf{R}\mathbf{x}_i, \tag{5.6}$$

therefore, minimizing Eq. (5.6) is equivalent to maximizing

$$\frac{1}{n}\sum_{i=1}^{n}(\mathbf{y}_i)^{\mathrm{T}}\mathbf{R}\mathbf{x}_i = \mathrm{Tr}\left(\mathbf{R}^{\mathrm{T}}\frac{1}{n}\sum_{i=1}^{n}\mathbf{y}_i(\mathbf{x}_i)^{\mathrm{T}}\right) = \mathrm{Tr}(\mathbf{R}^{\mathrm{T}}\mathbf{C}), \tag{5.7}$$

where $\mathbf{C}$ is the cross-dispersion matrix calculated from

$$\mathbf{C} = \frac{1}{n}\sum_{i=1}^{n}\mathbf{y}_i(\mathbf{x}_i)^{\mathrm{T}}. \tag{5.8}$$

At this point, a singular value decomposition is performed on $\mathbf{C}$ such that

$$\mathbf{C} = \mathbf{U}\mathbf{W}\mathbf{V}^{\mathrm{T}}, \tag{5.9}$$

where $\mathbf{W}$ is a diagonal matrix containing the singular values of $\mathbf{C}$, and $\mathbf{U}$ and $\mathbf{V}$ are orthogonal matrices. As was shown in [56], upon maximizing Eq. (5.7), $\mathbf{R}$ is given by

$$\mathbf{R} = \mathbf{U}\begin{bmatrix} 1 & 0 & 0 \\ 0 & 1 & 0 \\ 0 & 0 & \det(\mathbf{U}\mathbf{V}^{\mathrm{T}}) \end{bmatrix}\mathbf{V}^{\mathrm{T}}. \tag{5.10}$$

This procedure is applicable to all non-colinear sets of points with $n \geq 3$.

5.2.2 Application to Colloidal Clusters

Particle tracking [25, 55] yields vector coordinates $\mathbf{x}'_i$ for every particle i over a distinct set of times. Hence, the first step in tracking rotational motion of a cluster is to track the translational motion of each particle within the cluster. For each cluster, we first determine the center of mass $\mathbf{x}_{CM}$ at a given time and subtract this quantity from the coordinates of particles belonging to the cluster, thereby removing any translational motion. We are left with new coordinates $\mathbf{x}_i$ in the center of mass frame,

$$\mathbf{x}_i = \mathbf{x}'_i - \mathbf{x}_{CM}. \tag{5.11}$$

This step is equivalent to setting the elements of $\mathbf{v}$ to zero in Eq. (5.1). With translational motion removed, we may apply Eq. (5.2) with a slightly different interpretation. Rather than representing a transformation between coordinate frames, we may understand $\mathbf{R}$ as describing the rotational trajectory of a particle with inital position $\mathbf{x}^0_i$ to a final position $\mathbf{x}_i$ such that

$$\mathbf{x}_i = \mathbf{R}\mathbf{x}^0_i. \tag{5.12}$$

Therefore, we may use Challis' procedure to calculate a rotation matrix for each pair of successive times $[t, t+\Delta t]$. With the complete set of rotation matrices, $\{\mathbf{R}^k\}$, we may reconstruct the entire trajectory of a particle about the cluster center of mass by computing the product of successive rotations. Given $\mathbf{x}_i^0$, the position of a particle at some later time t can be calculated as

$$\mathbf{x}_i(t) = \mathbf{R}^{t-\Delta t}\mathbf{R}^{t-2\Delta t} ... \ \mathbf{R}^0 \mathbf{x}_i^0 = \prod_k \mathbf{R}^k \mathbf{x}_i^0, \tag{5.13}$$

where the index k enumerates the rotation between successive times.

The advantage of calculating $\{\mathbf{R^k}\}$ is that it describes the collective behaviors of particles within a cluster, rather than a property of any individual particle. For example, knowledge of $\{\mathbf{R^k}\}$ for a cluster allows for immediate calculation of the motions of any particular particle about the center of mass, or the motion of the cluster about any arbitrary axis of rotation. Diffusive anisotropic clusters with large aspect ratios rotate more freely about a long axis than about a short axis. Given $\{\mathbf{R^k}\}$, however, one needs only the initial orientation of these axes to compute and compare the motions around them.

5.3 Analysis of Motion

We use an assortment of basic methods to analyze particle trajectories. Our analysis provides information describing both the microscopic and macroscopic properties of a colloidal fluid, and by extension provides comparison to real materials. The methods described in this section apply to the analysis of both translational and rotational dynamics as their functional forms are analogous. Analysis specific to our work on the confinement effect or rotational diffusion will be discussed in Chapters 6 and 7, respectively.

5.3.1 Mean Square Displacement

Consider the average displacement of a diffusing tracer particle after an n-step, one-dimensional random walk. The tracer's random walk accurately models the Brownian motion of a particle in a true liquid. Being a true stochastic process, the probability distribution for the random walk is symmetric about the origin, resulting in a mean displacement of zero. An average displacement of zero is the result of motion in either direction being equally likely, and thus effectively cancel one another out. It is not because the tracer scarcely moves from its initial position, which shows that the mean displacement is not a useful parameter to characterize a diffusing particle's trajectory. Instead of directly taking the mean of the displacement, we first square the displacement to eliminate any differences in sign, and then average.

If a diffusing particle's position is given as $\vec{r}(t)$ in time, and the displacement is defined as $\Delta\vec{r}(t, \Delta t) \equiv \vec{r}(t+\Delta t) - \vec{r}(t)$. In practice, when dealing with a number of particle trajectories in the same system, we take an ensemble average over a number of particle trajectories and a number of lag-times:

$$\langle \Delta r^2 \rangle = \langle [r_i(t + \Delta t) - r_i(t)]^2 \rangle_{i,t} \tag{5.14}$$

where the average is taken over all particles i and all initial times t. The mean square displacement (MSD) grows as:

$$\langle \Delta r^2 \rangle_t = 6 D_T \Delta t, \tag{5.15}$$

with the diffusion constant D_T given by

$$D_T = \frac{k_B T}{6\pi\eta a} \tag{5.16}$$

where k_B is Boltzmann's constant, T is temperature, η is the viscosity of the fluid, and a is the hydrodynamic radius of the particles. Equation 5.16 is known as the Stokes-Einstein relation, or more recently as the Stokes-Einstein-Sutherland relation [57], given that both Einstein and Sutherland independently published this result in 1905. Consider Fig. 5.4, which shows a plot of MSD curves for a colloid at two different ϕ. The MSD is perhaps the single richest source of information regarding supercooled colloidal systems.

Particles also undergo rotational diffusion. While there are other ways to evaluate rotational motion [58], we use the MSAD as it is the most intuitively comparable to the MSD [59]. The MSAD is analogous to the MSD, providing the same type of information but relevant for the rotational diffusion of both spherical and non-spherical particles. Consider a vector $\hat{p}(t)$ rigidly attached to a particle; the particle may be of any shape. Between t and $t + \Delta t$, the particle rotates and the orientation changes from $\hat{p}(t)$ to $\hat{p}(t+\Delta t)$. Thus a rotation vector $\delta\vec{\varphi}(t)$ can be defined, such that its amplitude relates to the angle swept out by $\hat{p}$, $\cos|\delta\vec{\varphi}(t)| = \hat{p}(t)\cdot\hat{p}(t+\Delta t)$, and the direction is given by $\hat{p}(t)\times\hat{p}(t+\Delta t)$ [60, 61]. In other words, in the given time interval, the particle has rotated slightly about the axis defined by $\delta\vec{\varphi}(t)$. Following work by Ref. [59], we evaluate the MSAD in terms of an unbounded angular displacement:

$$\vec{\varphi}(\Delta t) = \int_t^{t+\Delta t} \Delta\vec{\varphi}(t')dt' \tag{5.17}$$

in the time interval $[t, t + \Delta t]$. The direction of vector $\Delta\vec{\varphi}(t')$ during this interval is aligned with a particle's axis of rotation, with its components in Cartesian coordinates. In this way we may define an unbounded MSAD

$$\langle \Delta\vec{\varphi}^2(\Delta t) \rangle = \langle [\vec{\varphi}(t + \Delta t) - \vec{\varphi}(t)]^2 \rangle, \tag{5.18}$$

where the average is over all initial times t, analogous to the MSD above, therefore allowing direct comparison between the two.

The MSAD grows as $\langle \varphi^2 \rangle = 4D_R\Delta t$, with the rotational diffusion coefficient for spheres given as

$$D_R = \frac{k_B T}{8\pi\eta a^3}. \tag{5.19}$$

This is known as the Stokes-Einstein-Debye relation and was originally found by Debye [62].

Both D_T and D_R, for translational and rotational motion respectively, depend on temperature T and viscosity η in the same way. Thus, for liquids the relationship between the two diffusion coefficients is constant:

$$\frac{D_T}{D_R} = constant \ \ (= \frac{4}{3}a^2 \ \text{ for spheres}). \tag{5.20}$$

One caveat in considering the rotational trajectory about only a single axis of rotation for a given cluster is that significant dynamical processes may be overlooked. Specifically, rotations around an axis normal to the axis being considered would be completely overlooked. Therefore when considering tetrahedral clusters, we use four orientation vectors, each extending from the cluster's center to the center of each of the clustered particles. We evaluate the MSADs for each vector and then calculate their mean, i.e. the MSAD would include an ensemble average of the 4 axes of rotation. Plots of MSAD and further discussion are included in Chapter 7.

Plots of the MSD and MSAD provide information regarding a colloidal system's time scales and length scales, which can be related to the sample's structural properties. For example, in log-log space, an MSD with a slope of 1.0 suggests diffusivity over a given time scale. A near hard-sphere colloidal suspension with amorphous structure, for $\phi < 0.58$, will exhibit diffusivity over sufficiently long time scales. For example, the orange MSD curve in Fig. 5.4 is for a colloid in the dilute limit with low ϕ, and has a slope of ∼1.0 for its full duration. The MSD curve's linearity reflects the colloid's dilute nature, where regardless of the observation time or distance traveled a particle's mobility is not impeded. Meanwhile, the MSD for higher ϕ (blue) has a slope of ∼1.0 for $\Delta t < 10$ s and $\Delta t > 100$ s. However, over the range 10 s $< \Delta t <$ 100 s, the curve plateaus. In our experiments, where the particles are nearly hard-spheres, a plateau in the MSD is interpreted as the presence of cage-trapping dynamics within the colloid, meaning that particles are crowded in by their local neighboring particles.

5.3.2 Quantifying Noise

There are instances where the plateau of the MSD is actually due to noise, and not a cage-trapping event. To understand to origin of how image noise can result in a non-zero vertical offset of the MSD's plateau, consider imaging and tracking a stationary particle. The true trajectory of this immobilized particle is a solitary dot in space, with no change in position in the lab's frame of reference over time; the MSD of this particle would have a magnitude of 0. However, slight variations of pixel intensity, random noise in the CCD detector, and minor shifts in the microscope system's various mechanical components, either from thermal fluctuations or various sources of vibrations, all manifest into random variations in the particle's image which we term "noise". The noise or uncertainty in particle position over a series of image frames will make stationary particles appear to move. As a result, the MSD of an immobilized particle will have a plateau of some finite magnitude. In data of particles whose true displacements are smaller than those produced by noise, it is useful to explicitly quantify the offset of this plateau to determine what portion of our MSD are due to real dynamics.

To quantify the level of uncertainty in an MSD or MSAD we use a technique developed by Gary L. Hunter, and described in Ref. [23]. We begin by quantifying the width of the noise δ_x by calculating the standard deviation of a Gaussian fit to a distribution of the immobilized particle positions. The standard deviation of displacements in the x-direction results in an uncertainty of

$$\langle \Delta x^2 \rangle = 2\delta_x^2. \tag{5.21}$$

Therefore, in three-dimensions, the uncertainty in particle position is

$$\Delta r^2 = 2(\delta_x^2 + \delta_y^2 + \delta_z^2). \tag{5.22}$$

As noted above, an MSD of this noise would appear as a plateau, whose offset is raised and lowered with variation of the average noise level. More typically, however, an MSD's noise is quantified by the vertical offset of a plateau that exists at the smallest lag-times Δt; a plateau at low Δt can be a hallmark sign of noise. The MSD data of a mobile particle at sufficiently large Δt will rise above the uncertainty as the particle's displacements out-pace the pixel variations caused by noise.

In our confinement experiments, discussed in Chapter 6, the good image clarity and appreciable particle dynamics resulted in a high signal to noise ratio; the true particle displacements are greater than those produced by random noise in the image. However, in our experiments studying the rotational diffusion of colloidal clusters discussed in Chapter 7, the noise levels could at times overwhelm the actual particle dynamics. Rotational displacements slowed to such an extent that explicit calculation of the uncertainty in our results proved necessary in order to discern which portions of the MSAD curves represented true particle dynamics.

To calculate the uncertainty of a rotating cluster of particles, such as the tetrahedral cluster in Fig. 5.2, we begin by pinning the cluster's center to the origin of our coordinate system. The average angular displacement of the cluster, defined as its MSAD, is effectively described in terms of the clustered particles diffusing across the surface of a sphere whose center is pinned to the cluster's center. For example, consider Fig. 5.3. The uncertainty of a surface-bound particle's position in space, given by Eqn. 5.22, results in an angular displacement δ_θ across the sphere's surface between image frames due purely to image noise.

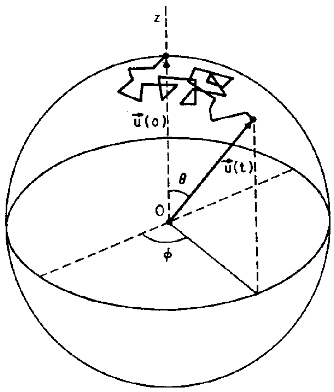

Figure 5.3: Particle diffusing on surface of unit sphere. Rotational diffusion can be represented by a point randomly diffusing on the surface of a unit sphere. Picture from Ref. [63].

We can express an arc length δ_l in terms of this angular displacement:

$$\delta_l = R \times \delta_\theta, \tag{5.23}$$

where R is the distance between the center of the cluster and one of the clustered particles. Using the expression for δ_l we define the uncertainty in angular displacement as, and square it to obtain a positive magnitude:

$$\delta_\theta = \frac{\delta_l}{R} \tag{5.24}$$

$$\delta_\theta^2 = \frac{\delta_l^2}{R^2} \tag{5.25}$$

We now replace δ_l with the uncertainty in particle position, given by Eqn. 5.22, to calculate the uncertainty in angular displacement:

$$\langle \Delta\theta^2 \rangle = \frac{2(\delta_x^2 + \delta_y^2 + \delta_z^2)}{R^2} \tag{5.26}$$

Since our MSAD is for a cluster of n particles, the uncertainty must include a factor of $1/n$:

$$\langle \Delta\theta^2 \rangle = \frac{2(\delta_x^2 + \delta_y^2 + \delta_z^2)}{nR^2} \tag{5.27}$$

A plateau in the curve of an MSAD plot, whose vertical offset is greater than the magnitude of Eqn. 5.27, most likely reflects true cage-trapping dynamics. In a recent

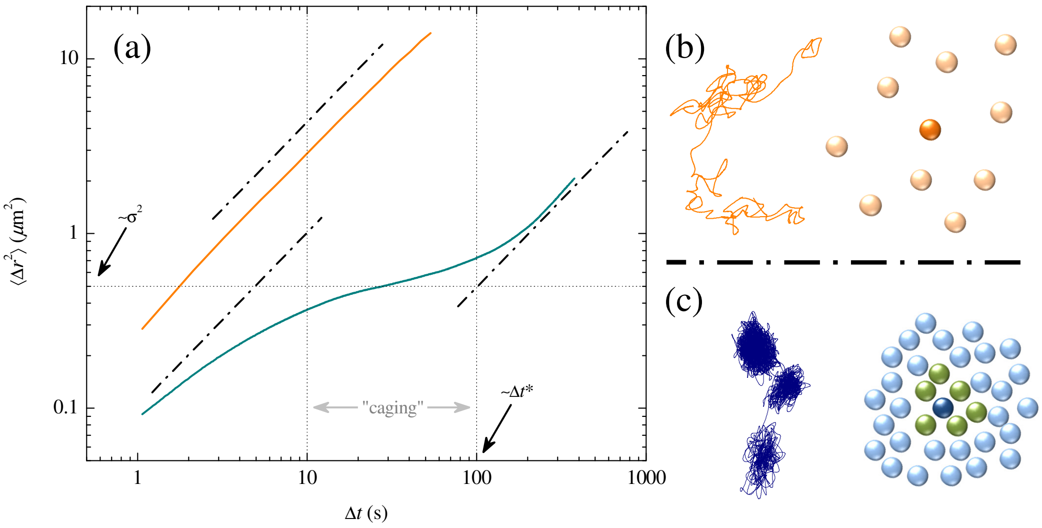

Figure 5.4: Description of relationship between MSD plots and particle trajectories. (a) Plot of the MSD for $\phi \sim 0.20$ (orange) and $\phi \sim 0.50$ (blue). The black dashed lines both have a slope of 1.0, proportional to purely diffusive Brownian motion. (b) Example of trajectory described by orange MSD in (a). On the right, in (b), is a cartoon describing positions of particles in sample described by orange MSD in (a), where particles are in the dilute limit. (c) Example of trajectory being described by blue MSD in (a). On right in (c), a cartoon describing particle positions in sample described by blue MSD in (a); the dark blue particle's trajectory exhibits tightly localized motion in three separate locations, due to "cages" formed by its nearest neighbors (green). The eventual random rearrangements of cages allow hops, of which two are shown in the blue trajectory.

body of work by my colleague Gary Hunter [23], we have determined that when taking uncertainty due to image noise into account, our tracking techniques can resolve angular displacements as small as 1.6°.

Cage-trapping dynamics are a microscopic component of colloidal systems, and a detailed discussion of how we identify cage-breaking events will be continued in the next section, Sec. 5.3.3. Macroscopic properties, such as the colloid's diffusion coefficient D_{T} and viscosity η, can be determined by fitting a line with a slope of 1.0, in log-log space, to the MSD's diffusive region. The line's offset in log-log space translates to a slope in linear space, which can be used to calculate the colloid's diffusion coefficient, using the following expression:

$$D_{\mathrm{T}} = \frac{\langle r^2 \rangle}{3d\Delta t} \tag{5.28}$$

where d is the dimension of motion and Δt in this context is the span of the MSD's diffusive region. Equation 5.28 is simply a reformulation of Eqn. 5.15.

5.3.3 Identification of Cage-Breaking Events

A major point of interest in our investigations of both the confinement effect and rotational diffusion has been related to cage-trapping dynamics. The nature or appearance of trajectories, in the context of the sample they came from, can provide critical details of what kind of features to expect in subsequent quantitative analyses. Plots of MSD curves, as discussed in the prior section, can provide critical clues about the dynamics of a colloidal suspension, but an MSD is an ensemble average. For a more fine-grained analysis of our tracked data sets we make a visual inspection of the individual particle trajectories.

The process of cage rearrangements leads to a liquid's overall structural relaxation [4, 64]. The chemists Gerold Adam and Julian Gibbs first hypothesized the existence of "cooperatively rearranging regions" (CRRs) of molecules as a supercooled liquid's means of increasing its configurational entropy [15]. Their model very precisely matches the popular empirical WLF relation [65], with excellent agreement to data from a large number of molecular and polymeric glass-formers. As the glass transition is approached, the divergence in a liquid's viscosity is matched by the divergence in the mean length-scale and time-scale of its CRRs [14, 17]. The divergence in length-scale could be thought of as a point when all of a material's molecules must move for any one molecule to move, which is by definition a solid.

Conceptually, prior simulations [14] and experiments [17, 66] have defined these cooperative regions simply as groups of neighboring molecules or particles that collectively rearrange their positions in order to realize a new position in space. The precise definition of a cooperatively rearranging region is open to interpretation. In our work on the confinement effect, discussed in Chapter 6, our definition of a CRR is comprised of three key elements: (1) the time scale used to determine displacements,

(2) the threshold for considering a displacement to be a "rearrangement," and (3) the definition of which particles are adjacent, such that their motion is "cooperative."

As of June 2011, in our experimental investigations of decoupling between translational and rotational diffusion, see Chapter 7, we are still investigating the role of cage-trapping dynamics. Strictly speaking, evaluation of cooperativity among particles is inaccessible due to our inability to see the particles surrounding the individual tracers. Instead we focus on evaluating the occurrence of cage-breaking events, and have employed two different methods for doing so. The first relatively simple method employs two of the elements used in our analysis of the confinement experiments: (1) determine a time scale over which cage-breaking displacements occur and (2) determine the threshold that qualifies a displacement as a "rearrangement". The second more involved method, known as the Iterative Barycenter Separation algorithm (IBS), was recently reported by R. Candelier, *et al.* in the supplementary portion of Ref. [67]. A discussion of the IBS is presented in Sec. 5.3.3.

Mobility Threshold

In our upcoming investigation of the effect of confinement of CRRs [21], we use a mobility threshold to define cooperative rearrangements. As mentioned above, we begin by identifying the time scale of interest. The Δt at which the MSD curve first becomes sub-diffusive, the onset of the plateau, provides an approximation of the time it takes for a particle to explore its cage. Think of this as the time it takes for a particle to diffuse within its cage before being restricted by its nearest neighbors. The width of the plateau indicates the average duration of a cage-trapping event; the plateau in Fig. 5.4 has a duration of approximately 90 s. The timing of the upturn at the end of the plateau is known as the rearrangement time scale Δt^*, which is ~100 s for the sample in Fig. 5.4. Finally, the plateau's vertical offset corresponds to the average cage size σ_c [67], where

$$\sigma(\Delta t) = \sqrt{\langle (r(t+\Delta t) - r(t))^2 \rangle}. \tag{5.29}$$

To pinpoint the value of Δt^* we refer to the probability distribution of displacements, as done in prior work in the field. Rearranging particles have displacements that are larger than normal, and thus lie in the tails of the distribution. While these displacements are rare statistical outliers, they are nonetheless responsible for the upturn in the MSD at large lag-times [14, 17, 66, 68, 69]. The importance of the outliers is quantified by calculating the non-Gaussian parameter α_2 where,

$$\alpha_2(\Delta t) = \frac{d\langle \Delta r^4 \rangle}{(d+2)\langle \Delta r^2 \rangle^2} - 1, \tag{5.30}$$

from Ref. [70], where again d is the dimension (See 5.28). The maximum of α_2 defines the cage rearrangement time scale Δt^*. We use α_2 to define this timescale in our confinement work, discussed in Chapter 6. Figure 1 of Ref. [17] provides the classic example of how this technique is used in colloidal experiments.

To define the length scale which separates a "rearranging" displacement from a "caged" displacement, we use a mobility threshold Δr^*. We can define Δr^* as the average displacement in Δt^*, which coincides with some threshold that defines the most mobile particles in the sample. Both experiments [17, 71] and simulations [72] have used a displacement threshold to define mobility such that over time, some percentage of the particles have displacements $|\Delta\vec{r}| \geq \Delta r^*$ [14, 72], although at any given time the exact fraction may not be exactly this percentage. Thresholds of the top 5th percentile [17, 72, 73], 8th percentile [74], 10th percentile [71], and 20th percentile [45] have all been used to define Δr^*.

In our confinement experiments, we define our mobility threshold as the top 10% of the most mobile particles, which is the percentage of displacements in the x-y direction that deviate from Gaussian behavior. For each of the confinement thicknesses H that we considered, roughly 10% of the most mobile particles deviate from a Gaussian distribution. We do not include displacements in the z-direction in this calculation, however. Being normal to the confining boundaries, displacements in the z-direction can vary significantly with H, making their inclusion in the calculation of our mobility threshold impractical.

To complete our identification of CRRs we must identify which highly mobile particles are simultaneously nearest neighbors. Two methods of determining nearest neighbors are (1) the use of 3D Delaunay tessellations of particle positions [17, 75] and (2) the definition of a minimum separation as a cutoff distance set by the first minimum of the pair correlation function $g(r)$ [73, 74]. In the analysis of our confinement experiments, we use the pair correlation function, which effectively produces a probability distribution of nearest neighbor distances. Consider the example in Fig. 5.5, created from the same 2D data used in Fig. 5.6. The position of the first and largest peak is the most probable distance at which neighboring particles are located.

The pair correlation function is computed using an iterative procedure. We begin by choosing some distance interval Δr. Next, we loop over a range of values of r that we define. For example, the data plotted in Fig. 5.5 is calculated for $1\ \mu\text{m} \leq r \leq 9\ \mu\text{m}$ with an interval of $\Delta r = 0.01\ \mu\text{m} = 10$ nm. We consider all the particles that exist within each iteration, counting particles that are a distance between $r \leq r + \Delta r$ away from the particle being considered. In other words, we are considering all particles in a spherical shell surrounding the reference particle, where the shell has a thickness of Δr. We divide our total count by N, the number of reference particles considered, which could be the total number of particles in our data–this depends on the range set by r. We then divide this number of $4\pi r^2 \Delta r$, the spherical shell's volume, i.e. the shell's surface area multiplied by its thickness: $4\pi r^2 \times \Delta r$. In this way, we account for the increasing number of particles as r increases. Finally, we divide by the particle number density, which ensures that $g(r) = 1$ for data with no structure. In other words, an arbitrarily placed spherical shell of inner radius r and

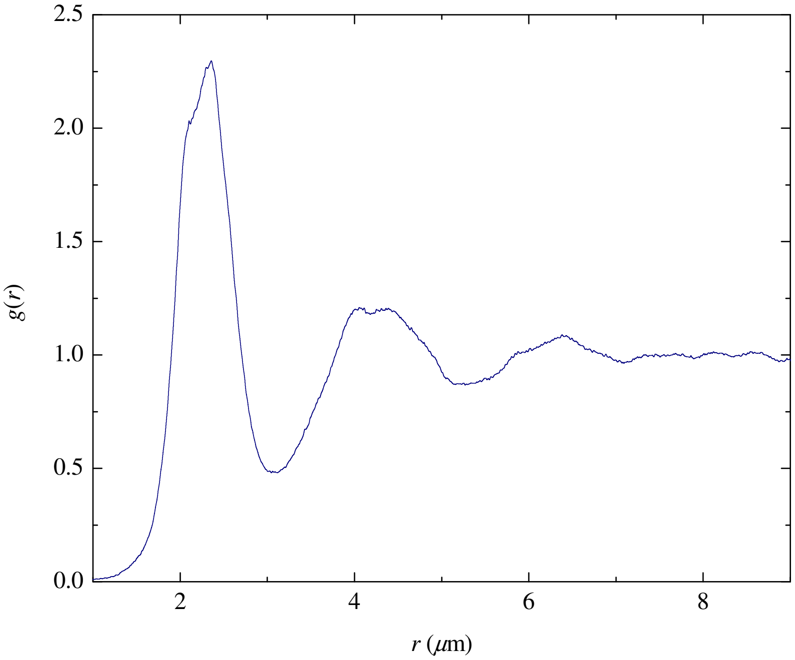

Figure 5.5: Distribution from pair correlation function for cross-section of bidisperse confined colloidal suspension. Particles have hydrodynamic radii of $a_{\text{small}} = 1.18$ μm and $a_{\text{large}} = 1.55$ μm. Here, the function counts a two-dimensional cross-section of only the small particles.

outer radius $r + \Delta r$ would have about $\rho \times V$ particles inside, where ρ is the number density and V is the volume of that shell.

In our work with rotational tracers, see Chapter 7, only the tracer is visible. As a result, we may only observe major rearrangements made by the tracer itself, and are unable to evaluate regions of cooperativity. Similar to our confinement experiments, we determine the time scale of significant rearrangements in terms of the time scale of diffusivity, indicated by the upturn in the cluster's MSD and MSAD curves. We lack the statistics necessary to evaluate the non-Gaussian parameter (eqn. 5.30), so instead we use the Δt at which the upturn occurs to define our time scale of cage-rearrangements. Plots of displacements over this Δt depict prominent spikes that coincide with the largest steps of the cluster's trajectory. Figures of such plots are provided in Chapter 7.

Iterative Barycenters Separation

Presently, the Iterative Barycenters Separation (IBS) algorithm is the most robust method available for determining the precise coordinate of a cage-breaking event. The IBS algorithm determines the point on a trajectory that is the furthest from its two halves, where each ‘half’ is an effective barycenter of the trajectory. Figure 5.6 shows a pair of plots that demonstrate use of the IBS algorithm on a 2D trajectory from my confinement data, published here [19] and discussed in Chapter 6. However, the IBS algorithm may not be appropriate for use on our trajectories of rotating clusters. The IBS algorithm was initially designed for 2D trajectories from computer simulations with a significant number of statistics [76, 77], while the trajectories of our rotating clusters are three-dimensional and shorter in duration. While analysis produced from the IBS is not included the results section of this dissertation, Chapters 6 and 7, I was able to implement it and use it on my data and it provided useful insight, so it is worth discussing.

Most generally, the IBS calculates the distance between two subsets of a trajectory using the following expression:

$$\forall t \in [t_i, t_f], \qquad \widetilde{p}(t) = \sqrt{\langle d_1(t_2)^2\rangle_{t_2\in S_2} \cdot \langle d_2(t_1)^2\rangle_{t_1\in S_1}} \tag{5.31}$$

where t_i and t_f are the initial and final times of the trajectory, $S_1 = t_i : t$ and $S_2 = t : t_f$ are the two subsets of points before and after time t, $d_i(t_j)$ stands for the Euclidean distance from the position at t_j to the center of mass of the subset S_i, and $\langle\cdot\rangle_{t_j\in S_j}$ denotes an average over the subset S_j. $\widetilde{p}(t)$ is therefore the product of the root mean square distances between all the points of the subsets to the barycenter of the *other* subset. In order for $\widetilde{p}(t)$ to be well defined, each subset must contain enough points to accurately approximate the barycenter's position, which is of course not too close to the bounds t_i and t_f. To compensate for the decrease in statistics near the bounds, it is useful to normalize the distribution in terms of t. In Candelier's work, they call this normalized quantity $p(t) = \xi(t) \cdot \widetilde{p}(t)$, where

$$\xi(t) = \frac{2[(t_f - t)(t - t_i)]^{1/2}}{t_f - t_i} \tag{5.32}$$

is a natural normalization of $\widetilde{p}(t)$, counterweighting the lack of statistics in subsets defined near a trajectory's extremities. We interpret the $p(t)$ almost as a plot of distance between two barycenters. First, consider when a subset's motion takes place entirely within a cage; the subset's two barycenters remain close to one another, producing a roughly constant $\widetilde{p}(t)$. An example of a flat fully caged $p(t)$ is shown in Fig. 5.6(b), in blue. Next, consider the case of a cage jump: $p(t)$ peaks at t when both barycenters are separated by the greatest distance, the midpoint of a cage jump. A good example of a peaking $p(t)$, identifying a cage jump, is shown in Fig. 5.6(b), plotted in gray.

As the name suggests, the IBS algorithm is run iteratively, until all cage jumps are identified. Iterations are completed until reaching a length-scale threshold, defined as the point at which the system becomes diffusive. Specifically, the length-scale roughly corresponds to σ_c^2, the square of the average cage size, which is the vertical offset of the MSD's plateau. Naturally, for a cage-break to be identified, the center to center

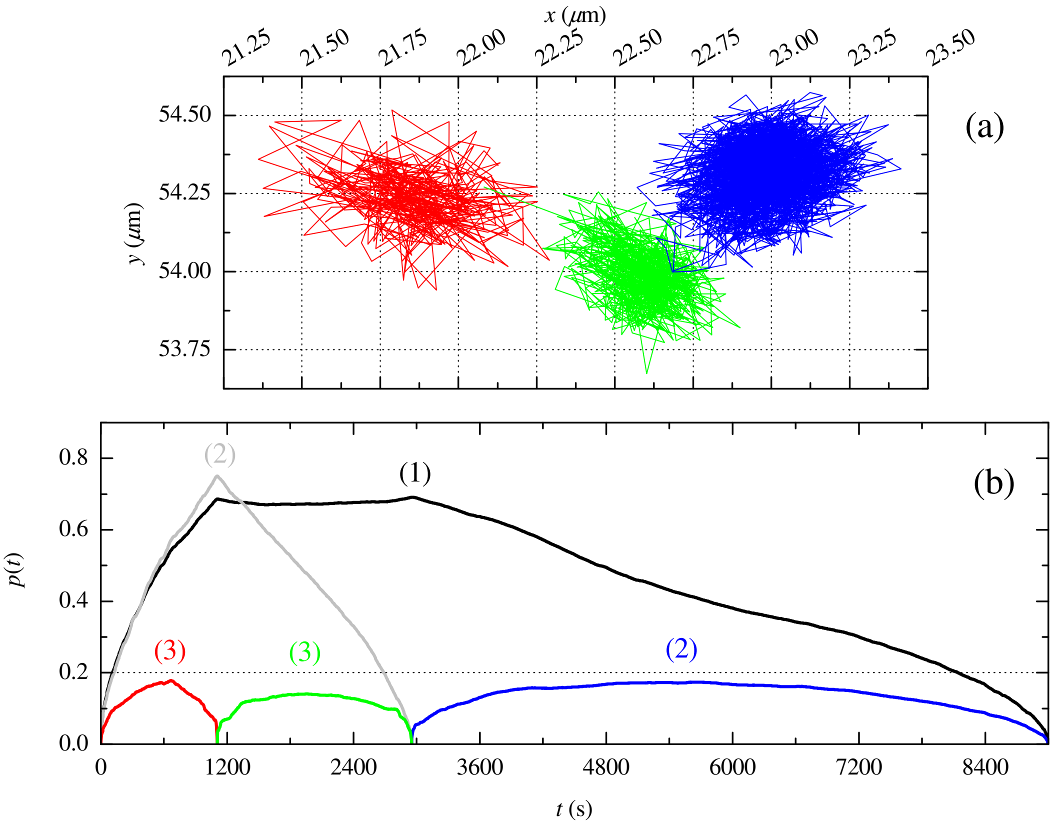

Figure 5.6: The IBS algorithm finds cage-breaking events in two-dimensional trajectories. (a) A two-dimensional particle trajectory from a confined colloid [19]. The colors correspond to respective IBS distributions, in (b). (b) The normalized IBS distributions for the trajectory in (a). The IBS is run iteratively, where each iteration measures the distance between two subsets (See 5.31). The peaks occur at a time of maximal distance from either subset's half or barycenter. Sharp peaks indicate a cage-breaking event. Peaks from one iteration define the subsets of the next. Iterations continue until barycenters are smaller than the mean cage size, equivalent to the length-scale over which the colloid enters the diffusive regime (See 5.3.1), indicated here by the horizontal dotted line. Each subset is enumerated in the figure: iteration (2) produced the gray and blue distributions, where the blue distribution falls below the threshold, halting subsequent iterations. The blue distribution is flat, indicating that no coordinate is significantly far from either barycenter; see how for the blue portion of the trajectory in (a) the particle remains caged for roughly two thirds of the data's duration.

distance between cages must be larger than the cage size itself. Again, this feature of the MSD and expression for σ are discussed above and indicated in Fig. 5.4.

5.3.4 Significance of Cage-Breaking

As discussed in the prior sections, cooperative rearrangements in molecular glass formers, and likewise colloidal systems, are a dynamical event that play a key role in how supercooled liquids accomplish structural relaxations until the onset of the glass transition [10, 15]. The divergence in the size of these groups is mirrored by the divergence in the material's effective viscosity [17]. Even beyond the glass transition, CRRs persist and continue to facilitate a glass's equilibration as it ages [45].

Over the past few years, we have probed the length-scales of CRRs in colloidal model systems by confining them to sample volumes comparable in size to the fluid's dynamic length-scale [20, 21, 30]. We have also begun novel investigations into the relationship between CRRs and diffusive decoupling [23, 78]. In this way, we have investigated the rolls of CRRs in or colloidal model in two different yet complementary ways. What follows, Chapters 6 and 7, is a discussion of the results from our published and drafted work.

Part III

Experimental Findings

Chapter 6

Confinement

6.1 Introduction

Phase transitions are usually investigated in the context of macroscopically large systems. However, confining samples so that one or more dimensions are microscopic leads to new physics, including confinement-driven phases [79]. Our interest in this proposal relates to liquids and glasses, or amorphous phases. In particular, the glass transition temperature T_G is often changed for a confined material [80–86]. T_G is defined based on a sharply increasing viscosity, or other standard methods [1, 3–5, 84]. In some experiments, the glass transition temperature is decreased upon confinement [49, 83, 87, 88] –as compared with the transition temperature in bulk–whereas in others, the glass transition temperature increases [80, 81, 87]. In some cases, T_g can increase or decrease even for the same material, depending on the experiment [80, 83, 84, 87]. Computer simulations indicate that confinement influences the arrangement of atoms [49, 87, 89, 90], which might in turn relate to the change of the glass transition temperature. However, it is difficult to directly probe the structure and dynamics of nano-confined materials, especially at a molecular scale.

As discussed in Chapter 2, we study confinement effects using a dense colloidal liquid, a model system which has a glass transition. Colloids are comprised of small solid particles in a liquid; often these are thought of as like hard spheres. When the particle concentration becomes sufficiently high, the sample is analogous to a glass: microscopically it is structurally disordered, yet it behaves macroscopically like a solid rather than a liquid [24]. Much previous experimental work has verified a variety of similarities between the colloidal glass transition and glass transitions in molecular systems [6, 8, 9, 17, 66, 74, 91–93].

My colleagues, in the Weeks Group, have pioneered the technique of fast three-dimensional particle tracking using confocal microscopy [17, 25, 26]. This technique can follow the motion of several thousand colloidal particles in three dimensions and will be used to conduct the experiments. My specific accomplishments in this project include:

- Measure new length scales. As the smallest dimension of the sample L decreases below some value L^*, the dynamics will begin to change. We will determine how L^* depends on the proximity to the glass transition, as well as other experimental details.
- Understand the role of boundary conditions in confinement effects. In molecular glass experiments, important differences are found when studying samples confined on substrates, as compared with free-standing films [80, 84–86]. In other experiments, it matters whether the confining surfaces are hydrophobic or hydrophilic. We can directly observe steric interactions between colloidal particles and features along sample walls that enhance surface roughness.
- Understand the connection between dynamical heterogeneity and confinement. Previous work has shown that particle motion occurs in "cooperative groups" in systems near the glass transition [14, 17, 66, 68, 69, 94–96]; see Ref. [10] for a comprehensive review. We investigate how the morphology of these groups changes in confinement, relating the character of these groups to the overall dynamical and structural changes in the confined colloidal system.
- Understand how particles pack in confinement. We are able to accomplish this goal since we are able to directly observe the three-dimensional coordinates of particles in our confined system. We make direct comparison between our results and simulation, and find excellent agreement.

6.2 Background

A general discussion regarding the background of the glass transition can be found in Chapter 1, but I will reiterate some of its key points here to provide context for our experiments with rotational diffusion.

As a glass-forming liquid is cooled, its viscosity increases smoothly but dramatically by many orders of magnitude. The macroscopic divergence in viscosity is related to the divergence in the microscopic structural relaxation time, or α-relaxation time. A conceptual explanation is the Adams and Gibbs hypothesis, which states that the flow in a supercooled liquid involves the cooperative motion of molecules and that the structural arrest at the glass transition is due to a divergence of the size of these cooperatively rearranging regions (CRRs) [15].

Computer simulations and experiments have explored the sizes and shapes of regions of cooperatively moving molecules as a liquid's glass transition is approached [10, 14]. A direct means of probing the dynamic length scales of glass-forming liquids is by confining them to smaller volumes, such as within thin films and nanopores. Constricting the dynamic length scales that would normally be available to the material can either increase, decrease or even maintain its glass transition temperature T_g [80]. Both simulation and experiment have suggested that the effect on T_g fundamentally depends on the nature of the interaction between the sample and its confining boundary [49, 97–102]. Strongly attractive interactions can result in an increase in T_g whereas repulsive interactions may result in a decrease [84, 100]. Frustration of any structural ordering, via a rough surface for example, can also play a key role, although this can either cause slower or faster dynamics [49, 97, 101]. Whether or not the restriction of the length scales accessible to CRRs is responsible for the variation in T_g remains to be seen due to the inability to directly observe molecular interactions within glass-forming liquids.

Instead of studying molecular glass-formers, we use dense colloidal suspensions of sterically-stabilized micrometer-sized spherical particles. Colloidal suspensions have often been used as experimental models of a hard sphere glass [24, 91]. We confine our samples within a planar volume formed by two quasi-parallel solid surfaces [19]. We use high-speed confocal microscopy to rapidly visualize and acquire three-dimensional images of the particle positions [26]. Subsequent image analysis lets us track the individual particle trajectories, providing an accurate picture of the cooperatively rearranging groups of particles. Near the colloidal glass transition ($\phi_g \approx 0.58$ [24]), particles begin to rearrange in groups characterized by a length scale of ∼3-6 particle diameters [17, 103].

In this series of experiments we further investigate our results from prior experiments [19], focusing specifically on the nature of cooperative rearrangements within the confined sample and how they relate to the system's increased glassiness. In these experiments we found that confinement induces glassy behavior at concentrations in which the bulk behavior is still liquid-like. Here, we show that confining colloidal liquids within this planar volume results in cooperatively rearranging groups of particles that are similarly planar shaped. We find that the flattening shapes of the cooperatively rearranging groups are correlated with the overall slowing of the dynamics, suggesting a connection between confinement, wall-induced structure, and glassy behavior.

Understanding the effects of confinement on the glass transition may help us understand the glass transition in the bulk. Perhaps more importantly, understanding the properties of confined fluids also has direct relevance with lubrication [104], the flow of liquids through microfluidic devices [89, 105], and the kinetics of protein folding [106].

6.3 Experimental Methods

We use spherical colloidal poly-methyl-methacrylate (PMMA) particles that are sterically stabilized to prevent interparticle attraction [24, 25]. A detailed discussion of colloidal PMMA particles is provided in Chapter 2. The particles are suspended in a mixture of solvents, cyclohexylbromide and cis- and trans-decalin, which matches both their density and index of refraction [25]. The viscosity of the solvent is 2.25

Table 6.1: Characteristics of the four samples studied. The number ratio $N_{\text{small}}/N_{\text{large}}$ is determined by counting particles in several fields of view using DIC (differential interference contrast) microscopy. The total volume fraction ϕ_{tot} is determined using confocal microscopy, by counting the number of small particles seen in a given imaging volume, using the known number ratio to determine the number of large particles present, and then using the particle sizes and the imaging volume size to compute ϕ_{tot}. Additionally ϕ_{tot} and $N_{\text{small}}/N_{\text{large}}$ was confirmed in samples B–D by direct 3D confocal microscopy observation, where the particle sizes could be easily distinguished and counted; the results were in agreement with the DIC measurements. The volume fractions of the small species and large species, ϕ_s and ϕ_l, are calculated from the other two quantities. The uncertainties of $N_{\text{small}}/N_{\text{large}}$ are ±5%, and the uncertainties of ϕ_{tot} are ±8%. In particular, note that samples A and C likely do not have the same volume fraction, but it is unclear which has the larger ϕ_{tot}. Samples B, C, and D are prepared by dilutions of one stock sample and thus all have the same $N_{\text{small}}/N_{\text{large}}$.

Sample	$N_{\text{small}}/N_{\text{large}}$	ϕ_s	ϕ_l	ϕ_{tot}
A	3.5	0.26	0.16	0.42
B	3.0	0.13	0.10	0.23
C	3.0	0.24	0.18	0.42
D	3.0	0.26	0.20	0.46

mPa·s at room temperature of 20° C. Section 4.1 includes a thorough discussion regarding solvents. While our sample is similar to other types of colloidal suspensions that act like hard spheres [24], the cyclohexylbromide in our solvent mixture induces a slight charge on the surfaces of the particles, discussed in Sec. 4.1.1. Thus, the particles have a slightly soft repulsive interaction in addition to their hard sphere core. To prevent crystallization, which would be readily induced by the smooth walls in our thin planar geometry [47–50], we use a binary mixture of particles with hydrodynamic radii of $a_{\text{small}} = 1.18$ μm and $a_{\text{large}} = 1.55$ μm, a technique discussed in Sec. 4.2. The number ratio is approximately $N_S/N_L = 3.5$, and the individual volume fractions are approximately $\phi_S = 0.26, \phi_L = 0.16$, so the total overall volume fraction is $\phi = 0.42 \pm 0.05$. The uncertainty of ϕ arises from the difficulty in precisely determining the individual species' particle size, the polydispersity of particle sizes ($\sim$ 5% for both species), and difficulties in determining the relative volume fractions of the two species. A study of a similar colloidal mixture found the glass transition volume fraction (for bulk samples) to be at $\phi_g \approx 0.58$ [107]. We examine four different samples A-D, with properties listed in Table 6.3.

Our goal is to study our sample with a range of confinement thicknesses. Here we focus on "thin film like" confinement between two flat surfaces. We achieve this by constructing a wedge shaped sample chamber, as described in Sec. 4.3.1 and shown in Fig. 4.2. We build the chamber using a glass slide, a rectangular glass coverslip, and a narrow piece of a ∼60 μm thick Mylar film, employing a method similar to the one used by Refs. [47, 51].

Using UV-curing epoxy (Norland 68) we attach the Mylar film near one end of one side of the glass slide so that it runs perpendicular to the slide's length. Next, the glass coverslip is laid across the slide so that one end is raised up by the Mylar film. Meanwhile, the coverslip's opposite end is clamped down, ensuring the thinnest gap size possible. We seal the sample chamber shut with epoxy, except for two small air holes; the sample is added via one while air escapes via the other. After adding the sample, the two openings are sealed with epoxy. The chamber's shape is depicted in Fig. 4.2: a very long chamber with a broad range of thicknesses. Due to the Mylar film, the glass surfaces are not parallel but very slightly angled at 0.4° relative to one another.

Within our field of view, the change in our sample's thickness due to our sample chamber's slight taper is less than 0.3 μm, which is negligible for all but the thinnest regions. We do not see any influence of the taper in any of our results (discussed further below), suggesting it is reasonable to consider the two boundaries as locally quasi-parallel. We define y as the direction along which H varies.

We use laser scanning confocal microscopy to view the sample [25, 26], discussed extensively in Chapter 3. We can acquire a three-dimensional image of the sample by scanning a $50 \times 50 \times 20$ μm^3 region (equal to $256 \times 256 \times 100$ pixels). We use Visitech's "vt-Eye" confocal system which can scan this volume in 2.0 seconds. This is much faster than the time for particles to diffuse their own diameter, which is ∼100 seconds in our samples. We acquire sequences of three-dimensional (3D) confocal images every 2.0 seconds for up to ∼40 minutes. By scanning different locations, we observe the behavior at different thicknesses H ranging from ∼6 μm to ∼19 μm in addition to the sample's bulk. Data representing the 'bulk' of our sample is acquired from a 20 μm thick sub-volume in the thicker region of the sample chamber that is over 15 μm away from the chamber's walls in order to avoid any boundary effects.

The small particles are dyed with Rhodamine dye [25] and the larger ones are left undyed. Thus the data in our results are for the smaller particles only. Each image is post-processed to find particle positions with an accuracy of 0.05 μm in x and y (parallel to the walls) and 0.1 μm in z (perpendicular to the walls, and parallel to the optical axis of the microscope). Given that the particles do not move much between images, we can link the particle positions in time to get 3D trajectories of the particles' motion throughout the sample volume [25, 55]. Fluorescent dye and particle tracking are discussed in Sections 2.3 and 5.1, respectively.

6.3.1 Stuck Particles

The glass surfaces of the cover-slip and slide are untreated. In experiments with sample A, we find that when we fill our slides with sample, a small fraction of particles stick to the sample chamber's walls. Typically less than 20% of the walls' area is coated with stuck particles [20]. In a second series of experiments done with samples B–D, no particles were stuck. Reassuringly, we find little dependence of the behavior on the number of stuck particles in the results discussed below. The stuck particles are easy to identify as their apparent motion, due to noise inherent to particle tracking, is much less than the other particles. An image showing the locations of some stuck particles is shown in Fig. 6.1. Other observations confirm that both large and small particles stick to the walls [20]. We find that the particles stick to the surfaces of the glass slides only during the initial loading of the sample chamber with colloid. The stuck particles remain stuck indefinitely, through a van der Waals attraction to the glass, and may therefore be regarded as a permanent feature of the surface. The mobile particles, which diffuse in solution, do not begin sticking to the sample's glass boundaries over time – during the course of the experiment they are not observed to stick, and over a long time (months) the amount of particles stuck to the glass does not appear to change. In fact, the mobile particles are repelled from the glass boundaries by a relatively weak Coulombic interaction; in other words, during the experiment, the particle-wall interaction is a weakly repulsive one. Particles interact with the wall hydrodynamically, which we show by measuring particle mobility in a dilute suspension near the glass walls. We show these results in Fig. 6.2, where we plot the Cartesian components of the diffusion coefficients of particles over a range of distances from the coverslip's surface using Eqn. 5.28. The behavior was in good agreement with Faxen's Law [108, 109], which is a correction to Stoke's law for the drag coefficient of a spherical object near a surface. Faxen's law is expressed as

$$\beta = \frac{6\pi\eta a}{1 - \frac{9}{16}\frac{a}{z} + \frac{1}{8}\left(\frac{a}{z}\right)^3 - \frac{45}{256}\left(\frac{a}{z}\right)^4 - \frac{1}{16}\left(\frac{a}{z}\right)^5}, \tag{6.1}$$

where β is a drag coefficient, a is the particle radius, and z is the distance between the surfaces of the coverslip and the particle. The apparent upturn or spike in D_z near the boundary is most likely due to the combination of poor optical resolution in the z direction and relatively low statistics over the range of z near the coverslip, where particles feel the aforementioned slight electrostatic repulsive force.

Stuck particles, however, have proven to be a very valuable feature of our experiments. For sample A, measuring the positions of the stuck particles allows us to accurately measure the sample thickness. While the uncertainty in locating individual particle positions in z is 0.1 μm, by averaging data from tens of stuck particles over hundreds of images we locate their mean z position to better than 0.005 μm. Thus the effective thickness H of each experimental data set is determined to within 0.01 μm, and is the range in z available to the *centers* of the visible particles. We report the thicknesses in terms of H. The true surface-to-surface thickness of a sample chamber is found by adding $2a_{\mathrm{small}} = 2.36$ μm to H. Noe that the uncertainty of a_{small} implies a systematic uncertainty for the true surface-to-surface thickness. The larger particles with radius a_{large} , which are invisible to the confocal microscope, have

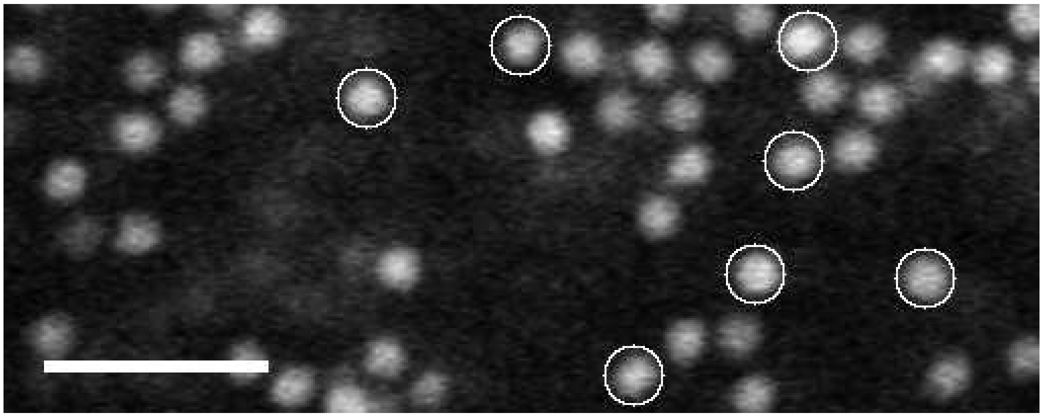

Figure 6.1: Typical 2D confocal microscope image showing particles immediately adjacent to one of the chamber walls. The circled particles are stuck to the glass, and the others move freely. Note that there are also undyed particles also stuck to the surface, as well as undyed mobile particles, which are not visible in this confocal image. The scale bar indicates 10 μm.

a slightly smaller range in z available to them, that is, $H + a_{\mathrm{small}} - a_{\mathrm{large}}$.

In addition to allowing accurate measurement of sample thickness, tracking the stuck particles provides a mean trajectory of the sample's frame of reference. Slides, and to a much lesser extent microscope stages, are known to drift over the course of our experiments, several hours in duration. We can address this type of systemic error by subtracting the very slight motions of the stuck particles from the trajectories of the mobile suspension.

6.4 Results

6.4.1 Wall-induced structure

For the first series of experiments, we study the behavior of sample A ($\phi \approx 0.42$) as a function of thickness. Accurate measure of the sample chamber's local thickness is done by calculating the number density $n(z)$ as a function of the distance z between the walls, shown in Fig. 6.3 for (a) the mobile particles and (b) the stuck particles. The maximum of each peak in (b) corresponds to the approximate position in z of the *centers* of the small particles stuck to the sample's walls. These positions indicate the maximum possible extent for the centers of the free particles. The centers of the stuck particles are indicated by the dashed lines in Fig. 6.3, whose separation indicate the *effective* local chamber thickness H. Since only the small particles are visible to the microscope, the actual thickness is $H + 2a_{\mathrm{small}} = H + 2.36$ μm. The mean particle radii are known only to within ±0.02 μm, while our uncertainty in their z positions

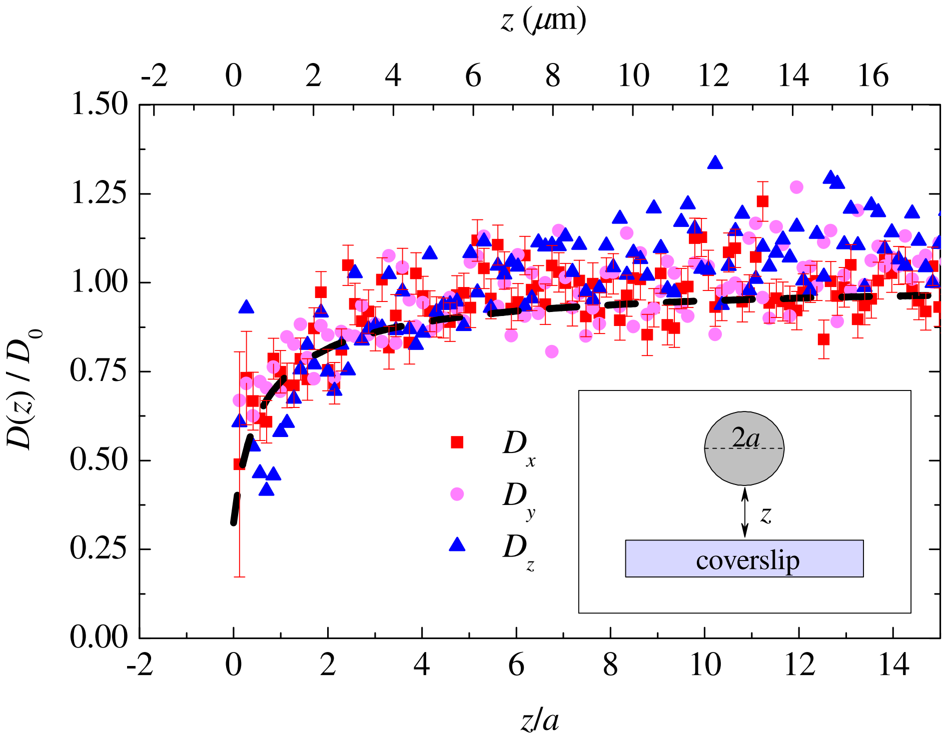

Figure 6.2: Measurements of local diffusion constants as a function of the distance z to the wall, normalized by the small particle radius $a = 1.18$ μm. The dashed line is a prediction calculated from Faxen's Law, shown in Eqn. 6.2 [108, 109]. Inset: sketch indicating that $z = 0$ corresponds to the particle touching the wall.

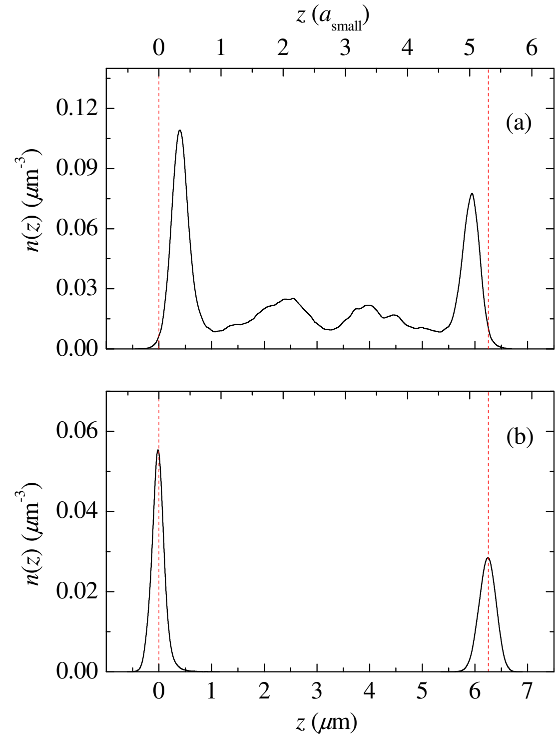

Figure 6.3: The number density n as a function of the distance z between the walls. (a) All mobile and visible (dyed) particles (b) All immobile and visible (dyed) particles. The vertical lines in both indicate the position of the centers of the visible particles stuck to the walls. For this data, the distance between the two positions is $H = 6.25$ μm, the effective local chamber thickness.

is 0.1 μm. By averaging over tens of stuck particles we can determine H to within 0.01 μm.

Figure 6.3(a) shows layering of particles near the sample walls, which has been seen in both computer simulations [49, 110] and experiments [47, 111]. However, comparing Fig. 6.3(b) to (a) we see that the boundary layers of the mobile particles are offset from those of the stuck particles. The offset is most likely due to Coulombic repulsion between the glass walls and PMMA particles. Using DIC microscopy, we confirmed that the large particles also form layers, albeit in positions shifted due to their size; the results are qualitatively in agreement with simulations that studied layering of binary mixtures of particles near walls [112].

Figure 6.4 shows the way layering changes with H. The peaks of $n(z)$ are tallest and thinnest next to the walls. Subsequent layers are shorter and wider, presumably as the correlations between particle positions become diluted through the presence of two particle sizes [112]. Note that we do not see any "quantization" effects for particle values of H. Some packing effects were seen in simulations at $H = 2ma_{\mathrm{small}} + 2na_{\mathrm{large}}$

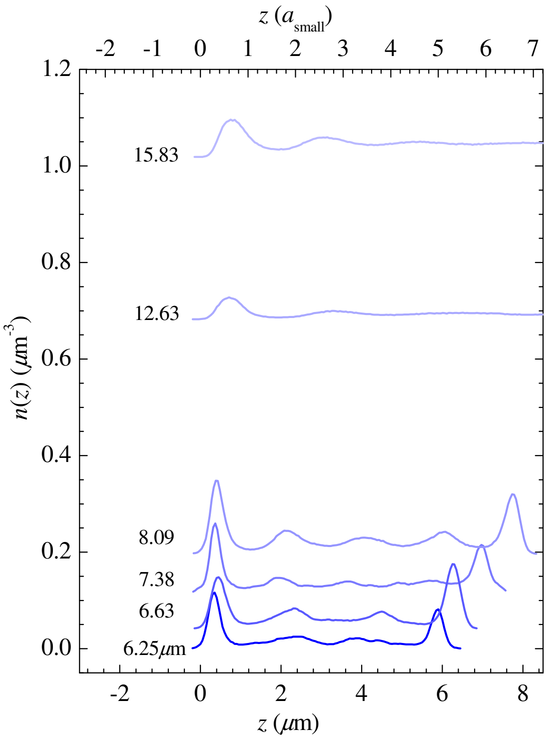

Figure 6.4: Number density n as a function of the distance z between the walls. The thickness H is as labeled (in microns). The values of H in terms of $a_{\rm small}$ are 5.30, 5.62, 6.83, 6.86, 10.7, and 13.4. The curves are vertically offset for clarity, where the offset is proportional to H.

for integer values m, n, but these effects are too subtle to be resolved given the relatively few values of H for which we have experimental data [112].

The layering that we observe is in good agreement with work by Dullens and Kegel [111], where they observed that the presence of a wall induces quasi-two-dimensional (q-2D) ordering of a dense colloidal suspension (a single-species sample with a polydispersity of 6%). Particles in the layer next to the wall had similar phase behavior to that predicted for pure two-dimensional hard sphere systems. This phase behavior was attributed to the narrowness of the density layers along the walls. In our experiment, the highly ordered, yet non-crystalline, q-2D layers along the walls serve as a template for subsequent layering into the sample's interior.

6.4.2 Sample-averaged dynamics

Before we consider the specific influence of the particle layers on the particle motion, we will quantify the average motion of the sample. This is done by calculating the mean square displacement (MSD) as

$$\langle \Delta x^2 \rangle = \langle [x_i(t + \Delta t) - x_i(t)]^2 \rangle_{i,t} \tag{6.2}$$

where the average is taken over all particles i and all initial times t. An analogous formula applies for $\langle y^2 \rangle$ and $\langle z^2 \rangle$. We find that $\langle \Delta x^2 \rangle \approx \langle \Delta y^2 \rangle$ for all our experiments; we report our results for the x direction, the direction over which the sample chamber has constant thickness. An in-depth discussion of the MSD and its significance can be found in Sec. 5.3.1. The data in Fig. 6.5 are from a series of experiments with Sample A, with $\phi \approx 0.42$, for different thicknesses H.

We first consider the results for motion parallel to the confining plates, $\langle \Delta x^2 \rangle$, shown in Fig. 6.5(a). The upper lines shows motion in an unconfined region and is reproducible for all chamber thicknesses $H > 15.5$ μm. For this sample, the motion in the unconfined region is nearly diffusive, with the MSD growing almost with slope 1 on the log-log plot. This behavior is similar to monodisperse samples with a volume fraction of $\phi \leq 0.4$ [17]. In other words, this sample is far from the glass transition, $\phi_g \sim 0.58$ [113, 114]. For values less than $H \approx 16$ μm ≈ 14 $a_{\text{small}} \approx 10$ a_{large} we observe a systematic slowdown. Note that Fig. 6.5(a) shows a log-log plot and thus for the thinnest region shown (bottom curve, $H = 6.25$ μm), to move a distance $\langle x^2 \rangle = (a_{\text{small}}/3)^2$ it takes a time scale 200 times larger than for the bulk region data ($\Delta t = 400$ s as compared to 2.0 s).

To contrast the mobility in the parallel and perpendicular directions, in Fig. 6.5(c) we plot $\langle x^2 \rangle$ and $\langle z^2 \rangle$ separately for a selection of three thicknesses. Not surprisingly, being perpendicular to the wall, motion in the z-direction is less. Furthermore, the upturn of the MSD at large Δt is barely beginning for the z data. The contrast between the x and z motion suggests that cage rearrangements may favor motions parallel to the walls.

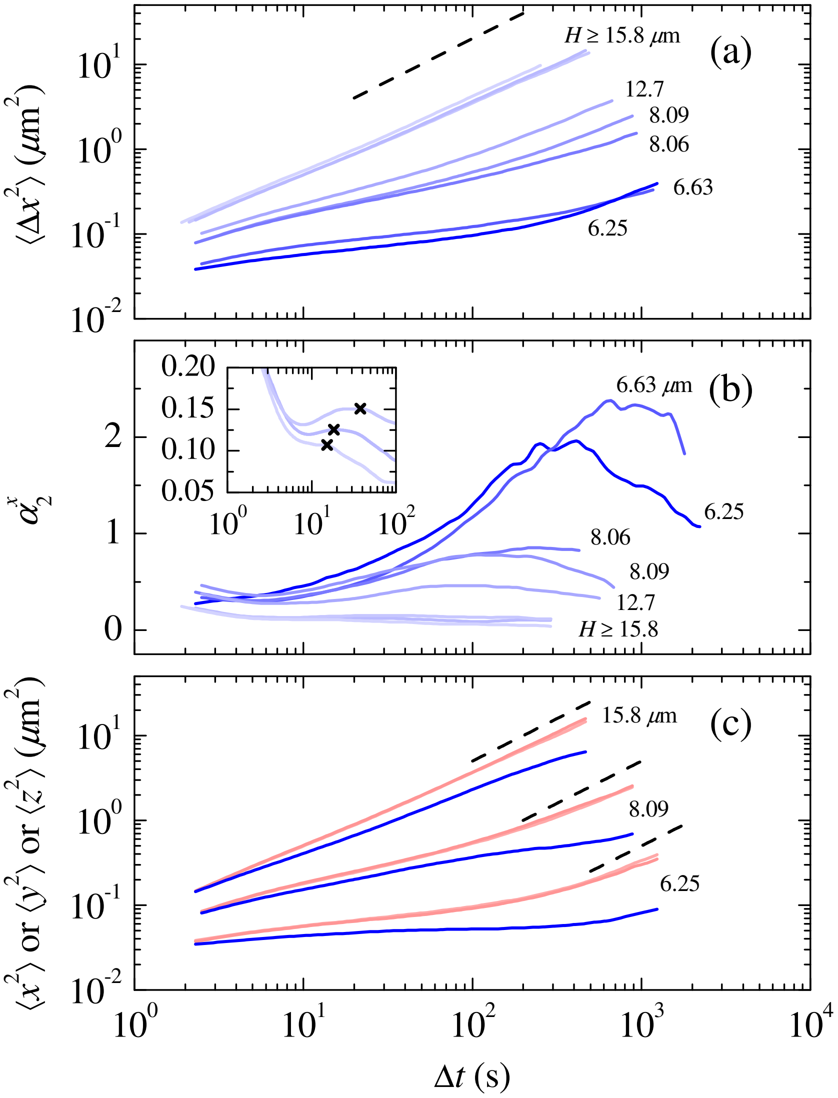

Figure 6.5: (a) The mean square displacement for our sample over a range of thicknesses [19]. The dashed line has a slope of 1.0. (b) Plots of the corresponding non-Gaussian parameter for each thickness [21]. The x superscript of α_2^x is to indicate that the non-Gaussian parameter is only calculated using the x displacements (parallel to the wall, and perpendicular to the slight gradient in H). The inset is a magnification of the curves for $H \geq 15.8$ µm, with each curve's local maxima labeled, corresponding with Δt^* for the data at these thicknesses. (c) Components of the MSD curves. Red curves are the x- and y-components of motion (parallel to the walls) and the blue are the z-component of motion (perpendicular).

In Fig. 6.5(a), the upturn at the end of the plateau in $\langle \Delta x^2 \rangle$ is the result of cage rearrangements [17, 74, 93, 97]. This is the inhibited motion of a particle due to its "cage" of neighboring particles [74, 93, 115–117]. For a complete discussion of cage-breaking dynamics and how it relates to plots of the MSD, refer to Chapter 5. At the earliest times ($\Delta t < 1$ s, not shown), particle motion is diffusive as particles have not moved far enough to encounter the cage formed by the neighboring particles [118, 119]. As the particle displacement becomes larger, its motion is impeded by its neighbors which form the cage, resulting in the plateau in $\langle \Delta x^2 \rangle$ for $\Delta t < 100$ s. The neighbors rearrange and this lets the caged particle move to a new position, perhaps with some of the same neighbors. The motion of particles at longer lag times is diffusive due to the uncorrelated cage rearrangements, and the motion has a greatly reduced diffusion coefficient D_∞ [74]; this is not quite seen in our data sets here as the time scales for this diffusive motion is longer than our observation times. The decreasing plateau height for smaller values of H seen in Fig. 6.5(a) suggests that the cage size decreases in more confined samples. The results in Fig. 6.5(a) are for Sample A, with $\phi \sim 0.42$; the results from samples C & D with a higher ϕ, shown in Fig. 6.6, demonstrate that the onset length scale for the confinement-induced slowdown increases [19]. The cage size may be due to the width of the layers in our system which narrow with decreasing H (see Fig. 6.4). As the density within a layer increases, particles within the layer become more crowded, which would suggest that the cage size decreases.

Equilibrium Behavior and Structure

It could be argued that by inducing structural order in our colloidal fluid we are not modeling glassy behavior at all, but instead observing some kind of nematic or smectic phase behavior. In other words, it is conceivable that there is some kind of true equilibrium crystalline state that incorporates highly ordered structural layers that we observe. This would suggest that we are merely observing the colloid while it is en route to some kind of nematic or other type of ordered phase.

However, recent simulations of confined hard sphere systems [120, 121], in a configuration very similar to our own, support our belief that our particular colloidal system is actually in a sort of meta-stable equilibrium. The findings of Ref. [121] state that although confinement strongly affects local structuring, the relationships between self-diffusivity, excess entropy, and average fluid density are, to an excellent approximation, independent of channel width or particle-wall interactions. Thus, thermodynamics can be used to predict how confinement impacts dynamics, supporting our assertion that we are not observing our system in some kind of transient phase, but really it is in a very robust meta-stable equilibrium. We say metastable because over the course of many months, in fact years, the bidisperse colloid has been observed to phase separate into large and small particle species. Alternatively, as has been suggested by colleagues, the phase separation could be due to a "drying out" of the colloid, where the solvent phase very slowly leaks through the epoxy used to seal the sample chamber. In this way, the particles would be drawn toward the edges of the sample, an effect that is not due to simple confinement, but a more complex effect specific to our sample chambers.

In short, our experiments are investigating an equilibrated fluid that is amorphous, barring the formation of layers. It would be valuable to totally frustrate layering, while still confining the sample, in order to distinguish the role of confinement specifically versus the effect of layering.

6.4.3 Confinement Length Scale

As our samples consist of particles of two sizes, we use naturally occurring variations in the number ratio $N_{\mathrm{small}}/N_{\mathrm{large}}$ as an additional parameter to understand confinement effects. While we cannot directly count the number of large particles, we can count the small ones, and it is reasonable to assume that the overall volume fraction does not vary much in confinement [90]. This is supported by DIC microscopy observations. Thus, a larger measured N_{small} implies a smaller N_{large}. In the bulk region, the number density $n_{\mathrm{small}} = N_{\mathrm{small}}/V$ is reasonably constant (using the observation volume V which is large). In confined regions, the acquisition volume V is based on the size of the imaging window in x and y, and the observed thickness H in z. For smaller H, we see differences in n_{small} from region to region, influencing the observed motion, as can be seen in Fig. 6.5(a, c). For the bottom two pairs of curves in Fig. 6.5(a) the thickness H is similar but the small particle number density is larger for the top curve of each pair. (Values of H and n_{small} are listed in Table 6.2.) These results make sense: a larger value of n_{small} means that more of the particles are small, and thus the effective thickness in terms of the particle size is larger.

Some of the variation of the MSD curves of Fig. 6.5(a) are likely due to composition differences between sample regions. While the sample is well-mixed, any given region will have a random fluctuation in the number ratio $N_{\mathrm{small}}/N_{\mathrm{large}}$. While we cannot directly measure the number ratio due to the invisibility of the large particles, the observed volume fraction ϕ_S of the small particles is a good indication of local composition. For the data shown in Fig. 6.5, the small particle volume fractions are listed in Table 6.2. Consider the data for $H = 8.09$ μm and $H = 8.06$ μm: the latter MSD curve shows faster dynamics in Fig. 6.5(a), and corresponds to a higher ϕ_S. Likely, given the greater proportion of small particles present in this data set, the sample is *effectively* thicker, resulting in faster motion. Again, an increase in $N_{\mathrm{small}}/N_{\mathrm{large}}$ would result in a greater number of particles fitting within a volume, thereby modeling a thicker layer of material. A similar argument can be made for the $H = 6.25$ μm and $H = 6.63$ μm data. It is also possible that the dynamics are faster simply because the small species diffuse faster than the large species, so even a bulk sample with a larger fraction of small particles would be expected to have faster motion as there are fewer large particles to move around. An additional example can

Table 6.2: The effective thickness of each data set, from Sample A (See Table 6.3), with the corresponding small particle volume fraction ϕ_{S}.

H (μm)	6.25	6.63	8.06	8.09	12.7	15.8	Bulk
ϕ_{S}	0.140	0.197	0.199	0.219	0.0908	0.186	0.206

be seen in data from $H = 12.7$ μm, which exhibits less mobility than anticipated due to an anomalously low ratio of small to large particles, as indicated in Table 6.2.

As noted earlier in this and other chapters, the growth of dynamic length scales has been observed as the glass transition is approached in a bulk material [10, 17, 66, 80, 103]. For our colloidal samples, this implies that samples with a larger ϕ should exhibit stronger confinement effects. To check this, we took data from samples B, C, and D at various thickness. Qualitatively the data resemble that shown in Fig. 6.5(a). To capture the H dependence, Fig. 6.6 shows the values of $\langle \Delta x^2 \rangle$, at fixed $\Delta t = 100$ s, as a function of H for the different samples. Consider the solid triangles, corresponding to sample D. For $H > 50$ μm, $\langle \Delta x^2 \rangle$ is essentially constant. At $H < 50$ μm, the data start showing a strong H dependence, suggesting a confinement length scale of $H^* \approx 50$ μm. For the solid symbols, an increase in H^* is seen as ϕ increases, from approximately 10 μm to 50 μm, confirming that there is a growing length scale as the glass transition is approached. These length scales are significantly larger than those seen for dynamical heterogeneities in monodisperse samples, which are $4 - 8$ μm [103]. However, this agrees with simulations which found a confinement length scale significantly larger than the mobile cluster size [87, 97]. In Fig. 6.6, sample A has a smaller value of H^* relative to sample C, which may be due to the excess of small particles in sample A; see Table 6.3.

The MSD curves show an overall slowing down due to confinement, but obscure the influence of the density layers on the motion. Figure 6.7(a) shows the number density for one data set. In panels (b) and (c) we plot the components of the MSD, for fixed values of Δt, that are perpendicular and parallel to the walls. The dips in $\langle z^2 \rangle$ [Fig. 6.7(c)] coincide with the layers in panel (a) and imply that particles within layers are in a preferred structural configuration and are less likely to move elsewhere [19, 49, 110, 122].

Surprisingly, the layers do not appear to influence the motion parallel to the walls, as seen by $\langle \Delta x^2 \rangle$, which does not depend on z. An absence of boundary effects on parallel motion seems counterintuitive as hydrodynamic interactions with the wall normally result in reduced motion for nearby particles [123]. We speculate that the cage dynamics dominate particle motion, rather than hydrodynamic influences. For example, if a particle is pulled by an external force in a direction parallel to the walls, other particles would be forced to rearrange, which is probably the most significant contribution to the drag. Particle rearrangements would be even more constrained for

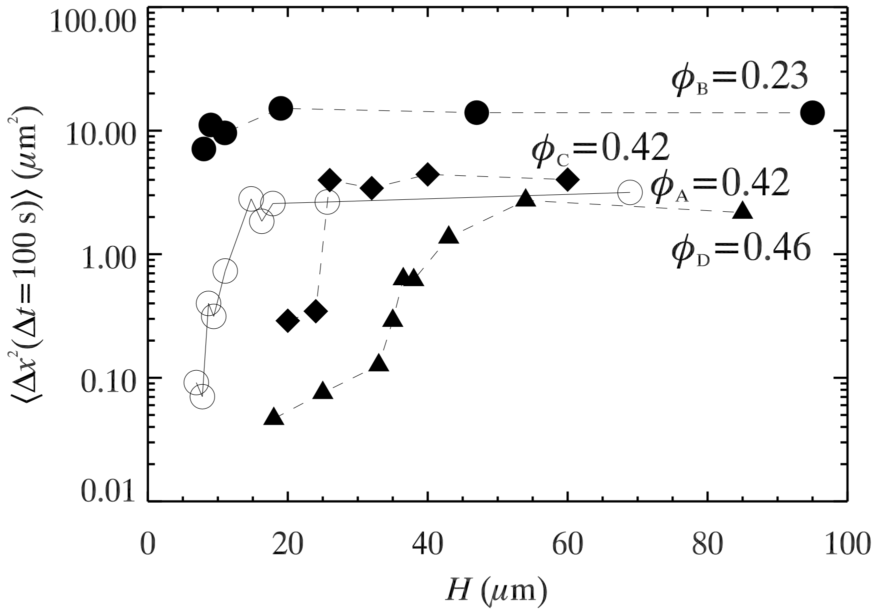

Figure 6.6: Value of $\langle \Delta x^2 \rangle$ at $\Delta t = 100$ s, as a function of thickness H, for samples with ϕ as indicated. The open circles correspond to sample A with $N_{\text{small}}/N_{\text{large}} = 3.5$, while the solid symbols correspond to samples B–D with $N_{\text{small}}/N_{\text{large}} = 3.0$. The lines are drawn to guide the eye. The plateau for each data set indicates behavior corresponding to the bulk, whereas the downturn at low H gives an idea of the length scale at which confinement becomes important.

a particle pulled perpendicular to the wall, thus explaining why we observe slower z motion. Simply put, the high volume fraction likely results in hydrodynamic screening.

Thus while confinement causes the layering of particles near the walls, this layering does *not* appear directly responsible for the slowing of the particle motion. Rather, the layering seems to be an additional influence on the motion in the direction perpendicular to the walls, as seen in Fig. 6.7(c), but only a minor influence compared to the overall fact of confinement. Note that results do not appear to depend on having an integral number of well-defined layers between the walls [89]. The overall dynamics slow smoothly and monotonically as the confining dimension decreases.

Our observation that the layers closest to the wall have slower motion perpendicular to the walls agrees qualitatively with previous experiments [82, 83, 88] and simulations [87, 97] which suggested that surface layers may be glassier than the interior. However, we note in our experiment this is strongly directionally dependent. The slowing is most easily seen if $\langle \Delta z^2 \rangle$ can be measured independently of the other two directions. Overall, the influence of the layers appears to be a secondary one, with the primary influence on the motion being the fact of confinement. For comparison to a bulk-like thickness of $H = 15.8$ μm, we have included a similar set of plots in Fig. 6.8.

The difficulty in particle mobility normal to the walls can be explained by the work of Dullens and Kegel on the interaction between colloidal particles at a smooth glass surface [111, 124]. In an experimental configuration similar to our own, quasi-two-dimensional (q-2D) layers of particles formed along the surface of a glass slide in a bulk polydisperse colloidal suspension. The wall-based particles seemed unable to leave their q-2D layer, exhibiting two-dimensional behavior that is fundamentally distinct from the dynamics of the particles further from the wall [111, 124]. Note that wall-based particles in dense colloidal suspensions, such as our own, behave significantly different from those in dilute liquid-like suspensions [125]. In our experiments, the particle layers near the wall become more pronounced with decreasing H, suggesting that these layers become more q-2D. While the q-2D nature of these layers may partially explain their slow motion, Fig. 6.7 shows that slowing is not restricted to these layers alone.

6.4.4 Defining cooperatively rearranging regions

The features of our $\langle \Delta x^2 \rangle$ curves resemble those of bulk supercooled colloidal liquids, where cage rearrangements play a significant role in the material's underlying dynamics. The process of cage rearrangements leads to a liquid's overall structural relaxation [4, 64]. Adam and Gibbs were the first to hypothesize the existence of "cooperatively rearranging regions" (CRRs) as a supercooled liquid's means of increasing its configurational entropy [15]. Conceptually, prior simulations [14] and experiments [17, 66] have defined these cooperative regions simply as groups of neighboring

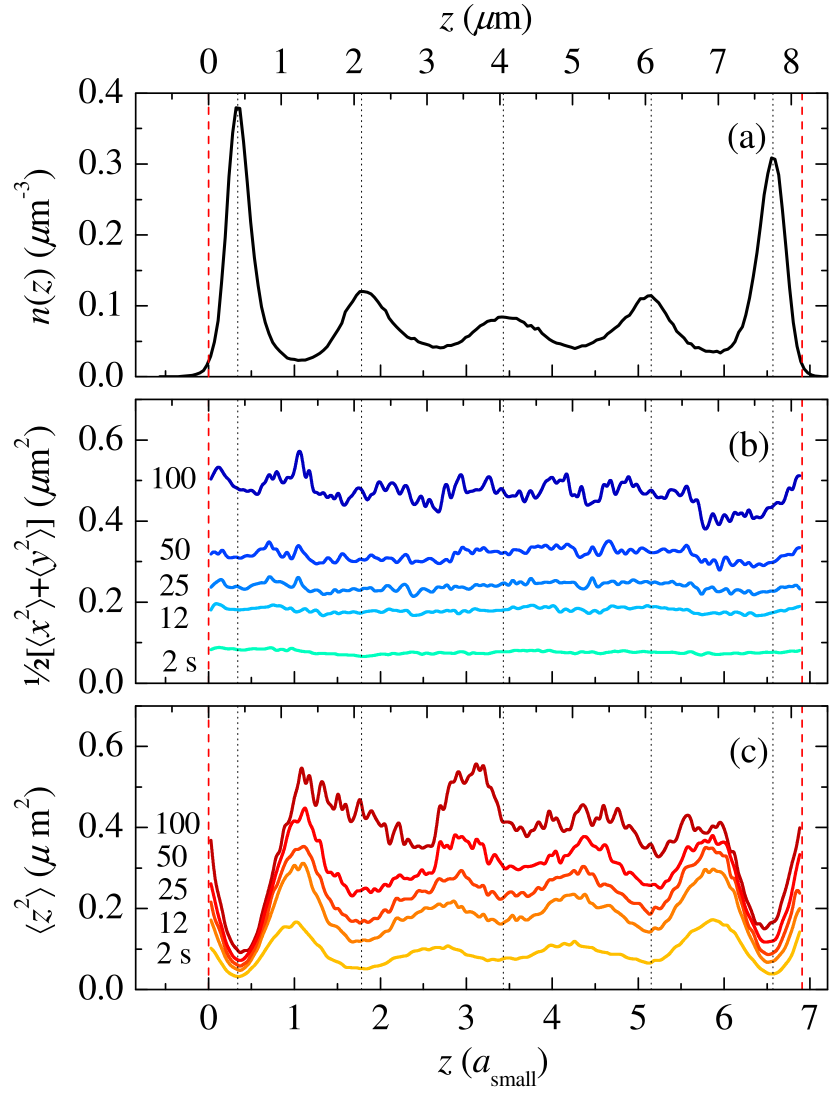

Figure 6.7: (a) Particle number-density $n_{\text{small}}(z)$ as a function of distance z across the sample cell. Additional particles are permanently stuck to the walls of the cell (not shown) which have centers located at $z = 0.00$ μm and $z = H = 8.06$ μm, indicated by the vertical dashed lines. These data correspond to the $H = 8.06$ μm data in Fig. 6.5. (b) Mean square displacement parallel to the walls ($\frac{1}{2}[\langle \Delta x^2 \rangle + \langle \Delta y^2 \rangle]$) and (c) perpendicular to the walls ($\langle \Delta z^2 \rangle$) as a function of the particles' initial positions z. The displacements are calculated using a range of Δt, as labeled. The dotted lines indicate the position of the number density maximum of each layer in (a) while the dashed lines correspond to the approximate position of the centers of the particles stuck to the glass walls.

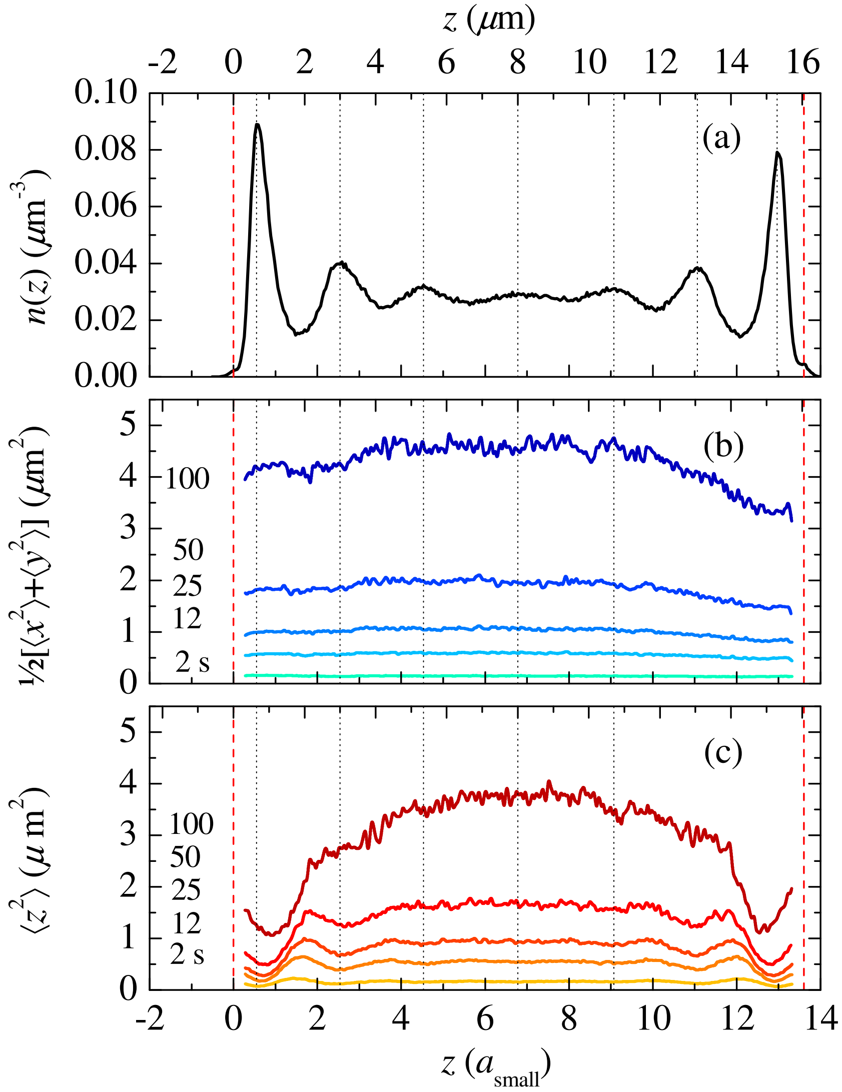

Figure 6.8: (a) Particle number-density $n_{\mathrm{small}}(z)$ as a function of distance z across the sample cell. Additional particles are permanently stuck to the walls of the cell (not shown) which have centers located at $z = 0.00$ μm and $z = H = 15.8$ μm, indicated by the vertical dashed lines. These data correspond to the $H = 15.8$ μm data in Fig. 6.5. (b) Mean square displacement parallel to the walls ($\frac{1}{2}[\langle \Delta x^2 \rangle + \langle \Delta y^2 \rangle]$) and (c) perpendicular to the walls ($\langle \Delta z^2 \rangle$) as a function of the particles' initial positions z. The displacements are calculated using a range of Δt, as labeled. The dotted lines indicate the position of the number density maximum of each layer in (a) while the dashed lines correspond to the approximate position of the centers of the particles stuck to the glass walls.

molecules or particles that collectively rearrange their positions in order to realize a new position in space.

The precise definition of a cooperatively rearranging region is open to interpretation. Our definition is described below, and is comprised of three key elements: (1) the time scale used to determine displacements, (2) the threshold for considering a displacement to be a "rearrangement," and (3) the definition of which particles are adjacent, such that their motion is "cooperative." A general discussion of identifying cage-breaking events is also provided in Sec. 5.3.3.

We start by defining the time scale of interest. Prior work has found that a good choice is based on the shape of the probability distribution of displacements [17, 69, 93, 126] Rearranging particles have displacements which are larger than normal, and thus lie in the tails of the distribution. While these displacements are rare, they are less rare than a Gaussian, and these statistical outliers are nonetheless responsible for the upturn in the MSD at large lag times [14, 17, 66, 68, 69]. The importance of the outliers is quantified by calculating the non-Gaussian parameter α_2,

$$\alpha_2(\Delta t) = \frac{\langle \Delta x^4 \rangle}{3\langle \Delta x^2 \rangle^2} - 1, \tag{6.3}$$

from Ref. [70]. The maximum of α_2 defines the cage rearrangement time scale Δt^*. We plot $\alpha_2(\Delta t)$ in Fig. 6.5(b) and find that both the maximum value of α_2 and the time scale Δt^* increase with decreasing H. For data from $H \geq 15.8$ μm, the levels of noise at low values of Δt are seemingly more non-Gaussian than the actual particle dynamics. Despite the noise, for $\Delta t > 10$ s there are secondary local maxima of α_2 that we consider to be a better approximation of Δt^* [see the inset plot of Fig. 6.5(b)]. We plot Δt^* versus H in Fig. 6.11(a), which decays roughly exponentially with H until $H \approx 20$ μm, at which it reaches the bulk value. Simply put, as H decreases more particles have anomalously large displacements, and the time scale for these displacements grows rapidly.

Given the variation of $n(z)$ at a given H, shown in Fig. 6.4, it is conceivable that Δt^* would also vary with z. Unfortunately, we have insufficient data to conclusively investigate the behavior of $\alpha_2(z, \Delta t)$ for a given H. However, the z-averaged determination of Δt^* is sufficient for our purpose, which is to set a time scale for considering CRRs.

To define the length scale which separates a "rearranging" displacement from a "caged" displacement, we use a mobility threshold Δr^*. Both experiments [17, 71] and simulations [72] have used a displacement threshold to define mobility such that over time, some percentage of the particles have displacements $|\Delta \vec{r}| \geq \Delta r^*$ [14, 72], although at any given time the exact fraction may not be exactly this percentage. Thresholds of the top 5th percentile [17, 72, 73], 8th percentile [74], 10th percentile [71], and 20th percentile [45] have all been used to define Δr^*. From examining distributions of Δx and Δy for our data, we find that the slowest 90% of the displacements are well described by a Gaussian distribution, whereas the top 10% are more probable

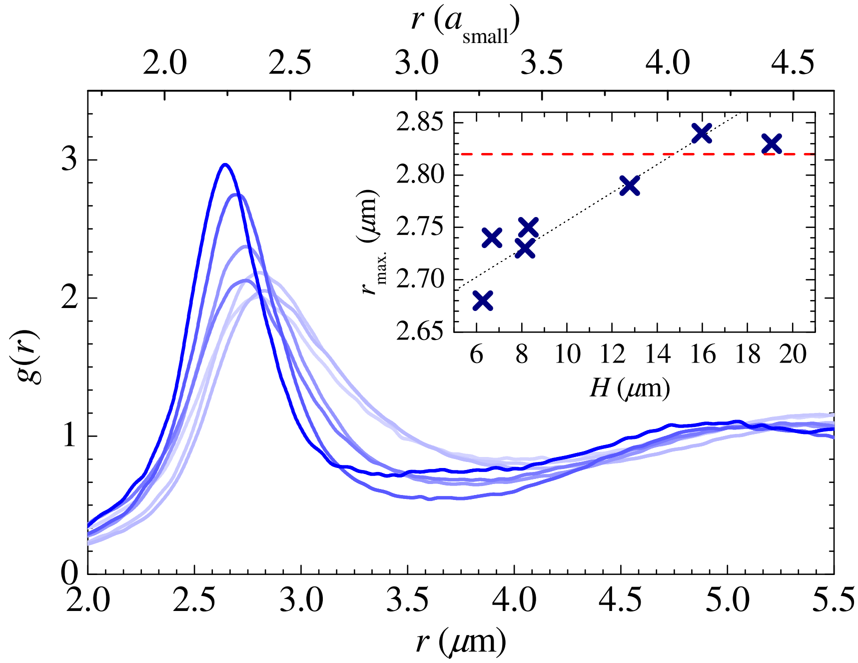

Figure 6.9: The pair correlation function $g(r)$ for a range of H. Darker curves correspond with thinner samples. The curves are from samples with thickness H equal to 6.25, 6.63, 8.09, 12.6, 15.8, and 18.9 μm, along with one curve for the sample's bulk (the lightest color curve). The inset shows the position of the first peak as a function of H. For hard spheres, this position would be expected to be constant, and the slight shift in the peak position is likely due to the slight charge of the particles and layering induced by the boundaries. The red horizontal dashed line indicates $r_{\rm max}$ for the bulk sample, while the diagonal dotted black line is only a guide to the eye.

than a Gaussian distribution would predict; the threshold of $10 \pm 1\%$ for this is valid for our range of H. Thus, we define our mobility threshold as the top 10% of the most mobile particles. Displacements in the z-direction, however, vary significantly with H, making their inclusion in the calculation of our threshold impractical. As is the case with prior studies [14, 17], our choice of Δr^* is somewhat arbitrary and our results are robust to some variation of Δr^*.

To complete our identification of CRRs we must identify which highly mobile particles are simultaneously nearest neighbors. Two methods of determining nearest neighbors are (1) the use of 3D Delaunay tessellations of particle positions [17, 75] and (2) the definition of a minimum separation as a cutoff distance set by the first minimum of the pair correlation function $g(r)$ [73, 74]. Given that we cannot see the large particles, it is problematic to compute the Delaunay triangulation, and so we use method (2) and calculate $g(r)$. Our distributions of $g(r)$ do not vary substantially with H, as shown in Fig. 6.9. The minimum distance between nearest neighbors, the position of the first minima, does grow with H, from ∼3.4 μm to ∼4.1 μm. We use the average value, 3.87 μm, to define particles which are nearest neighbors.

The minor shift of peak position of $g(r)$ with H can be explained in terms of layering, the charge interaction between particles, and the slight variations in the relative concentration of either particle species (See Table 6.2). In the bulk, the particles tend to repel one another due to their slight surface charge, whose screening length is greatly reduced by free ions within the solution [28]. As the sample becomes thinner, a greater proportion of particles reside along or are very near the sample chamber's walls [19, 112]. Along a smooth surface, it is entropically favorable to form ordered layers versus the now latent particle-particle charge repulsion. Within the layers, particles are relatively ordered in contrast to the bulk phase [111, 112, 124], resulting in a closer proximity to nearest neighbors, and thereby resulting in a shift in the primary peak of $g(r)$ with smaller H. We have observed that any local increase in volume-fraction as a result of the formation of layers is minor. Finally, as discussed previously, the number ratio of small to big particles can vary slightly between different regions in the sample. Variations in concentration would result in a variation of the probability of small particles neighboring one another, with a shorter neighbor-to-neighbor distance, thus shifting the first peak of $g(r)$ to the left. Likewise, a decrease in $N_{\text{small}}/N_{\text{large}}$ would render an opposite effect. A similar effect is shown in recent experiments with a bidisperse colloidal suspension like our own [107].

One problem posed in our experiment is the selective visibility of the colloidal particles. As discussed earlier, only the smaller particles of our binary suspension are fluorescently labeled meaning that the larger species of particles are not visible to our confocal microscope. Despite this limitation we can still draw some reasonable conclusions, which has also been suggested by results from a recent simulation on a similarly confined system [121]. For example, in a recent study of the aging of a binary colloidal suspension similar to the one studied here, Lynch et al. showed that the cooperative dynamics of one species were similar to that of the other [45]. In other words, mobile particles of one species were often near mobile particles of the other species. Therefore, our inability to observe the motion of the larger particles does not prevent us from drawing some more general conclusions regarding the role of cooperative behavior in confinement. One other possible limitation is that small rearranging particles may not be nearest neighbors, but may be part of the same CRR, connected by unseen large particles. This is beyond our ability to determine, although it may simply limit the apparent sizes of CRRs without otherwise changing their character.

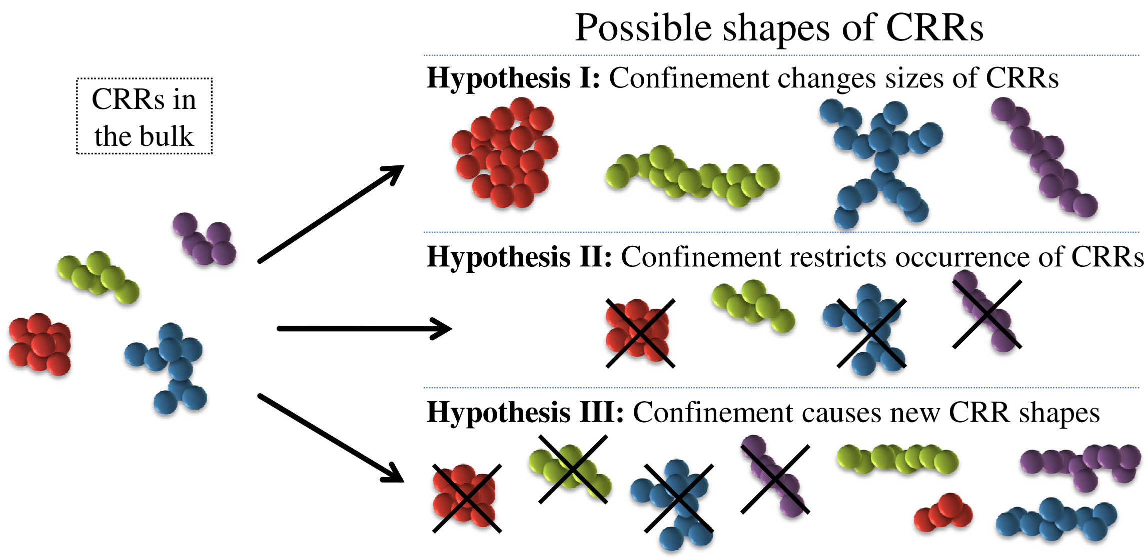

Figure 6.10: Particles in the unconfined bulk sample move via "cooperatively rearranging regions" (CRRs) as indicated schematically at left. Upon confinement, it is possible that the size or shapes of the observed CRRs could change, as indicated schematically at right. Three hypotheses to consider are that confinement might (I) change the size of these regions, (II) only allow some rearrangements to occur, or (III) result in the appearance of entirely new shapes of rearranging regions.

6.4.5 Hypothesized Behavior of Cooperatively Rearranging Regions

We have defined CRRs using the maximum of α_2 to set the time scale for displacements, examining particles with the top 10% of displacements, and using a fixed distance threshold to connect rearranging particles into a cooperative region. We now briefly consider three possible experimental outcomes for how the character of CRRs might change for smaller values of the thickness H.

Hypothesis I: The size of CRRs may change as H decreases. The slowing seen in the MSD curves in Fig. 6.5(a) is similar to that seen in supercooled colloidal liquids, and has been associated with a growing size of CRRs [17, 66]. Perhaps confinement induces a similar larger size of CRRs, explaining the slowing of the MSD (see Fig. 6.10, top). Alternatively, it is possible that due to the smaller available volume, the CRRs are limited in size when confined. In this hypothesis, the CRRs are of the same character as those seen in unconfined supercooled liquids but at a different volume fraction.

Hypothesis II: A second hypothesis is that confining the sample to a smaller volume prevents certain shapes of CRRs from ever forming. Those CRRs which would extend outside the sample chamber are no longer observed. Consider a specific particle: there are many possible CRRs that could move this particle [127]. If a large subset of those are excluded as they would involve non-existent particles outside the sample chamber, then the particle would have to wait until an allowable CRR is attempted before successfully moving. In other words, this hypothesis is that the CRRs seen in confinement are a subset of those seen in the bulk, and that as the subset becomes smaller with smaller H, the overall motion slows (see Fig. 6.10, middle).

Hypothesis III: A third hypothesis is that confinement results in new cluster shapes, that are not observable in the bulk (see Fig. 6.10, bottom). Then, something about the character of these new shapes is connected to the slower dynamics. This hypothesis is plausible due to the layering, which changes the structure in confinement compared to the bulk. Previously, it has been theorized that cluster morphology can relate to dynamics in a predictable way as the glass transition is approached [128].

In the next subsection, we use our experimental data to investigate each of these hypotheses in turn; finding limited support for the first hypothesis, refuting the second hypothesis, and confirming the third hypothesis.

6.4.6 Shapes and Sizes of Cooperatively Rearranging Regions

We begin the assessment of our three hypotheses by rendering three-dimensional images of the CRRs themselves, to develop a qualitative understanding of their nature. Figure 6.12 depicts clusters of the top 10th percentile of the most mobile particles in a sample confined within a plate-spacing of $H = 15.8$ μm and 6.63 μm (panels a/b and c/d, respectively). Only clusters that are $N \geq 2$ in size are shown. For clarity, bonds have been drawn between particles that are nearest neighbors, i.e. within a cluster. The bonds in no way indicate physical attachment between the colloidal particles. The colors of the particles relate to the z component of the particle's displacement, and can be ignored for the moment. For both thicknesses, groups of mobile particles can be seen. Note that the size of these mobile clusters in the unconfined sample is small, as expected for this low volume fraction ($\phi = 0.42$) [17].

We first consider Hypothesis I, that the sizes of cooperatively rearranging regions change upon confinement. At first glance, comparing Fig. 6.12 panels (a) and (c) may suggest that the cluster sizes are smaller upon confinement, but recall that the particles shown are the most mobile 10%; the thinner sample has fewer particles in the imaged volume, and thus 10% of this smaller number results in fewer mobile particles to show without necessarily implying that the CRRs are smaller. To quantify the size of CRRs we calculate the mean number of particles in a CRR N_C as a function of H, plotted in Fig. 6.12(b). Figure 6.12(b) shows that CRRs tend to involve roughly the same number of particles, regardless of thickness. The mean CRR size is between 3 and 4 particles, but this is only slightly larger than the minimum size of 3 particles. The small size may be because the bulk sample, with $\phi = 42$, is liquid-like and only

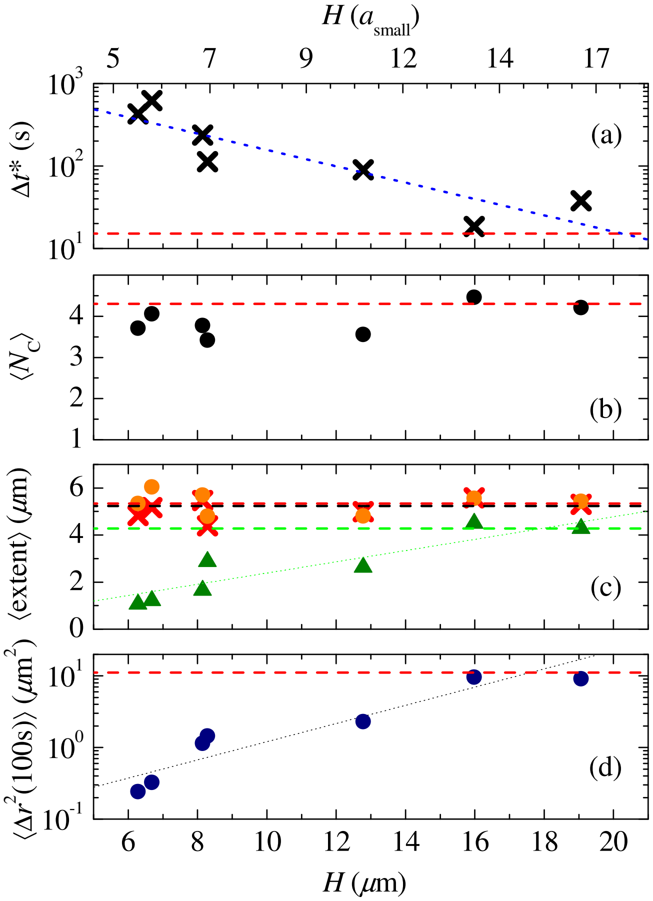

Figure 6.11: (a) Values of Δt^* that maximize α_2 for a range of thicknesses H. The dotted line is a guide to the eye. The horizontal dashed line indicates the value of Δt^* for the bulk sample. (b) Plot of the mean number of particles within cooperatively rearranging regions, as a function of H. Only $N_C \geq 3$ are considered to avoid trivial rearrangements that consist of 1 or 2 particles. The upper dashed line indicates $\langle N_C \rangle$ for the sample's bulk. (c) Plot of the average extent of cooperatively rearranging regions parallel (circles & crosses) and perpendicular (triangles) to the sample's walls. The difference between the x and y data is an indication of the amount of uncertainty in our data. The upper and lower horizontal dashed lines indicate the mean horizontal and perpendicular extent of data from the sample's bulk, respectively. In principle these should be the same (the behavior should be isotropic in the bulk); in practice the lines may differ due to finite data or anisotropy in the imaging volume (50 μm in x and y but only 20 μm in z). (d) Value of the mean square displacement $\langle \Delta r^2 \rangle$ at the time scale Δt=100 seconds. The horizontal dashed line indicates the value of the bulk sample.

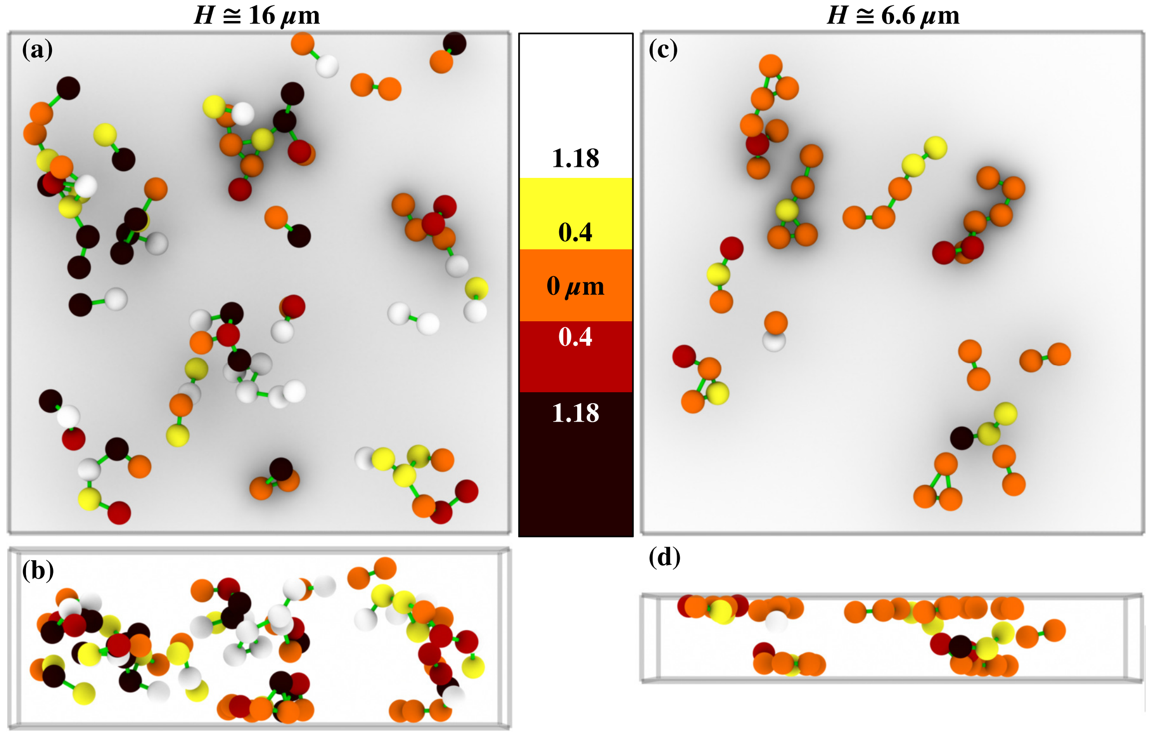

Figure 6.12: Three-dimensional renderings of the top 10^{th} percentile of the most mobile particles in two different sample thicknesses. The green bonds between particles are drawn only to indicate nearest neighbors and do not imply permanent attachment between the particles. Only groups with $N_C \geq 2$ particles are drawn. The colors correspond to the magnitude of displacements in the z-direction, normal to the confining boundaries. The experiment's field of view, and the effective position of the confining boundaries, are indicated by the light gray bounding boxes. The sample on the left (a, b) has a thickness of $H = 15.8$ μm and the one on the right (c, d) has $H = 6.63$ μm. The top row of images (a, c) view the sample normal to the confining boundaries, while the bottom row (b, d) provide a parallel view. Note that black and white indicate displacements of at least a_{small} over a $\Delta t = 23$ s and 250 s for the thicker and thinner sample respectively.

has small CRRs [17]. Alternatively, as noted above, we cannot see the large particles which are almost certainly part of CRRs [45]. With the data of Fig. 6.11(b), we cannot confirm Hypothesis I. There is a very slight downward trend in $\langle N_C \rangle$ with decreasing H, but this could be due to poor statistics. It is possible that the status of Hypothesis I would be clearer in a sample with a larger value of ϕ, although such samples are very difficult to load into our thin sample chambers (as has been noted by others [129]). Likely some of the difficulty in loading the samples is due to their increasing glassiness in confined spaces.

An alternate way to quantify the size of a CRR is through its spatial extent; quantifying this will also provide tests of Hypotheses II and III. We define the spatial extent of the CRRs as $x_{\text{extent}} = \max(x_i) - \min(x_i)$, where i ranges over all particles within a given cluster of mobile particles. Similar definitions apply for the y and z directions. Effectively, the extent is the dimensions of the rectangular box that the CRR fits into, and serves as a crude but useful method of quantifying the size. We plot the mean CRR extent in the x, y and z directions separately in Fig. 6.12(c). We find that the CRRs maintain a constant size in the direction parallel to the walls. However, the amount of distance that the CRRs extend in the direction perpendicular to the walls is significantly smaller than H, and decreases as H decreases. In the z direction, then, Hypothesis I is true, perhaps trivially because CRRs have to fit into a thinner sample chamber. In the x and y direction, Hypothesis I is refuted; clusters do not grow or shrink in this direction. Comparing this result with the $\langle N_c \rangle$ data of Fig. 6.12(b) suggests that the CRRs are becoming more compact in z with the same number of particles. Flatter but similarly sized groups suggests that perhaps the groups are fractal in the bulk, with a fractal dimension larger than 2 (as seen previously in Ref. [17]), and become more planar upon confinement (fractal dimension approaching 2).

We now consider Hypothesis II, that confinement results in a subset of CRRs, drawn from the full set of CRRs that occur in the bulk sample. To test this, we consider the shapes of CRRs, as crudely quantified by the extent measurements. Hypothesis II would suggest that CRRs with a large z extent disappear, and the CRRs with smaller z extents become correspondingly more probable. Within the restricted subset, however, it seems plausible that CRRs should maintain their relative probability. We examine this hypothesis in Fig. 6.13, which shows the probability distributions of the extents in the three directions for a bulk sample (panel a) and a confined sample (panel b). In the unconfined sample the probabilities of the extent in the x, y, and z directions are approximately the same, as should be expected; these CRRs are spatially isotropic. Differences in the z are most likely due to minor particle position errors which are larger in z, as discussed in Sec. 3.3.1. In contrast with Fig. 6.13(a), Fig. 6.13(b) shows that the extents of CRRs in confinement have a very different probability distribution. The extent in z is nearly zero for a majority of CRRs [red curve in Fig. 6.13(b)]; these are planar CRRs and are overwhelmingly more probable than in the unconfined case. A small subset of confined CRRs do extend into the z-direction by one to two particle diameters. The relative probabilities of planar CRRs as compared with non-planar CRRs for Fig. 6.13(b) are very different than in the unconfined case, demonstrating that Hypothesis II is false.

However, Fig. 6.13 shows that Hypothesis III is true: the CRRs in the confined cases are qualitatively new and different than those of the unconfined sample. The CRRs often consist of particles from only one layer, and thus are planar. Given that the bulk sample does not have layers (at least, away from any walls), it makes sense that these planar clusters are not found in the bulk. Some CRRs do have particles from more than one layer, although the shapes still differ from the unconfined case. The clusters of rearranging particles along the walls in Fig. 6.12(c, d) seem to be the most planar in shape, which is in agreement with the findings of Ref. [124], where the behavior of particles along the walls are uniquely quasi-2D. We have also tested our conclusions by considering the radius of gyration in x, y, and z for the clusters; the results are similar to those in Fig. 6.13.

6.4.7 Dynamics Within Cooperatively Rearranging Regions

We can investigate the behavior of particles within CRRs. In Fig. 6.12 the color intensity of the particles corresponds to the magnitude of displacements in the $+z$ and $-z$ directions, respectively; white is positive and black is negative. If a particle is moving predominantly in a horizontal direction then it is colored orange. Solid black or white correspond to displacements of at least a full particle radius over the indicated Δt. As suggested by the greater number of white beads in Fig. 6.12(c, d), in the confined situation mobile particles displace horizontally more frequently than otherwise. This makes sense; a rearrangement consisting of particles within a single layer does not require the particles to move vertically for the rearrangement to occur. Occasionally we do see particles which jump between layers or even swap between layers; one example is near the bottom right corner of Fig. 6.12(c).

The onset of flatter or more planar CRRs coincides with the sample's overall slowing. In Fig. 6.11(d) we plot the MSD values from Fig. 6.5(a) for $\Delta t = 100$ s against the corresponding range of H. We observe that the MSD values of Fig. 6.11(d) begin to deviate from those of the bulk, indicated by the horizontal dashed line in (d), at approximately the same H that the z-extent of the CRRs first begin to flatten relative to the z-extent from the bulk, the horizontal dashed line in (c). In order for CRRs to be planar, the likelihood for individual cage rearrangements in the z-direction must be restricted. The inhibition of particle motion in z means that particles simply take a greater amount of time to move out of the way of their neighbors in any direction, z or otherwise. Thus, the system's average rearrangement timescale exhibits an overall increase. What results is the observed correspondence between the sample's average mobility and the likelihood for adjacent particles to isotropically rearrange.

To compare the amount of displacements that are parallel to the boundaries to those that are perpendicular, we calculate the directions of motion for all particles and

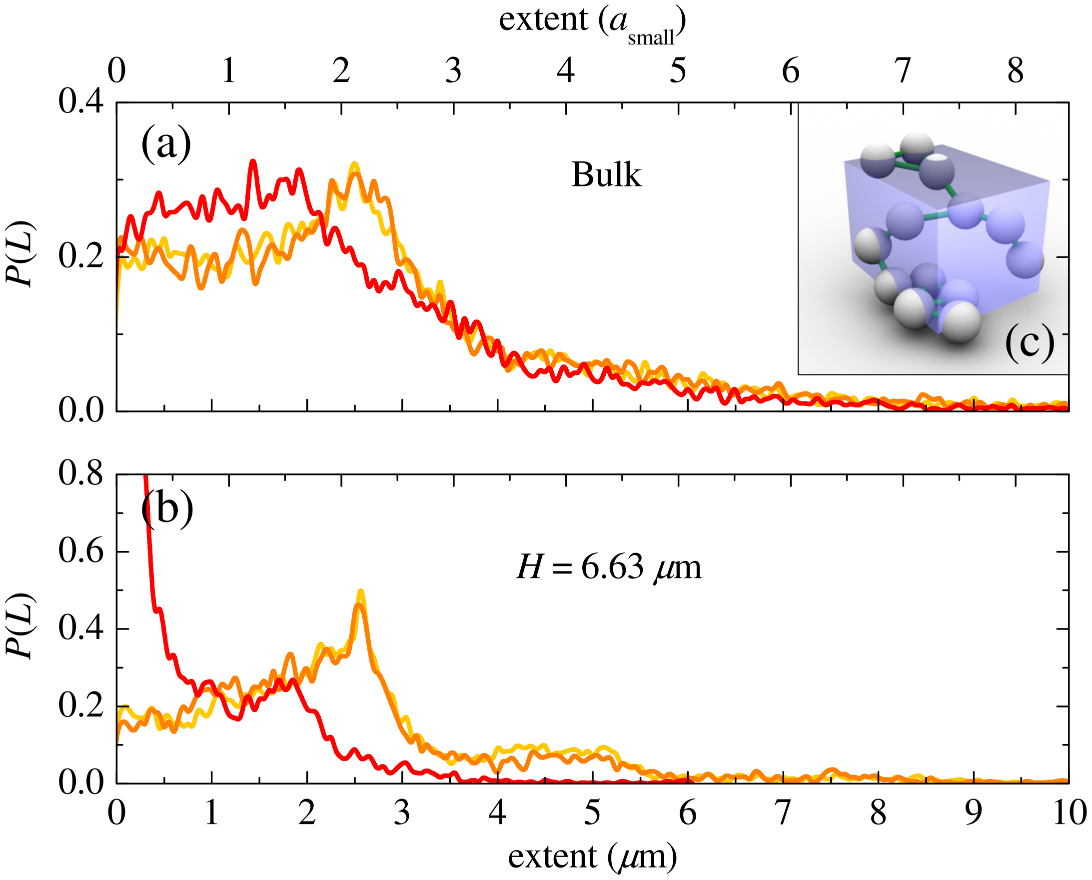

Figure 6.13: Extent of mobile groups of particles. Red and two orange lines indicate the components of CRR extent that are perpendicular and parallel to the boundaries, respectively. CRRs in the bulk (a) of the sample are more isotropic in shape than when confined (b) to $H = 6.63$ μm. Note the difference in scales used by the two plots. Only CRRs consisting of at least 3 particles are considered in the data shown. (c) A rendering depicting how extent is calculated, where a box (in shaded blue) is fitted through the centers of the outer most particles in a cluster.

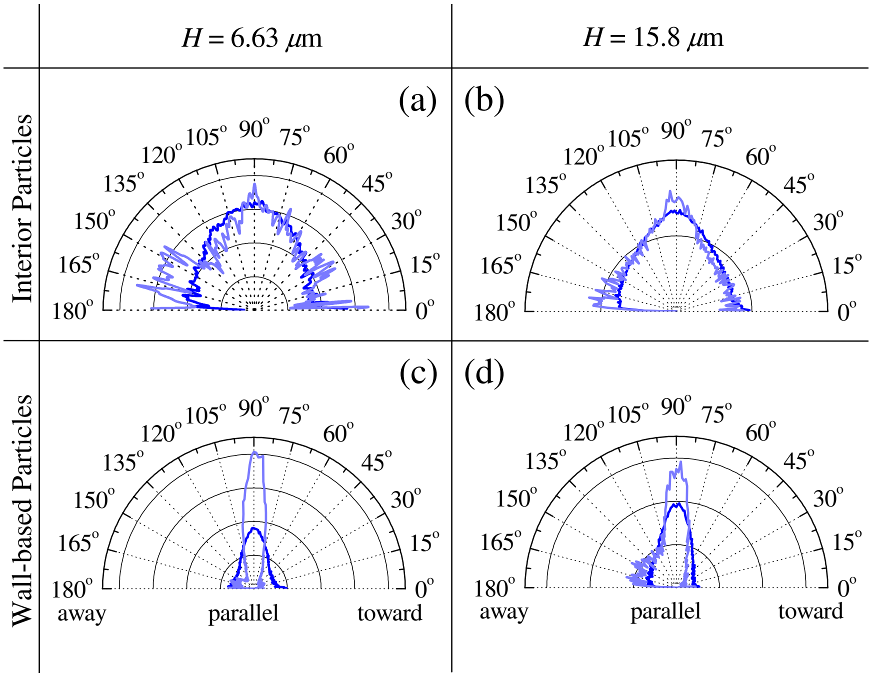

Figure 6.14: Polar plots of the probability distributions of the directions of particle displacements for $H = 6.63$ and $H = 15.8$ μm as indicated. (a,b) Data for the two thicknesses, considering only particles away from the walls. (c,d) Data for particles in the layers immediately adjacent to a wall. The displacements from one wall are reversed, so that 180° always means motion away from the nearest wall. In all panels, the light blue curve is the distribution for the most mobile 10% of the particles, while the dark blue curve is the distribution for all particles. Displacements are measured over $\Delta t = 250$ s and $\Delta t = 23$ s for the $H = 6.63$ μm and $H = 15.8$ μm data, respectively.

then repeat the comparison for different confinement thicknesses. Using a spherical coordinate system we determine the polar angle of a given particle displacement. The polar angle θ spans a range from 0° to 180°, which correspond to motion toward or away from the nearest sample chamber wall, respectively. That is to say that we exploit the symmetry between the two walls. We first compute the polar angle θ relative to the $+z$ axis, and then use $180° - \theta$ for the data in the lower half of the sample chamber. Comparing the data separately for the top and bottom half, we find no difference in the results. For isotropic motion, the distribution of θ is proportional to $\sin\theta$, so we divide our measured histograms by $\sin\theta$ to remove this dependence. The distributions are plotted in polar coordinates, shown in Fig. 6.14, for thicknesses of $H = 6.63$ μm and $H = 15.8$ μm. The blue curves are for all particles, and the light blue curves are for the top 10^{th} percentile of displacements, providing insight into the directions that tend to permit higher mobility. The top panels show the motion of the particles in the interior of the sample, and the bottom panels show the motion of the particles immediately adjacent to the walls.

In both the 15.8 μm and 6.63 μm samples, the particles in the outer layers along the walls tend to move parallel to them rather than perpendicularly [Fig. 6.14(c, d)]. Predominantly parallel motion along the walls makes sense in light of our assertion that the walls induce quasi-2D layering [111]. The effect is even more pronounced for the fastest particles, whose distribution suggests that fast particles are moving almost exclusively along the walls. This agrees with our observations from Fig. 6.12(b, d), where all but one of the particles layered along the walls are almost all orange, indicating they are moving primarily horizontally. The distributions in Fig. 6.14(c, d) do show some data at $\theta = 180°$, indicating that some particles move away from the walls, and less data at $\theta = 0°$, indicating that some particles make slight motions toward the walls. As noted in the discussion of Fig. 6.3, there is a slight Coulombic repulsion between the particles and walls, so particles within the layer adjacent to a wall have some ability to move toward the wall.

The situation changes markedly for the inner layers [Fig. 6.14(a, b)]. Considering only the full distribution of all particles we see that particles tend to move in any direction, so their dynamics are isotropic. The distribution of directions for the fastest interior particles is not significantly anisotropic, but they do show a tendency to move perpendicular to the confining boundaries. There are bumps in the distribution near $\theta = 0°$ and 180°, which suggests that particles that move in z have a slight increased probability to make large motions in z, hopping between layers. Figure 6.12(b, d) show that rearrangements of particles along the walls and the ones within adjacent density layers can be coupled via the occasional large perpendicular displacements of individual particles, a tendency confirmed by examining movies of particle motion.

Overall, the particle dynamics in the thicker region are far more isotropic than the ones from the confined region [compare Fig. 6.14(a, c) with (b, d)]. In the $H = 15.8$ μm case, the fastest particles' dynamics are almost as isotropic as the rest of the sample. Only along the walls, where the fastest particles tend to move in a planar manner, is there any appreciable sign of anisotropic behavior. For thicker samples, where $H \geq 15.8$ μm, heterogeneous dynamics only exist along the walls. Throughout the rest of the interior, the sample's dynamics are liquid-like, as suggested in Fig. 6.5(a).

6.4.8 Conclusion

We find that confinement slows the motion of colloidal particles and thus induces a glass transition to occur sooner than normal, in other words, at volume fractions for which the bulk behavior is liquid-like. The smooth quasi-parallel walls confining our sample induce the formation of density layers within the colloidal sample's volume. The higher particle density within the layers increases the duration of cooperative rearrangements, giving rise to heterogeneous dynamics, typically the hallmark of glassy systems, despite our sample's relatively low volume fraction. The structural inhomogeneities induced by the density layers result in corresponding inhomogeneities in the system's dynamics, as described by the plots in Fig. 6.7. The most dense layers form along the sample chamber's glass surfaces, as shown in Fig. 6.4 and also observed in recent experiments in simulations [49, 110, 112]. The "quasi-two-dimensional behavior" [124] of the wall-based particles mean that they tend to remain there. The layered particles do cooperatively rearrange within the layer but rarely with adjacent layers. The wall-based layers serve as templates, inducing the formation of additional layers further from the walls, depicted in Fig. 6.4.

The volume fraction in the bulk region of Sample A is too low for the particles to rearrange in groups, using the methods of [17] to look for such groups. Any length scale for such groups appears to be at most ∼2 particle diameters. It is intriguing that we observe the confinement effects to begin at a thickness H of approximately 7 small particle diameter. Previously, the largest dynamic length-scale observed in a comparable colloidal system was approximately 3 particle diameters; each particle is 2.36 μm in diameter, resulting in a length-scale totaling ∼9 μm [17, 103]. These values are even larger than those observed in simulation (0.05-0.32 in Lennard-Jones units) [130]. The confinement length scale observed in the work presented here, see Figs. 6.6 and 6.11, is the largest length scale ever observed in a colloidal model glass former. Experiments with molecular glass formers observe confinement being effective over length scales significantly larger than those of cooperatively rearranging regions (CRRs) [85, 131]. In the same way, as shown in Fig. 6.11, we observe that the CRRs present in our confined colloidal system are roughly 3 times smaller than the confinement length-scale.

The rarity of rearrangements perpendicular to the confining walls can explain the minimal upturn in the z-component of the MSD curves in Fig. 6.5(c). Like the particle number density, the particle dynamics vary with distance from the walls, as depicted in Fig. 6.7(c). For example, the dynamics of particles near the volume's center are naturally less 2D than the ones closer to the walls. The correspondence between particle mobility and number density is an intuitive one: the layers' higher particle density causes an increase in cooperative rearrangements among the layered particles. The layer-bound cooperative rearrangements are the source of the heterogeneous behavior observed in the sample's averaged dynamics, as indicated by the MSD curves in Fig. 6.5(a). As the thickness H decreases, perpendicular displacements between layers become more difficult. The infrequency of particle displacements between layers results in a hindrance of rearrangements within layers, resulting in an overall slowing of motion. The slowness or increase in the rearrangement time scale is indicated by Fig. 6.11(a).

Simulations [49, 87, 132] and a recent experiment [20, 101] suggest the roughness of the walls is crucial to this slowing. However, we note that our data show slowing both with completely smooth walls (samples B, C, and D) and walls with isolated stuck particles (sample A). In contrast to our work, rough walls in simulations and an experiment are composed of particles fixed in a liquid-like structure [49, 87, 97, 101]. This prevents layering of adjacent particles and restricts motion parallel to the walls. Thus the glass transition in confined samples occurs sooner (at higher temperatures [87, 97] or lower densities [49]). In our experiments, particle motion parallel to the wall is not noticeably inhibited, as seen in Figs. 6.7 and 6.8. Yet, we still find the glassy behavior occurs sooner: at constant volume fraction, the dynamics are slower as the confining dimension decreases. Thus it seems that the important effect in our experiments is simply the restriction of motion perpendicular to the wall, close to the surface of the wall.

With displacements tending to occur within layers, cooperatively rearranging regions exhibit an increasingly planar shape, as seen in Fig. 6.11(c). In conclusion, the thickness at which we begin to observe the slowing in the sample's average dynamics corresponds with the confinement length-scale at which cooperatively rearranging regions begin to become planar in shape [Figs. 6.11(c) and (d)]. The trend of the data in Fig. 6.6 suggests that the observed increase in rearrangement time-scales and the thickness at which these regions begin to flatten will both grow with higher volume-fractions [19]. It will be important to see how these results will change when the walls have texture which frustrates the formation of layers, a case which has been carefully studied in simulations [49, 97, 100]. Recent colloidal experiments show that the MSD is larger near rough walls than for smooth walls in the same sample [101].

A quick means of investigating the role of boundary roughness in confined systems, using our colloidal data from Sample A, is to examine the motion of particles in comparison to their distance from stuck particles.

6.5 Influence of boundary roughness

As discussed above, varying portions of the boundaries of Sample A are dotted with stuck particles. It is the influence of these stuck particles that we investigate in

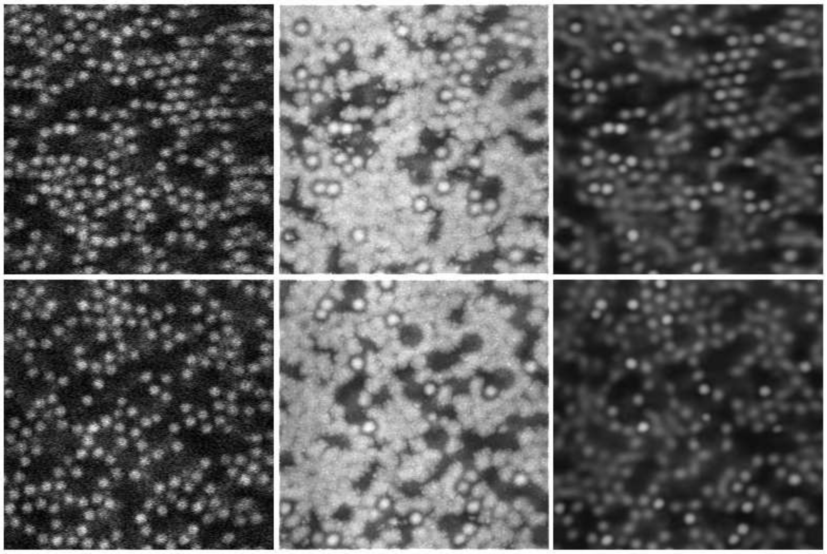

Figure 6.15: Images showing behavior near the top wall ($z = H$, top row of images) and near the bottom wall ($z = 0$, bottom row of images). The left images are individual 2D slices from a single 3D image stack. The middle images show the maximum intensity observed at each location over the duration of the movie (2300 s in duration). The right images show the average intensity observed at each location over the duration of the movie. Bright spots in the middle and right images indicate visible particles stuck to the glass, and darker regions suggest where the larger invisible particles are stuck. Regions that are black in the left panels but not in the middle panels are probably occupied by mobile large particles. For this region of the sample chamber, $H = 8.06$ μm.

this section. These particles are visible in Fig. 6.15. The top row shows images corresponding to the top of the slide, and the bottom row shows images from the bottom of the slide in the same x and y location. The left images are 2D raw images taken from the confocal movie. The middle panels are the maximum intensity observed at each pixel over the duration of the movie. In these images, stuck small particles show up as distinct white circles, and stuck large particles show up as black regions. The remaining space is filled in fairly uniformly by the visible small particles exploring the available free space. The right panels of Fig. 6.15 show the time-averaged intensity of each pixel. Here the brightest white circles are the stuck particles, and the less bright spots are where mobile particles spent longer periods of time. The darker regions correspond to locations where no visible particles wandered during our observation period, and thus are likely to have invisible particles stuck in those locations.

The images of Fig. 6.15 show that the stuck particles are easy to distinguish in the data, as they do not move. We also note that their positions are closer to the wall than the other particles, both giving us evidence for the repulsion of the mobile particles from the walls, and also allowing us to accurately determine the local thickness H based on the stuck particle positions [21]. The area fraction of the stuck particles ranges from 10% to 20% (total for both species). From DIC microscopy as well as images such as those shown in Fig. 6.15, we find that the large particles appear to be stuck in comparable area densities to the small particles. It is interesting to also note that there are large patches next to the walls which do not have any stuck particles. This can be seen in the connected regions that are uniformly bright in the middle images of Fig. 6.15. While the avoided regions make it clear where the stuck particles are located, the regions fully explored by the mobile particles given a sense of where the particles see only the flat glass wall.

From the z positions of the stuck particles, we can determine the sample thickness H. This is the maximum range that the particle *centers* can cover, whereas the actual wall spacing is $H + 2a_S$. As we can determine H more precisely than we know a_S, we report our results in terms of H. The uncertainty in measurements of H is ± 0.01 μm and $2a_S = 2.36 \pm 0.04$ μm [19]. Our uncertainty of H is low, much smaller than our resolution (0.1 μm in z), because we average over all of the particles stuck on each surface to find the surface's location in z. While individual particles' z-positions vary because of noise, the average is well defined in all cases.

6.5.1 Results

As noted earlier in this Chapter, Fig. 6.5(a) for example, confinement results in slower particle motion [19, 21]. This is illustrated in Fig. 6.16, which shows the mean distance particles move $\langle \Delta x^2 \rangle$ (circles) and $\langle \Delta z^2 \rangle$ (triangles) within a given time Δt, as a function of the thickness H. For $H > 16$ μm, there is no dependence on H, suggesting that $H \approx 16$ μm is the onset length scale for the confinement effects for this sample. For smaller H, the motion slows down dramatically. This suggests that confinement induces the colloidal glass transition to occur "earlier," that is, at a lower volume fraction ϕ than would be seen in the bulk. The results do not vary qualitatively with the time scale Δt; in the results below, we use $\Delta t = 100$ s as a representative time scale. As shown in Fig. 6.6, the onset length scale grows with increasing volume fraction as $\phi \to \phi_g$ [19]. In this section we focus on Sample A, described in Tables 6.3 and 6.2. This sample is a liquid when unconfined, and while it slows down upon confinement, the sample never enters the glassy state for any confinement we have studied.

Simulations found both faster and slower dynamics within confined samples, depending on the texture of the confining boundary. For cases with smooth walls, particle motion is faster, and for cases with rough walls, particle motion is slower [49, 132]. To simulate rough walls, typically one simulates a bulk liquid, and then locks the positions of some of the particles into place to become the walls, as shown in Fig. 6.17(a). Near the walls, this roughness sterically frustrates particle motion parallel to the walls, and thus intuitively it is sensible that these boundary conditions

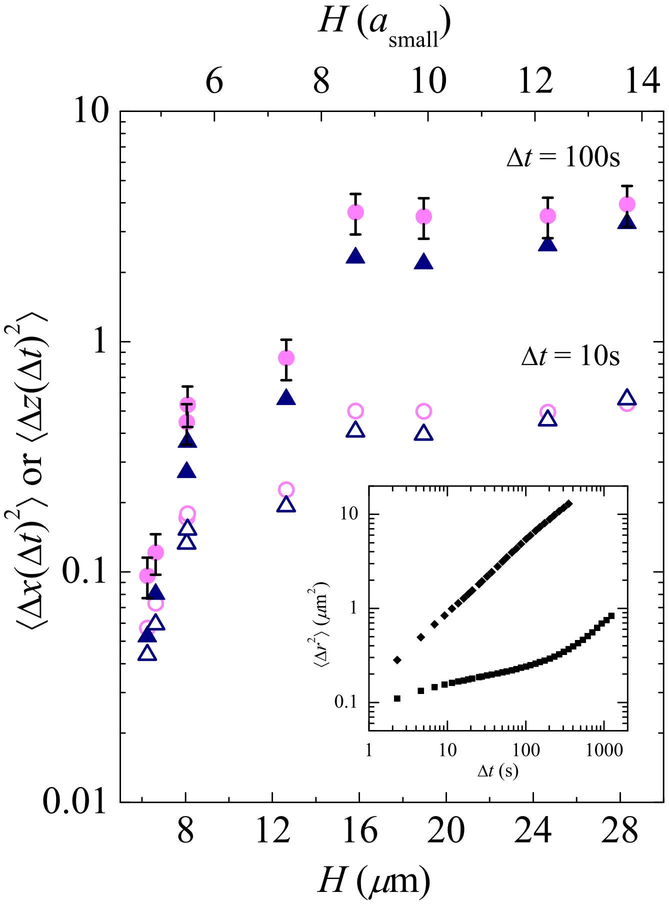

Figure 6.16: The average mobility $\langle \Delta x^2 \rangle$ (parallel to the sample chamber walls, indicated by circles) and $\langle \Delta z^2 \rangle$ (perpendicular to the sample chamber walls, indicated by triangles), as a function of the confinement thickness H. The open symbols are for $\Delta t = 10$ s and the solid symbols are for $\Delta t = 100$ s. There is an additional data set at $H = 69$ μm not shown which agrees with the data shown for $H > 16$ μm [19]. The uncertainties of the data points are ±20%, and are indicated by representative error bars for one set of data. The inset shows the mean square displacement for samples with $H = 16.32$ μm (upper curve) and $H = 6.25$ μm (lower curve). The data shown here is from Sample A.

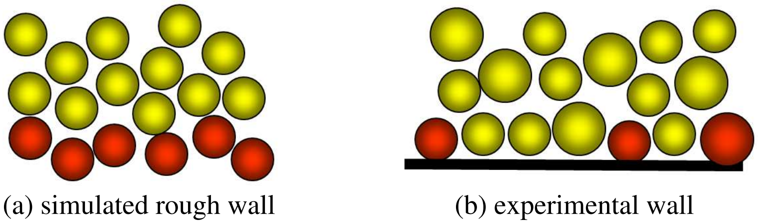
(a) simulated rough wall (b) experimental wall

Figure 6.17: Sketch of typical boundary conditions. (a) Rough walls in a simulation; the dark (red) particles are taken from a liquid configuration and then immobilized. (b) Our boundaries with a few dark (red) particles stuck to the walls.

result in glassier dynamics. It has also been noted that for smooth walls, particles tend to form layers near the walls [112, 132, 133]. Particles which move within layers then could potentially move more easily [49]. In one set of simulations, an extra spatially varying potential was added to either enhance or prevent particle layering [100]. They found that particles are indeed more mobile when organized into layers. An implication then is that in addition to the steric frustration of motion, rough layers such as shown in Fig. 6.17(a) prevent particles from layering on the walls, and this will additionally slow the dynamics.

Our boundary conditions, schematically shown in Fig. 6.17(b), present two conflicting possibilities. Mobile particles are hindered in their motion when they encounter stuck particles. This should lead to glassier behavior when the samples are confined (implying that more particles are close to the wall, where they feel the influence of the stuck particles). On the other hand, the flat patches allow particles to form layers against the wall. Furthermore, the stuck particles are the same size as these layers, and so also help formation of additional layers farther from the wall. Indeed, we do see layering of the visible (small) particles, as discussed in Ref. [19, 21] (cf. dotted lines in Fig. 6.7). Simulations suggest that the larger invisible particles also form layers against the walls, although because of the binary mixture, the layers of both particle sizes quickly wash out away from the walls [112]. Our prior work found that particles prefer to move within these layers [21], suggesting the possibility of enhanced mobility, based on comparison with the simulations. The one mitigating factor is that particles within the layers next to the walls are a mixture of the two particle sizes, and so the layers are more "entangled" than they would be if all of the particles were identical in size [49, 112]. Recall that Samples B–D, see Table 6.3, have completely smooth walls with no stuck particles, and confinement still resulted in slower motion (see Fig. 6.6) [19]. This demonstrates that the stuck particles are not solely responsible for confinement induced slowing in our samples, although perhaps they slow motion even further.

To clarify the role of the stuck particles, we examine how the motion of the mobile particles depends on their distance to the nearest stuck particle. It is important to note that we only know the distance to the nearest *visible* stuck particle, so some particles will appear far from any stuck particle and yet be neighboring an invisible stuck particle. The unlabeled particles do appear as black regions, but their centers cannot be accurately defined. With this caveat in mind, we plot the mean squared displacement $\langle \Delta r^2 \rangle$ as a function of distance s from the nearest visible stuck particle in Fig. 6.18(a) (using $\Delta t = 100$ s). (s is defined based on the initial position of the mobile particle at t, rather than the final position at $t + \Delta t$.) Near a stuck particle, $\langle \Delta r^2 \rangle$ decreases by about 10 - 20 percent. The size of the decrease appears about the same for all samples. However, thicker samples show a longer-ranged influence of the stuck particles; we are not sure why. For the $H = 15.8$ μm data, the stuck particle influence is seen even out to $s \approx 6$ μm, nearly three small particle diameters. Slight upturns are seen at the smallest values of s that we plot, around $s = 2.36$ $\mu\text{m} = 2a_S$. These are due to tracking errors (particles which appear incorrectly closer to a stuck particle than their diameter), which causes a larger subsequent displacement when the tracking error is corrected. For all curves in Fig. 6.18(a), the data at large values of s typically correspond to particles near the edge of our imaging volume, where no visible stuck particles happen to be nearby within the imaging volume. Because of the high likelihood of being adjacent to stuck particles outside the imaging volume (given the fairly uniform coverage of the stuck particles on long length scales), we crop the data for $s < 0.8H$ where we think the data are potentially misleading. In all cases, the cropped data are essentially flat, that is, independent of s and continuing the trend shown in Fig. 6.18(a).

We note that the magnitude of the effect seen is not large, on the scale of the dramatic slowing down shown in Fig. 6.16. That is, the slowing due to varying the sample thickness H appears to be the primary effect, and the influence of the texture is a secondary effect. For example, changing H from 12.6 μm to 8.06 μm in Fig. 6.18(a) changes the overall dynamics by a factor of more than 2, as indicated by the horizontal dotted lines, while the proximity to stuck particles results in a decrease by a factor of only 1.2 for each H. The variation between the amount of stuck particles on walls ranges from 10% to 20% of the area, which our current results suggest is not enough of a variation to change the overall character of the slowed dynamics as a function of H (in other words, the data shown in Fig. 6.16).

Despite the weakness of the effect, these results suggest that different boundary conditions will slightly influence the overall dynamics. For example, if there were more stuck particles on one side of the sample chamber than on the other, we might expect a gradient in mobility. Such asymmetric boundary conditions are present in a few of our experiments, such as the example shown in Fig. 6.19. Here, the top of the sample chamber has more stuck particles than the bottom. This is most clearly seen by contrasting the top-middle image (from the top of the sample chamber) with the bottom-middle image. To examine the impact on the mobility of particles, we plot the average mean square motion $\langle \Delta x^2 \rangle$ as a function of z in Fig. 6.20(a). Here, the dotted black line indicates the number density as a function of z, showing the layers

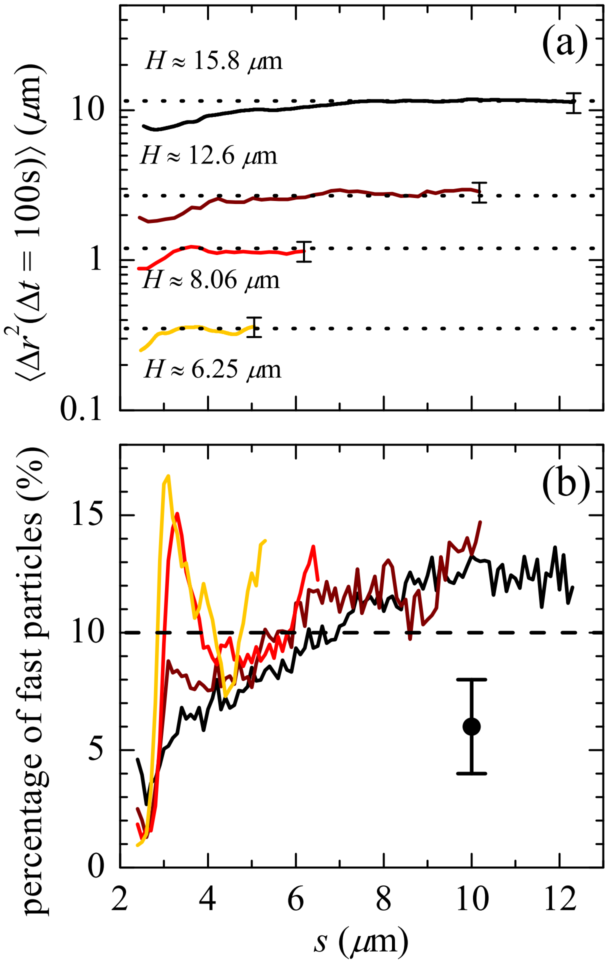

Figure 6.18: (a) Graph of the mean square displacement $\langle \Delta r^2 \rangle$ as a function of the distance s away from the nearest immobile boundary particle. The displacements are calculated using a time lag $\Delta t = 100$ s, and the curves are from different sample chamber thicknesses H as indicated. The horizontal dotted lines indicate the plateau height for each curve, averaged over all particles at all s. The plateau height decreases for smaller H, indicating the average slowing due to confinement. Error bars for each curve are indicated at the right end of each curve. (b) Graph of the fraction of highly mobile particles, as a function of distance s from the nearest immobile boundary particle. The definition of "highly mobile" is such that 10% of the particles are considered highly mobile, so on average the data should fluctuate around 10% on this graph (indicated by the horizontal dashed line). The color/shading of each curve is the same as for panel (a). The error bar shown indicates the uncertainty of the data. In both panels (a) and (b), the curves are truncated at large s, where there are too few particles to provide adequate statistics.

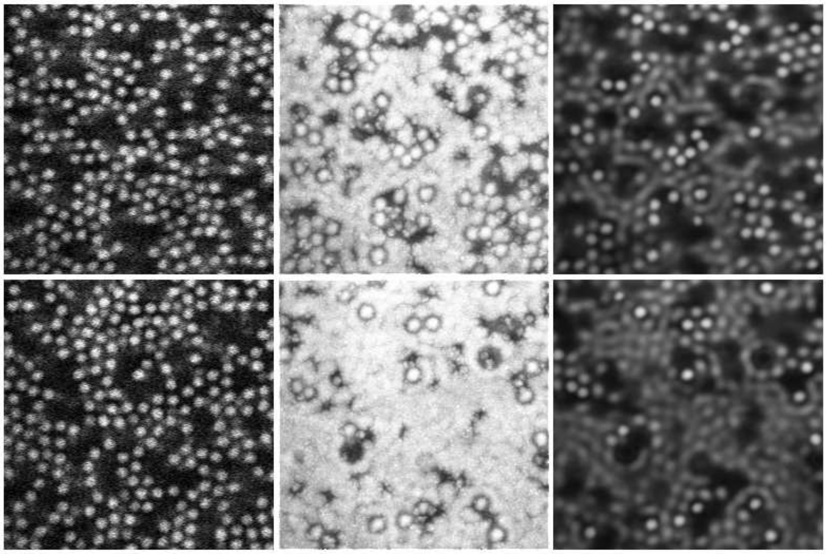

Figure 6.19: Images similar to those described in Fig. 6.15. Here, the top of the slide (top row of images) has more stuck particles than the bottom of the slide (bottom row of images). In particular, the bottom-middle image shows a large region where mobile particles have wandered freely, whereas the top-middle image shows much smaller free patches of open surface. For this region of the sample chamber, $H = 8.09$ μm. The duration of this movie was 2500 s.

of particles, and the thicker shaded curves show the mobility $\langle \Delta x^2 \rangle$ for different lag times Δt as indicated. Especially for the longest lag time $\Delta t = 100$ s, particles are more mobile closer to $z = 0$, where there are fewer stuck particles at the glass wall. Figure 6.20(b) shows the more common case that we observe, corresponding to the more symmetric boundary conditions of Fig. 6.15, and where there is little variation in mobility across the sample.

One last question is how the stuck particles influence the spatial dynamical heterogeneity. Prior work has shown that in glassy materials, motion occurs intermittently in time and in spatially localized regions at any given moment [10, 11, 14, 68]. For example, microscopy studies of dense colloidal suspensions found cooperative motion, where groups of particles would all rearrange simultaneously [17, 45, 66, 69, 73, 134]. Our results above show that proximity to stuck particles at the boundary decreases the average mobility of particles; this suggests that the most mobile particles undergoing cooperative rearrangements are less likely to be near the stuck particles.

To check this, we define a highly mobile particle as one with a displacement in the top 10 percentile of the displacement distribution [21]. If the sample behaves homogeneously, we expect that in any given region, roughly 10% of the particles we observe there over time should be highly mobile. We first define displacements using

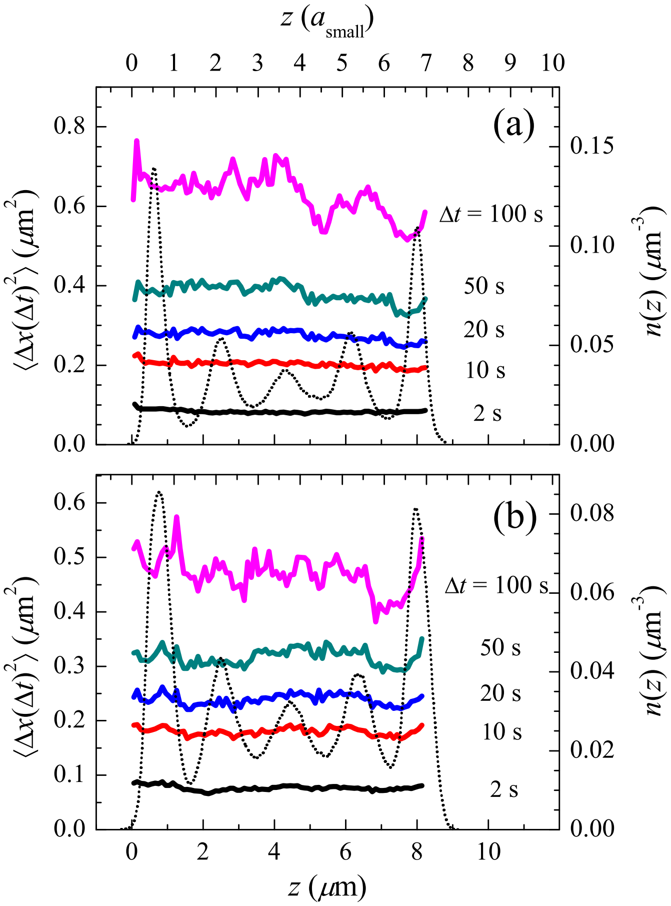

Figure 6.20: In both panels, the thin solid black curve shows the local number density $n(z)$ for the mobile particles (right vertical axis). The family of thicker shaded curves show the average mobility as a function of z, for the values of Δt indicated. For (a), the data correspond to Fig. 6.19 with $H = 8.09$ μm. For (b), the data correspond to Fig. 6.15 with $H = 8.06$ μm. The noise in the $\langle \Delta x^2 \rangle$ data give a good representation of the uncertainty, ±10% in all cases.

the methods of Refs. [17, 68]: $\delta r(t, \Delta t) = \max|\vec{r}(t_i) - \vec{r}(t_j)|$, with $t \leq t_i < t_j \leq t + \Delta t$; by allowing the time interval to fluctuate, this removes some of the "noise" of the Brownian motion and highlights the truly large motions. We determine the threshold δr^* such that 10% of the displacements are larger than this threshold. We then examine, as a function of s, what fraction of particles at that distance have displacements larger than the threshold. The results are plotted in Fig. 6.18(b), which would be a flat line at 10% if there was no influence of the stuck particles (indicated by the horizontal dashed line). Instead, we see that the highly mobile particles are less likely to be adjacent to stuck particles. Clearly, the stuck particles have a strong influence on the spatially heterogeneous dynamics. While the two thinnest data sets ($H = 6.25$ μm and $H = 8.06$ μm, darkest curves) show a spike around $s = 3$ μm, it is most likely noise due to lack of statistics, whereas the dip close to contact ($s \approx 2a_S = 2.36$ μm) is systematic for all data. We estimate the uncertainties due to noise in Fig. 6.18(b) are ±2%, judging from the large s data. The deviations for $s < 4$ μm appear significant, especially the dip close to contact.

6.5.2 Conclusion

In this section we have discussed our study of the influence of confinement on a dense colloidal suspension, which is a good model system for a small-molecule glass-former. Confinement between two rigid glass walls results in slower particle motion [19]. In this article, we examined how particles stuck on the walls influence the dynamics of nearby particles. Not surprisingly, proximity to a stuck particle results in reduced mobility. In cases where one wall has more stuck particles than the opposite wall, a slight gradient in mobility is seen, with the slowest motion next to the roughest wall. These results are in qualitative agreement with simulations, although the roughness in simulations is of a different character than our experiment [49, 97].

One caveat is that in our experiments, only the small particles are fluorescently dyed and so we do not see the large particles. There are both mobile large particles whose motion is unknown, and also large particles stuck against the wall whose influence is unseen. Presumably these latter particles diminish particle mobility nearby. Currently, we see a reduction in average particle motion of about 20% near stuck visible particles. Likely if we could measure the distance to the nearest particle of either size, the observed reduction in average particle motion near immobile particles would become more pronounced. However, it is possible that due to the layering, proximity to immobile large particles would not slow down the mobile small particles. Prior experimental studies of binary particle mixtures do not see a strong overall difference in mobility of the small and large particle species [45], and our qualitative observations of confined samples using DIC microscopy likewise did not see large differences.

Our work shows that local variations in wall texture influence the motion of nearby particles, and this in turn suggests that it is possible to locally tune particle mobility by tuning wall texture. While this observation is unsurprising, this has implications for microfluidic flow of colloidal suspensions. First, the effective viscosity of a colloidal suspension is likely higher in a small capillary tube, given our observed glassiness in the particle motion. However, the viscosity and diffusivity may depend differently on the confinement length scale [80]. Second, if particles stick to the capillary tube walls, then over time the mobility will decrease especially strongly near the stuck particles.

I spent a significant amount of time assisting an undergraduate who attempted to conduct experiments to study more complex and controlled wall textures to see their influence on the glassiness of confined of colloidal suspensions. Walls were textured or roughened with particles by spin-coating a colloidal suspension in a layer across the surface, and then sintering the particles. The work yielded little to no meaningful results. Hopefully this work will be pursued in the future.

A similar series of experiments, also patterning the glass confining boundary through the sintering of particle layers, were recently reported on by Sarangapani, *et al.* [135]. Their findings are similar to our own, providing little further insight. Another series of experiments, where a colloidal suspension is carefully confined between a smooth and rough surface, show that rougher walls do slow dynamics, but not as dramatically as smooth walls [101].

This work was supported by a grant from the National Science Foundation (DMR-0804174). We thank A. Schofield and W. C. K. Poon for providing our colloidal particles.

Chapter 7

Rotational Diffusion

7.1 Introduction

We use confocal microscopy to observe the rotational and translational dynamics of ordered clusters of colloidal particles in a colloidal "supercooled fluid". In a Newtonian fluid, the rotational diffusion constant D_{R} and translational diffusion constant D_{T} depend on the temperature T and viscosity η in a simple fashion. In particular, for a given tracer size and shape, the ratio $D_{\mathrm{T}}/D_{\mathrm{R}}$ is a constant independent of T and η [59]. However, in supercooled molecular liquids close to the glass transition, this seems to not be the case [10, 11, 18, 136–140] This suggests that supercooled molecular liquids are not merely Newtonian fluids with large viscosities, but that diffusion takes place by fundamentally changed mechanisms [3–5, 139, 140].

We directly observe rotational and translational diffusion of non-spherical particles embedded in dense colloidal suspensions. As described extensively in Chapter 2, colloidal systems manifest a glass transition as the volume fraction of the solid particles approaches $\approx 58\%$ [8, 24]. Because they can be viewed directly, colloids are ideal for studying the mechanisms of this transition [17, 66, 91]. As discussed in Chapter 3, we use confocal microscopy to observe the motion of the colloidal clusters of particles [25, 26]. Thus, we can measure D_{R} and D_{T}, and make an effort to determine the microscopic mechanisms responsible for their changes near the glass transition.

A focus of this work is to look for possible spatial heterogeneity in the rotational motion [141–144], which may be analogous to previously identified translational heterogeneities [10–12, 68, 94] and which may explain the behavior of $D_{\mathrm{T}}/D_{\mathrm{R}}$ [59, 60, 139]. A decoupling might manifest itself by a difference between translational heterogeneities and rotational heterogeneities, for example in size, shape, or mobility.

The work presented here is the first in what will become a significant series of experiments that constitute a timely intersection of three components: a novel synthesis method for non-spherical clusters of colloidal particles developed from 2003 onward [22, 32, 145], microscopy techniques for studying the colloidal glass transition developed by our group from 2001 onward [19, 25, 26, 45, 74, 146], and simulations from 2004 onward studying rotational motion in supercooled fluids [59–61, 141]. In the same vein, the issues to be settled by our ongoing experiments have been recognized since the 1990's [18, 136–140]. Our experiments are the first direct experimental observation of rotational motion in a supercooled fluid.

7.2 Background

A general discussion regarding the background of the glass transition can be found in Chapter 1, but I will reiterate some of its key points here to provide context for our experiments with rotational diffusion.

Rapid cooling of some materials results in the formation of an amorphous solid known as a glass. This transition to a disordered solid is the glass transition [3–5]. As the temperature of a molecular glass-forming material is decreased the viscosity rises smoothly, but rapidly, with little apparent change in the microscopic structure [3–8, 91, 147]. Glass formation may result from dense regions of well-packed molecules [3–5, 13, 140] or a decreasing probability of finding mobile regions [10–12, 15, 17, 126, 127, 148, 149]. As no structural mechanisms for this transition have been found, many explanations rely on dynamic mechanisms. Some theoretical explanations focus on the idea of dynamical heterogeneities [10–13, 15, 126, 148, 150] The underlying concept is that, for any molecule to move, all molecules within a surrounding region must "cooperate" in their movement. As the glass transition is approached the sizes of these regions grow, causing the rise in macroscopic viscosity [15]. While generally accepted, and with some global features confirmed, the details of this conceptual picture remain in debate [10–12].

7.2.1 Rotational and translational diffusion

As discussed in Chapters 1 and 5, micron sized particles suspended in a fluid undergo random Brownian motion, known as diffusion. Such particles diffuse both translationally and rotationally. Relationships regarding translational and rotational diffusion are discussed in Chapter 5. A thorough discussion regarding diffusion coefficients, their relationship to the MSD and MSAD, and relevant derivations are provided in Chapter 5, specifically Sec. 5.3.

The purpose of the work discussed here is to discuss the relationship between D_{R} and D_{T}. As discussed in Sec. 5.3.1, both D_{T} and D_{R}, for translational and rotational motion respectively, depend on temperature T and viscosity η in the same way. Thus, for liquids the relationship between the two diffusion coefficients is constant:

$$\frac{D_{\mathrm{T}}}{D_{\mathrm{R}}} = \mathit{constant} \ \ (= \frac{4}{3}a^2 \ \ \text{for spheres}). \tag{7.1}$$

Therefore, with a dramatic increase in viscosity we will expect a dramatic slowing of both types of motion. However, as the viscosity rises sharply near T_g, Eqn. 5.16

appears to break down [18, 136–140, 151] and in several cases, also Eqn. 5.19 [59, 152–158] In particular, molecules appear to translationally diffuse faster than would be expected from the bulk viscosity η, although one simulation has seen the opposite effect [61]. In all these cases, Eqn. 7.1 no longer holds; this was observed relatively recently even in an experiment where the glass transition was approached by increasing the pressure at constant T [159].

A breakdown of Eqn. 7.1 is considered a physical paradox as it means that two types of motion, which are analogously related to the same set of physical parameters, actually respond to these conditions in markedly different ways [139, 140].

To understand the challenge of many prior experimental measurements of rotational motion, it is useful to consider a second way to characterize rotational diffusion, based on the original Debye derivation [62]. This model considers rotational diffusion as a random walk of the direction of $\hat{p}(t)$ [58, 63]. The random walker diffuses like a point on the surface of the unit sphere, with diffusion constant D_R at short times. Start with the initial condition $\hat{p}(0) = \hat{z}$, and then solve the diffusion equation on a sphere. This leads to the probability distribution for an angular displacement $\psi \equiv |\vec{\delta\varphi}|$ in a time Δt:

$$P(\psi, \Delta t) = \frac{1}{2}\sum_{l=0}^{\infty}(2l+1)P_l[\cos\psi]\exp[-l(l+1)D_R\Delta t], \tag{7.2}$$

where $P_l(x)$ are the Legendre polynomials [58]. The probability of finding a rotation between ψ and $\psi + d\psi$ is equal to $P(\psi)\sin(\psi)d\psi$. For small Δt such that $\psi \ll 1$ radian, $\langle\psi^2\rangle \approx 4D_R\Delta t$ [139], as the sphere's surface locally looks like a 2D plane. Recent work favors Eqn. **??** as ψ is bounded between 0 and π, and thus it is harder to study large angular motions [59–61], whereas $\vec{\varphi}$ is unbounded.

Related to $P(\psi)$ is the reorientational time correlation function:

$$C_{\text{reor}}(\Delta t) = \langle\hat{p}(t+\Delta t)\cdot\hat{p}(t)\rangle = \langle P_1(\cos\psi)\rangle; \tag{7.3}$$

P_1 is the $l = 1$ Legendre polynomial [142]. C_{reor} is related to $P(\psi)$ as

$$\langle P_1(\cos\psi)\rangle = \int_0^{\pi} d\psi \sin\psi P_1(\cos\psi)P(\psi) = \exp[-2D_R\Delta t]. \tag{7.4}$$

Experimental techniques such as dielectric relaxation and infrared spectroscopy measure $\langle P_1(\cos\psi)\rangle$ [**?**]. Typically they observe $\langle P_1(\cos\psi)\rangle \sim \exp[-\Delta t/\tau_1]$. One could then deduce D_R as $D_R = (2\tau_1)^{-1}$, to match the prediction of Eqn. 5.19, assuming that the full distribution $P(\psi, \Delta t)$ is given by Eqn. 7.2. However, for supercooled liquids, the rotational correlation time may not be so simply related to D_R [59–61, 139, 142, 156].

In particular, as noted in Sec. 1.1, as the glass transition is approached, molecules move in coordinated localized groups, rather than as non-interacting random walkers.

These dynamical heterogeneities violate the assumptions behind Eqn. 7.2, and thus it may not be possible to learn about D_R from τ_1 [61, 141]. Note also that some experiments find stretched exponential behavior, $C_{\mathrm{reor}}(\Delta t) \sim \exp[-(\Delta t/\tau)^{\beta}]$ with $\beta < 1$, and thus define a rotational time scale from the integral of $C_{\mathrm{reor}}(t')dt'$ [137]; here it is clearer that there is not a direct relationship between C_{reor} and D_R.

Similarly, some experiments measure rotational motion from $\langle P_2(\cos\psi)\rangle$ using techniques such as Raman scattering, fluorescence depolarization, NMR, and some forms of infrared spectroscopy [58]. These experiments measure the rotational decorrelation time τ_2. It would be possible to determine D_R as $D_R = \frac{1}{6}\tau_2^{-1}$, but this may not work if Eqn. 7.2 no longer applies in a glassy sample.

A final complication for rotational diffusion is that many molecules have more than two rotational degrees of freedom, and it has been shown that rotational motion along different directions can exhibit widely differing characteristics at supercooled temperatures [61], although this is not always true [60]. All of these ways to consider the rotation of an orientation vector $\hat{p}$ are easily applied to other orientation vectors attached to a complex molecule [59–61].

7.2.2 Colloidal glass transition

The inability to directly observe molecular interactions has relegated investigation of rotational dynamics to computer simulations [60, 61] and, more recently, simple 2D model systems [160], which have produced compelling results suggesting correlations between translational and rotational dynamical heterogeneities. Alternatively, as discussed in Chapter 2, colloidal suspensions have proven to be a reliable avenue for experimentally exploring the microscopic dynamical processes at play: colloids have a glass transition [24] and exhibit cooperatively rearranging regions [17, 74]. Moreover, many colloids behave as hard sphere systems, arguably the simplest system in which to study the most fundamental features the glass transition. An important advantage of colloids is that individual particles can be followed in 3D using a confocal microscope, which permits direct observation of spatially heterogeneous dynamical processes [17, 25, 26] that can be difficult to study with more conventional methods that average over many particles in the bulk sample.

While spherical colloidal particles provide the simplest realization of a glass, they fail to capture the rotational dynamics that are thought to be important in most glass formers. Probing the rotational dynamics therefore requires the introduction of non-spherical particles. En route to developing monodisperse suspensions of non-spherical particles, we study individual anisotropic tracer particles in dense bidisperse colloidal suspensions of beads, isolating the effect of crowding on rotational diffusion. The essential question we wish to address is: does the decoupling of translational diffusion from rotational diffusion and viscosity depend critically on having a glass formed entirely from non-spherical particles or is it a more generic feature of disorder and the crowding that accompanies the approach to the glass transition? With recent advances in colloidal chemistry [33] and the development of "colloidal molecules" [32, 161] and the means to track their motion [22, 23], we are in a position to address this question.

In our experiments we use high speed confocal microscopy to follow the 3D translational and rotational motion of tracer colloidal clusters in a dense amorphous suspension of spheres at volume fractions ϕ ranging from 0 to 0.565. We find that rotational diffusion of isolated colloidal clusters is tightly coupled to the suspension viscosity η while translational diffusion decouples for a deeply supercooled system. This shows that the decoupling of translational and rotational diffusion is a generic feature of glass-formers that results from crowding and not peculiar to glasses formed from anisotropic particles [18, 162]. Upon decoupling, translational motion becomes facilitated by cooperative rearrangements with surrounding particles, exhibited by "cage-breaks". Conversely, we do not observe any type of hops in orientation, and the divergence between the two types of motion increases with ϕ.

7.3 Sample preparation

Our colloid is a suspension of spherical colloidal poly-methyl-methacrylate (PMMA) particles, sterically stabilized by a thin layer of poly-12-hydroxystearic acid [33, 35] to prevent interparticle attraction. To prevent crystallization we use equal volume fractions of two particle species, 725 and 1100 nm in radius (2.5% polydispersity for each species) [163]. The particles are suspended in a mixture of ∼85/15 (w/w) cyclohexyl bromide (CHB, Fluka, 99%) and *cis*-decahydronaphthalene (*cis*-decalin or DEC, Aldrich, 99%), which effectively matches both the density and index of refraction of the particles. To screen the repulsive charge between the particles, we saturate the solvent mixture with an appropriate amount of tetrabutylammonium bromide (TBAB, Aldrich, 98%) [28]. We add a trace amount of PMMA colloidal clusters, already suspended in a similar CHB/DEC mixture, synthesized using the method developed by Elsesser, *et al.* [22]. The clustered particles are ∼1.3 μm in radius, according to both static light scattering measurements and calculation of diffusion coefficients using optical particle tracking techniques [22, 55]. Although the clustered particles stick together with van der Waals attractions, the clusters are stable and do not aggregate with other particles in even the most dense suspensions [32]. Only the cores of the clustered particles are fluorescently labeled [22], making the clusters easily visible among the rest of the colloid, which is invisible under fluorescent microscopy. The poor z-resolution of optical microscopy makes labeling only the particle cores a necessity in order to clearly distinguish the clustered particles from one another [22]. An example of a core-shell cluster is shown in Fig. 7.1.

Samples were prepared for observation by filling rectangular glass capillaries (Vitrotubes, 0.10 × 2.0 mm I.D.) and were sealed with optical adhesive (Norland #68). See Sec. 4.3.2 for a complete discussion regarding the use of rectangular capillaries. In between the preparation of each sample, we incrementally dilute the colloid using the original supernatant, producing samples with volume fractions ϕ ranging from ~0.39 to ~0.57. We extrapolate the precise volume fractions of each sample by recording the mass of the colloid before and after each dilution, and then calculating the colloid's final ϕ by massing it before and after evaporating the solvent.

In retrospect, some minor design changes to these sample chambers would have been desirable. While it would potentially be a much more fragile sample chamber, it would be useful to attach the capillaries to a slide in such a way that both sides would be accessible for viewing. In this way, portions of the sample that were closer to one side would be more easily viewable than optically penetrating 50+ μm of colloid from the far side. Also, using capillaries with a cross-sectional height of roughly 200 μm would be useful simply for observing more sample. Recall, that particles closer than $30 - 40$ μm to the boundaries may suffer some wall affects, therefore only a $\sim$ 30 μm thick volume of the sample's interior is useful to us. With better control over cluster purity and yield, use of sugar-sealed vials may be investigated in the future, as discussed in Sec. 4.3.

7.4 Data acquisition

We locate individual tetrahedral clusters within the colloid, ensuring that they are at least 35 μm from the nearest boundary to avoid wall effects. We image the clusters using a Leica TCS SP5 confocal microscope, equipped with an Argon laser ($\lambda_0 = 514$ nm) and an oil-immersion objective (Leica, 63×, 1.4 NA). A $25\times25\times25$ μm^3 volume is scanned in 0.8 s with a pixel size of approximately 100 nm in x & y and 200 nm in z. The lag-time Δt between each scan is adjusted, from $\Delta t = 20$ s to 90 s, depending on the viscosity of sample. The result of a typical confocal scan of a diffusing cluster is shown in Fig. 7.1A. While the cluster in Fig. 7.1 is imaged in a clear open volume of solvent, quality index-matching of the colloid provides comparable image quality from even the most densely packed samples.

7.5 Tracking cluster trajectories

We identify the horizontal and vertical positions of particles within a cluster to an accuracy of 0.02 μm and 0.04 μm , respectively, for the duration of experiment [55]. By averaging, the coordinates of the center of clusters are twice as accurate. We further enhance accuracy by adjusting the particle coordinates to better match those of true tetrahedron, using a technique explained in Ref. [23].

To determine the translational trajectory of the cluster's center of mass, we calculate the mean of the particle coordinates, providing the coordinate of the cluster's center of mass at each time. We plot the center's trajectory for a range of ϕ in Fig. 7.2. To determine the cluster's orientation we follow the method described in [23]. First,

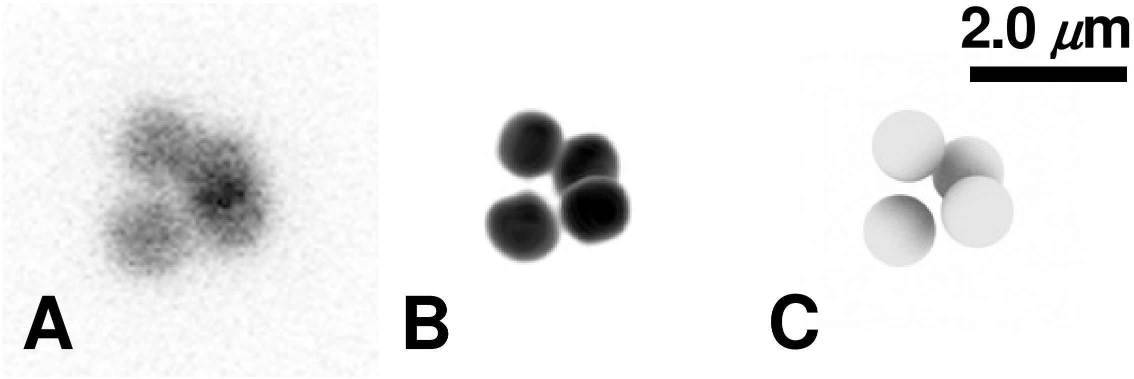

Figure 7.1: Visual representations of a colloidal tetrahedral cluster, visualized using a confocal microscope. Only the core of each particle is fluorescently labeled, surrounded by a blank undyed shell of PMMA, making each particle visually distinct from its clustered neighbors. (A) and (B) have been inverted for clarity. (**A**): Composite, calculated by taking the mean of a stack of cross-sections. The composite images allow us to see through the cluster, where the overlap between multiple beads appear black in the image. (**B**): Projection of a 3D reconstruction. (**C**): Projection of a 3D rendering of spheres at the centers of the particle coordinates, as determined by our tracking algorithms [23, 55]. The sphere diameters are roughly equal to that of the fluorescent cores.

we define a unit vector $\hat{\mathbf{u}}_1$ pointing from the center of the cluster to the center of one particle in the cluster. We then follow the orientation of this vector at each successive time thereby mapping out its angular trajectory. We illustrate cluster orientations in Fig. 7.2 as traces of the unit vector's tip on the surface of a unit sphere.

7.6 Mean square displacement and diffusion

The random translational and angular Brownian motion of a particle is characterized by its translational and rotational diffusion coefficients, discussed in Sec. 5.2. For an arbitrary 3D object possessing no special symmetries, there are three translational and three rotational diffusion coefficients. Because of its high symmetry, however, the diffusive motion of a tetrahedron is characterized by only one translational and one rotational diffusion coefficient. Therefore, we can quantify the tracer mobility in this system using only the mean square displacement (MSD) of the center of mass and the mean square angular displacement (MSAD) as described above.

For translational diffusion the MSD grows linearly in time without bound according to the relation

$$\langle \Delta \vec{r}^2(\Delta t) \rangle = \langle [\vec{r}(t+\Delta t) - \vec{r}(t)]^2 \rangle = 6 D_T t \, . \tag{7.5}$$

Thus we obtain the translational diffusion coefficient D_T from a measurement of the MSD. However, a straightforward similar definition of the MSAD is bounded in time as the unit vector $\hat{\mathbf{u}}_1$ is confined to a unit sphere, complicating the determination of the rotational diffusion coefficient D_R. To remedy this problem, we follow the procedure described in Ref. [59] and define a vector rotational displacement

$$\vec{\varphi}(\Delta t) = \int_{t}^{t+\Delta t} \Delta\vec{\varphi}(t')dt' \tag{7.6}$$

over the time interval $[t, t + \Delta t]$. The direction of vector $\Delta\vec{\varphi}(t')$ is given by the cross product $\hat{\mathbf{u}}_1(t) \times \hat{\mathbf{u}}_1(t + \Delta t)$, which is aligned along the axis of rotation, and its magnitude is given by $|\Delta\vec{\varphi}(t')| = \cos^{-1}(\hat{\mathbf{u}}_1(t) \cdot \hat{\mathbf{u}}_1(t + \Delta t))$. The unbounded MSAD is then given by

$$\langle \Delta\vec{\varphi}^2(\Delta t)\rangle = \langle[\vec{\varphi}(t + \Delta t) - \vec{\varphi}(t)]^2\rangle = 4D_R t \ , \tag{7.7}$$

analogous to the MSD defined in Eq. 7.5 above. Thus we obtain a measurement of the rotational diffusion coefficient D_R as well as a direct comparison between the MSAD and MSD.

One caveat in considering the rotational trajectory about only a single axis of rotation for a given cluster is that significant dynamical processes may be overlooked. Therefore we consider 4 orientation vectors, each extending from the cluster's center to the center of each of the clustered particles. We evaluate the MSADs for each vector and then calculate their mean, i.e. the MSAD include an ensemble average of the 4 axes of rotation, unlike the MSD reported here. We plot the MSAD in Fig. 7.3B.

Plateaus begin to appear in the MSAD (Fig. 7.3B) for $\phi > 0.50$, but are the result of uncertainty due to noise.

For monodisperse supercooled colloidal liquids, the occurrence of plateaus in the MSD is expected within the time scales reported here [17]. However, bidisperse colloids can exhibit heightened fluidity and greater fragility [164]. Short plateau or steps are present in the MSD of $\phi \sim 0.565$, but are short due to the relatively poor statistics from a single tracer in a very dense medium. In other words, the slow dynamics of this sample would require either observation for a significantly greater period of time, or an ensemble of clusters in the sample. Either method would produce an improvements in statistics and therefore more well defined plateaus in the MSAD.

We calculate the uncertainty of the MSAD due to noise levels for both $\phi \sim 0.54$ and $\phi \sim 0.565$ using Eqn. 5.27, and by following the technique described in Sec. **??**. The technique was developed by Gary L. Hunter and explained in Ref. [23]. We begin the calculation of the uncertainty $\langle\Delta\theta^2\rangle$ by considering a respective tetrahedral cluster's motion within its translational frame of reference by fixing its center to the origin of our coordinate system. The Cartesian coordinates of the clustered particles are then converted to a spherical coordinate system, which we use to calculate a histogram of the radial component of positions. We fit a Gaussian to this distribution, whose standard deviation σ and offset R reflect the width of uncertainty in the particles'

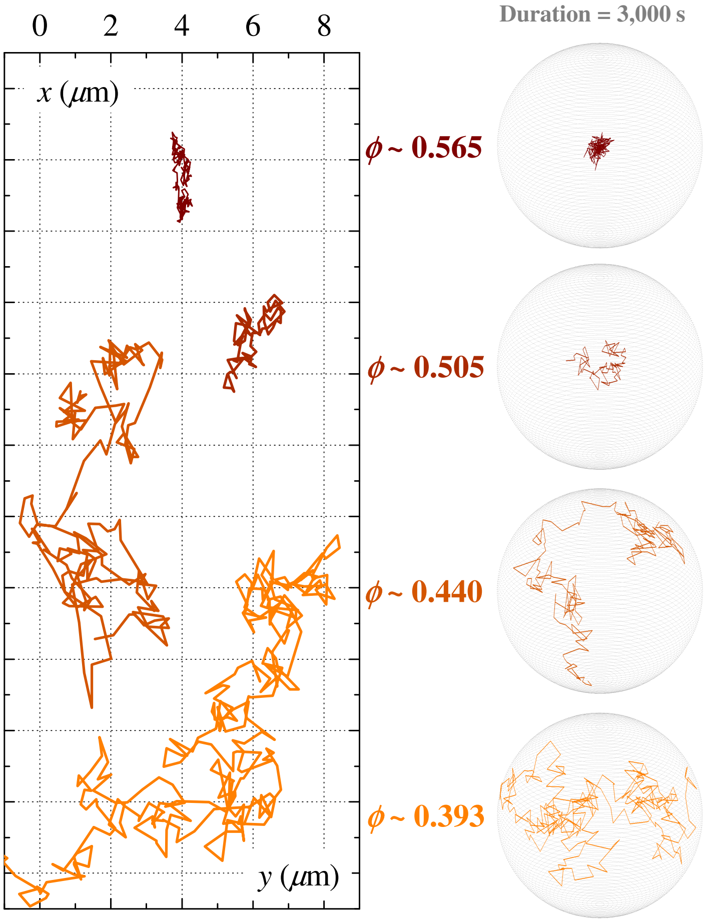

Figure 7.2: Translational and rotational trajectories for clusters at different ϕ. The plots on the left are 2D projections of 3D trajectories of the center of mass of clusters. The plots on the right are rotational trajectories depicted by a trace of a cluster's orientation across the surface of a unit sphere in the translating frame of reference of the cluster. As noted in the figure, each trajectory spans the same duration of 3,000 s. The translational trajectories only share the same set of axes for comparison, and are each from a unique sample.

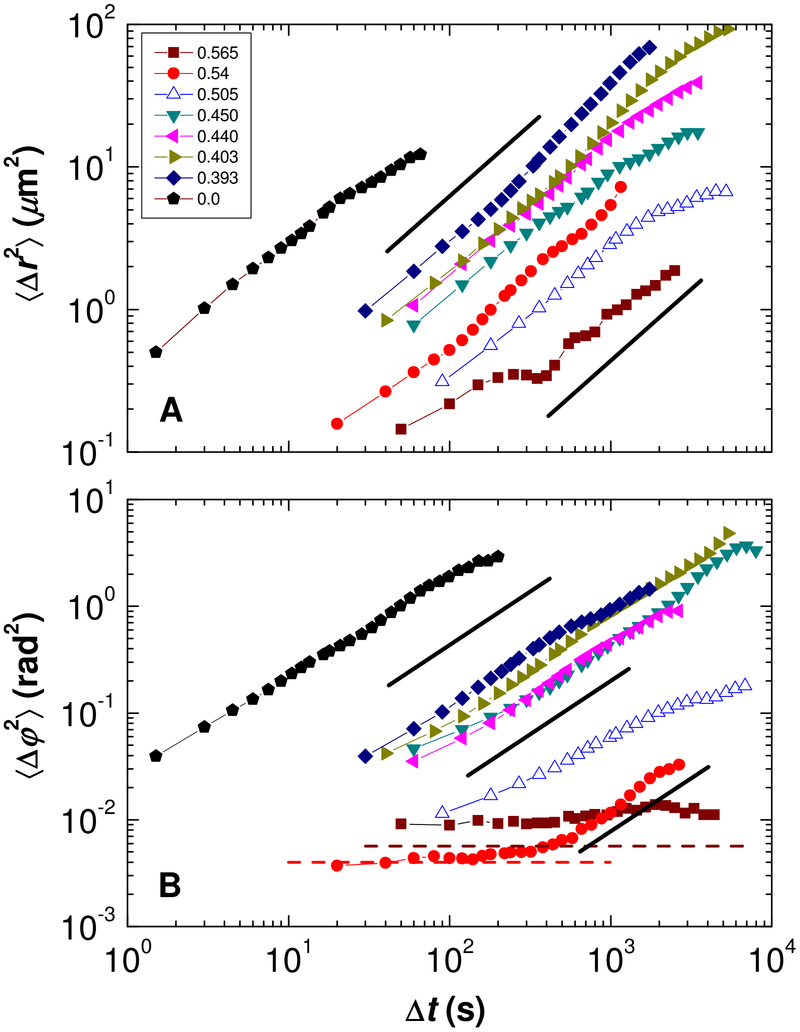

Figure 7.3: Translational and rotational mobility for range of volume fractions ϕ. (**A**) Mean square displacement (MSD) $\langle \Delta x^2(\Delta t) \rangle$. (**B**) Mean square angular displacement (MSAD) $\langle \Delta \varphi^2(\Delta t) \rangle$, as evaluated by Ref. [59]. The empty symbols represent data from a pentamer cluster, the solid symbols are from tetrahedra. The straight lines show a slope of 1. The horizontal dashed lines represent the "noise" of the correspondingly colored data sets; MSAD below these levels cannot be resolved. The noise-level for $\phi \sim 0.565$ is higher than for $\phi \sim 0.54$ due to an increase in optical distortions between the two datasets. There is inherent uncertainty in this data since each curve represents only a single cluster that may be subject to inhomogeneous structural and temporal relaxation processes that become significant with increasing ϕ [17]. The duration of each data set is limited by our inability to overcome basic experimental limitations such as photo bleaching and the available field of view. The level of uncertainty due to noise in the images varies between each data set.

angular displacement and the mean distance between a particle's center and the center of the cluster, respectively. Using the values for R and the standard deviation, we are able to calculate the uncertainty as

$$\langle \Delta\theta^2 \rangle = \frac{6\sigma^2}{4R^2} \tag{7.8}$$

by using Eqn. 5.27.

The specific amount noise varies for each data set. The rotational displacements of clusters in data from $\phi \sim 0.54$ and $\phi \sim 0.565$ can at times be so slight that they are comparable to the levels of uncertainty. In Fig. 7.3B, the MSAD for $\phi \sim 0.54$ and $\phi \sim 0.565$ are plotted as solid red circles and solid maroon squares, respectively. We plot the levels of uncertainty for each data set with correspondingly colored horizontal dashed lines. The offset of these lines are calculated using Eqn. 7.8 and denote each respective data set's level of uncertainty.

The initial plateau of the MSAD of $\phi \sim 0.54$ for $\Delta t \lesssim 200$ s, is roughly equal to the uncertainty of that data set. For $\Delta t > 200$ s the magnitude of the MSAD rises beyond the uncertainty, yielding reliable data that we use to calculate this cluster's rotational diffusion coefficient D_{R}. The cluster at $\phi \sim 0.565$, a higher volume fraction, completes only the slightest angular displacements, which results in an MSAD that remains mostly flat for the full range of Δt. Seemingly, the cluster is never observed to reach a diffusive regime of rotational motion.

7.7 Diffusive decoupling

We determine D_{T} and D_{R} by calculating the slope over the diffusive regimes of the MSD and MSAD curves; the linear portion beyond the upturn. Calculation of D_{T} and D_{R} is explained in Sec. 5.3. We plot D_{T} and D_{R} on a shared axes in Fig. 7.4 in terms of both ϕ and η, where η has been interpolated from data reported in Ref. [165]. Figure 7.5 depicts the interpolation process, where we converted the normalized viscosity data from Ref. [165] to values of the true bulk viscosity of our colloidal suspensions. Next, we perform a simple linear interpolation between adjacent data points, shown as solid black triangles in Fig. 7.5, to calculate values of η that correspond to the values of ϕ measured from our samples. The viscosities reported in Ref. [165] are for monodisperse colloidal suspensions. Ideally, we would instead use viscosities of bidisperse suspensions, like the one used in our own experiments. However, a monodisperse suspension serves as a reasonable first order approximation.

Rotational diffusion remains coupled with η for the full range of ϕ, while translational diffusion decouples for $\phi \geq 0.51$. For comparison with molecular experiments, we include a line of slope -0.73 in Fig. 7.4. Fits to data from molecular experiments have determined that translational diffusion decouples from viscosity in a very large number of fragile glass formers, and goes as $\eta^{-0.73---0.75}$ [10, 18, 166]. Such fits are in excellent agreement with computer simulations and theoretical models, also showing that D_{T} in super cooled fragile molecular glass formers scales with $\sim \eta^{-0.73---0.78}$ [10, 167]. Our translational and rotational data in Fig. 7.4 shows good agreement with the slopes of $\eta^{-0.73}$ and η^{-1}, respectively, and therefore good agreement with fragile molecular glass formers in general. Decoupling between D_{R} and D_{T} in our colloidal system is most certainly real as the two values diverge by almost two orders of magnitude for $\phi \geq 0.51$.

Note that we calculate D_{T} and D_{R} for every ϕ, with the exception of $D_{\mathrm{R}}(\phi \sim 0.565)$. Being so close to ϕ_g, the cluster never exhibits appreciable angular displacements during the experiment's 5,000 s duration. Observation would need to continue for an extra decade of time in order to observe diffusive rotational dynamics, given the prolonged relaxation times observed at this concentration [44]. To determine $D_{\mathrm{R}}(\phi \sim 0.565)$, we make an intuitive approximation based on our data and the Stokes-Einstein-Debye model, denoted by this data's significant error bars. The coefficients for the pentamer, denoted by the solid symbols in Fig. 7.4, are slightly lower than the trend set by data for tetrahedron.

The pentamer, a triangular dipyramid [32], is larger than the tetrahedral clusters. Unlike the tetrahedron, the pentamer has a primary axis of symmetry. Therefore, in the dilute limit, it can be accurately modeled as an ellipsoid, whereas the tetrahedron has been shown to be very accurately modeled by a sphere [168]. While subtley different, the data for the pentamer is included here since it is not significantly different and suggests that decoupling for a pentamer occurs in the same way as for a tetrahedron. It helps establish that the decoupling effect being observed is, to some degree, robust to shape.

To understand what changes occur at $\phi \sim 0.54$ to cause decoupling, we make a direct qualitative comparison between the cluster's translational and rotational trajectories in Fig. 7.6. At $\phi \sim 0.54$, cage-trapping behavior becomes prominent in the translational trajectories but not the rotational ones, plotted in Figs. 7.6**A** and **C**, respectively. Inspection of the MSAD data, plotted with solid red circles in Fig. 7.3**B**, reveals a plateau and then upturn at $\Delta t \sim 300$ s. Such an upturn could be interpreted as an indication of cage-breaking behavior in the cluster's rotational trajectory, a relationship that is thoroughly discussed in Sec. 5.3.3. However, as described in Sec. 5.3.2 and earlier in this section (Sec. 7.6), the MSAD's plateau is at the level of noise indicated by the horizontal red dashed line in Fig. 7.3B. The upturn, which occurs at $\Delta t \sim 300$ s, indicates the average time it takes for the cluster to rotate enough for our particle tracking algorithms to detect beyond the noise levels. Recall from Sec.5.3.2 and Ref. [23] that our rotational tracking methods allow us to resolve angular displacements of at least 1.6°. The angular displacements over time intervals of $\Delta t < 200$ s are too subtle to be detected using our techniques.

By considering trajectories from samples with values of ϕ that are greater and smaller than $\phi \sim 0.54$, where decoupling between translational and rotational diffusion first becomes appreciable, we gain some further insight into the role of microscopic

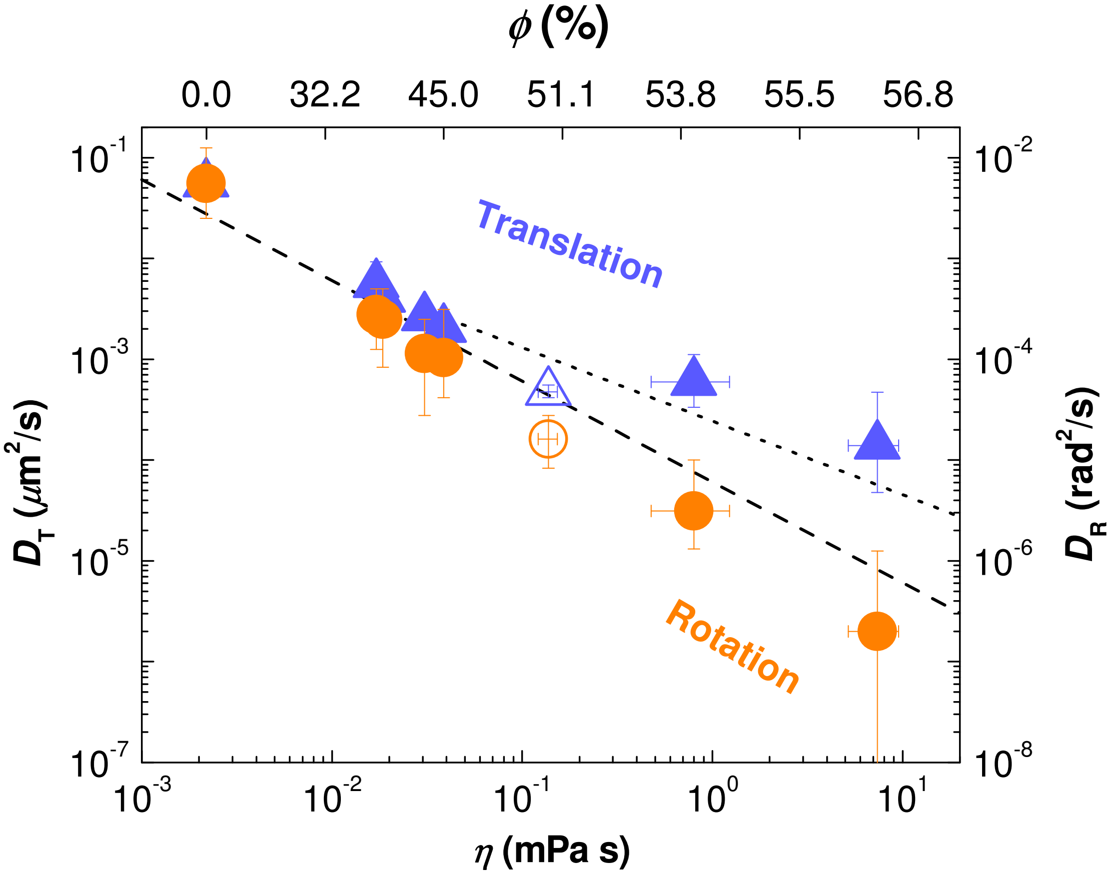

Figure 7.4: Diffusion coefficients of tracer clusters for different η and ϕ. The values of η (bottom) are interpolated from the data published in Ref. [165] using our own ϕ (top) values. Both vertical axes have the same scale, but have been shifted to overlap the coefficients at $\phi = 0.0$. Blue triangles: translational diffusion coefficients D_{T} (left axes) Orange circles: rotational diffusion coefficients D_{R} (right axes). Open symbols: data from a pentamer, $n = 5$ particles arranged as a triangular dipyramid [32]. Dashed and dotted lines show η^{-1} and $\eta^{-0.73}$ dependencies respectively.

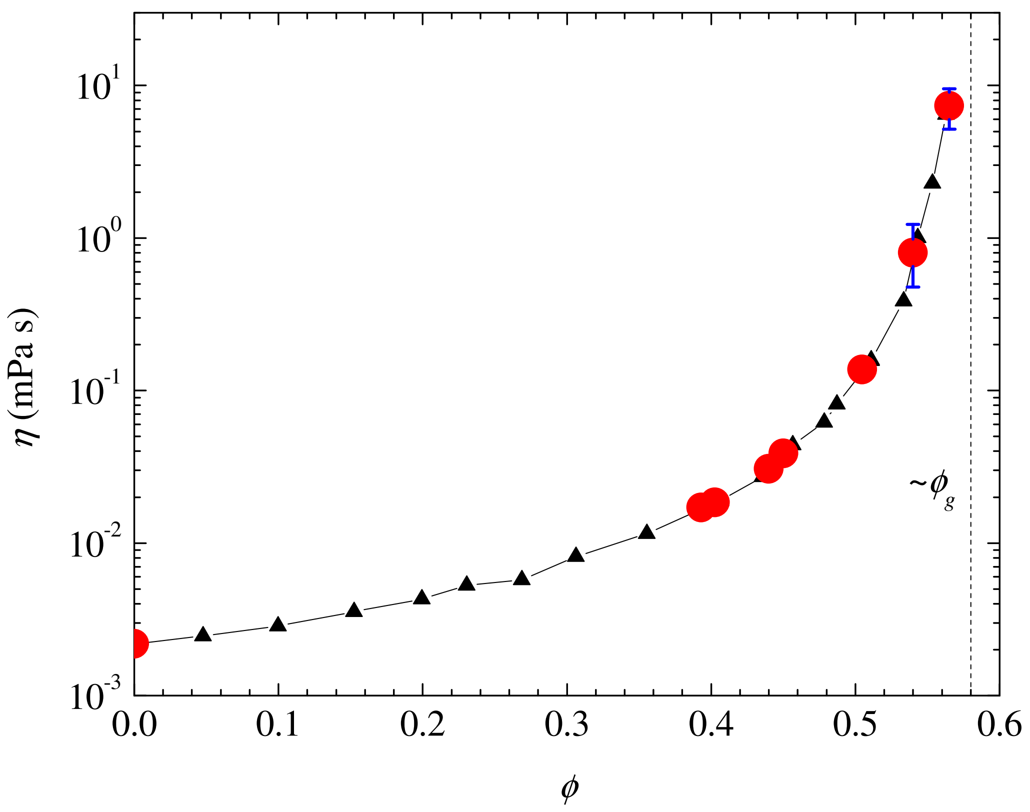

Figure 7.5: Plot of viscosity of monodisperse colloidal PMMA particles for broad range of ϕ, replotted from Ref. [165]. The original data from Ref. [165] was the colloid's viscosity normalized by the solvent's viscosity: η_0/μ, where η_0 is the bulk viscosity of the colloid and μ is the viscosity of the solvent. Multiplying the normalized data by the viscosity of our solvent mixture, $\mu = 0.00218$ mPa s, gives us the data plotted here solid black triangles. The solid red circles represent the data from our experiments, where we measured the volume fractions of each of our samples and then calculated their η with a simple linear interpolation along the data plotted in black. The amount of uncertainty in our results for all but the two most dense samples is indicated by the size of the red symbols.

rearrangements in the greater diffusive decoupling. The translational and rotational trajectories from $\phi \sim 0.505$, shown for a duration of 3,000 s in Fig. 7.2, are both qualitatively similar. Meanwhile, very close to the glass transition at $\phi \sim 0.565$, there are clear cage-breaking events in the translational trajectory, but none in the rotational trajectories. In fact, the cluster of particles hardly appears to be rotating at all.

We can make a more quantitative comparison between the trajectories of $\phi \sim 0.54$ by calculating the translational and rotational displacements over a given lag-time Δt:

$$\Delta x(\Delta t) = \Delta x(t + \Delta t) - \Delta x(t), \tag{7.9}$$

and repeat for the y and z Cartesian components to calculate the sum displacement

$$\Delta r(\Delta t) = \sqrt{\Delta x^2 + \Delta y^2 + \Delta z^2}. \tag{7.10}$$

The rotational displacement, $\Delta\varphi(\Delta t)$, can be calculated in an analogous way using the rotational trajectory.

We plot both $\Delta r(\Delta t)$ and $\Delta\varphi(\Delta t)$ in Figs. 7.6A and C, respectively. For the sake of comparison we use $\Delta t = 300$ s for both, the lag-time for which the MSAD begins to describe true particle dynamics, rather than the noise found for shorter lag-times. In Fig. 7.6A there are three prominent peaks, each spanning a duration of ~500 s, that signify the largest translational displacements completed by the cluster's barycenter. Between plots A and C we have drawn four color bars that span the periods between the large translational displacements as a way of visually comparing the translational and rotational displacements. Also, we have colored the corresponding segments of the translational trajectory in Fig. 7.6B in the same way. Comparison of Figs. 7.6A and C reveals, as labeled by the colored segments, that the peaks in translational displacement have highlighted the periods over which the cluster is cage-trapped, separated by significant "breaks" or displacements. However, between the translational and rotational data in Figs. 7.6A and C, no relationship seems to exist. Seemingly, for $\phi > 0.54$, rotational motion simply continues to slow monotonically, while the cluster's translational motion assumes more heterogeneous dynamics. The difference between the two types of displacements is in correspondence with the results of Fig. 7.4, where diffusive decoupling is observed over this range of ϕ.

Therefore, we conclude that this is the reason for diffusive decoupling in our colloidal system: the heterogeneous nature of translational motion, which arises in the suspension's "supercooled" regime, allows for translational motion that is faster than what would be expected for a sample of this viscosity. The absence of sudden cage-breaking behavior for the cluster's rotational motion, however, results in strong coupling between rotational motion and the sample's bulk viscosity, even when very close to the glass transition. Our findings are in excellent agreement with experiments studying ortho terphenyl (OTP), a fragile molecular glass former [18]. Likewise, the colloidal glass transition is itself fragile [169]. However, our findings are in disagreement with recent computer simulations of the molecular dynamics of OTP [61]. The

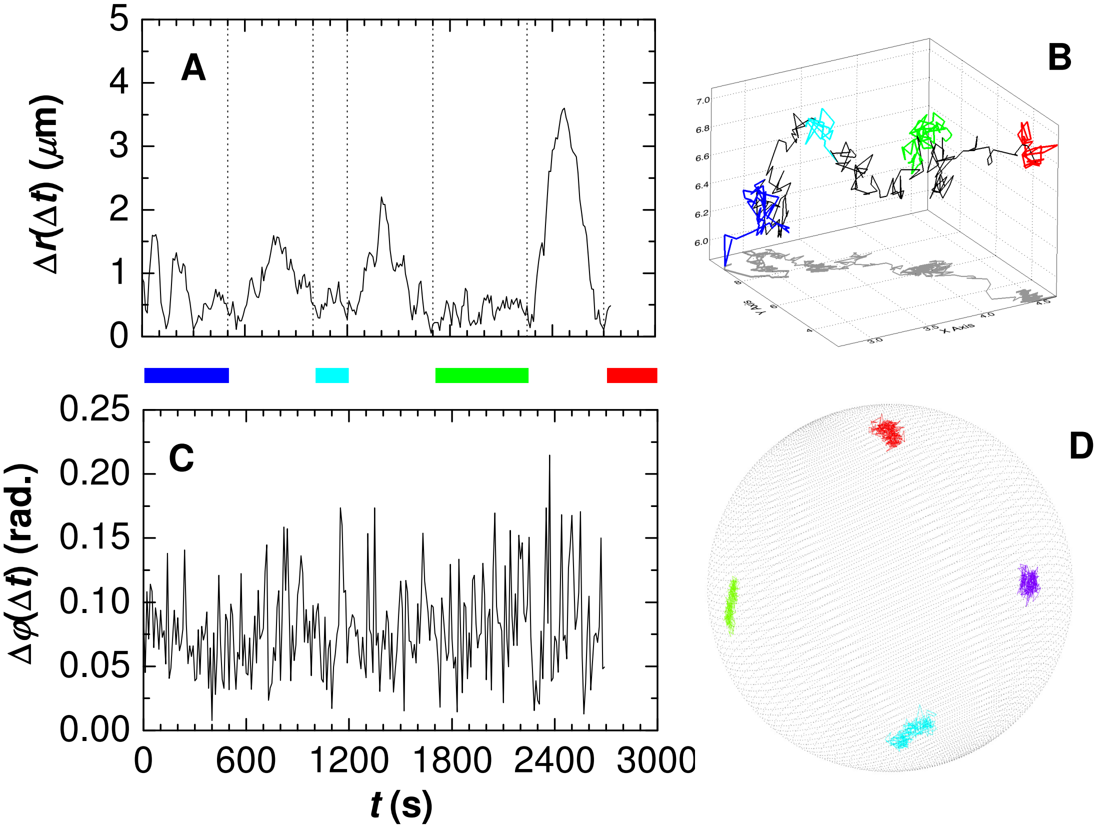

Figure 7.6: Comparison of translational and rotational displacements. **(A)** The displacement of a tetrahedral cluster at $\phi \sim 0.54$ over consecutive time intervals of $\Delta t = 300$ s. The vertical dashed lines in (A) correspond with significant displacements shown in (B). The color bars signify to periods when the cluster is "caged", not making a major displacement, and correspond to the matching colored segments of the trajectory in (B). **(B)** A 2D projection of the 3D trajectory of the clusters barycenter. The colored segments here correspond to the periods denoted by the colored bars between plots (A) and (C). **(C)** The angular displacement over $\Delta t = 300$ s. **(D)** Traces of each of the 4 clustered particles on the surface of a unit sphere, in the cluster's frame of reference.

details of this disagreement are discussed in Chapter 8. If nothing else, our findings show that a simple near hard-sphere fluid exhibits many of the complex properties associated with much more complex materials. Therefore, we have shown the level of abstraction necessary for any theoretical treatment or modeling of diffusive decoupling in fragile glass formers. More generally, any future theoretical treatments regarding the structural relaxation processes of glass forming materials must make careful consideration of both translational and rotational diffusion.

Chapter 8

Summary of Work and Outlook

8.1 Summary

Through a series of experiments, I have used colloidal suspensions of microscopic Brownian particles to effectively model aspects of the glass transition. High speed laser-scanning confocal microscopy has allowed me to clearly visualize dynamic particle interactions deep within the colloid. Through creative design of experiments, such as the use of a wedge-shaped sample chamber (see Chapter 4) or clusters of fluorescently labeled core-shell particles (see Chapter 7), we have been able to develop significant insight into some of the fundamental mechanisms of the colloidal glass transition.

8.1.1 The Confinement Effect

In Chapter 6 I discuss how confinement of a glass forming liquid can, depending on its interaction with the confining boundaries, increase or decrease the glass transition temperature T_g. Through confinement, we induce glassy behavior in a sample that is otherwise a fluid in the bulk [19]. In this work, we discover the largest dynamic length scale ever observed in a colloidal liquid. Closer investigation of the sample's dynamics, in an effort to probe this dynamic length scale, reveals that confinement of the fluid induces cooperative dynamics among the particles, a hallmark feature of a much more dense (effectively colder) "supercooled" a fluid in the bulk. Our work reveals a relationship between structural configurations, the density layers, and the cooperatively rearranging regions of particles. Structural layering frustrates particle diffusion normal to the sample boundaries, resulting in the cooperative groups of particles to assume a more planar shape. We were able to establish a robust relationship between the morphology of these cooperative groups of particles and the material's overall bulk behavior [21]. Finally, an in-depth look at the interaction between the interface of the suspended particles and the sample boundary highlighted the influence of boundary conditions on a glass forming fluid. Specifically, rougher boundaries further slow particle dynamics, effectively decreasing ϕ_g [20]. Our findings are in good agreement with numerous computer simulations [49, 170]. Also, this work set the stage for further investigations currently being pursued by my colleagues (Gary L. Hunter, undergraduate researchers, etc.).

8.1.2 Rotational Diffusion

Through close collaboration with researchers at NYU, I was able to study the rotational diffusion non-spherical colloidal particles. These non-spherical particles, simply ordered clusters of microspheres, served as tracers of both translational and rotational motion in dense bidisperse suspensions of individual Brownian microspheres. For the first time, through the simultaneous observation of both types of motion, we were able to observe decoupling between translational and rotational diffusion of the clusters. Specifically, we observed good agreement between our experiment and results from fragile molecular glass formers, where rotational diffusion remained coupled with viscosity, while translational diffusion decoupled by the same magnitude as observed in molecular materials. Our findings establish a level of abstraction, the near hard sphere model system, that is capable of accurately describing diffusive decoupling. Through the completion of this work, we developed a suite of techniques for the observation and analysis of the rotational diffusion of colloidal clusters [23].

8.2 Impact and Outlook

8.2.1 The Confinement Effect

Beyond the observation that confinement slows colloidal diffusion, even inducing glassy behavior, the observation of layering, or induced structural order, has perhaps been the most significant contribution of our work to the field of colloidal physics. Frequently, when layering induced by boundaries are observed in experiments, our work is cited [164]. Computer simulations of confined systems have used our results to support their own conclusions, such as how the formation of layers does not push the system out of equilibrium [120, 121]. Similarly, theories have incorporated our findings into their treatment of the subject [171]. Structural order of a variety of types, beyond just layering, are now used to explain various aspects of confinement, and subsequently the glass transition on the whole [172]. Related to layering, our work provided insight into the nature of particle interactions with a hard boundary [173]. In general, a significant impact of our work has been highlighting the relationship between structure and dynamics in hard sphere systems [172].

Continued work in this area is necessary to understand the effect of confinement when layering is somehow frustrated or avoided. Very recent experiments by other groups of scientists have made headway in this area [101, 135]. Most notably, the work by Eral, *et al.* investigated confinement of a colloidal suspension between a smooth and a rough surface. In this way, they were able to directly compare the influence of layering along the smooth surface versus the relative lack of layering along the rough surface, both for one sample of particles at the same ϕ. Supporting our findings [20], they confirm that slowing induced by confinement is predominantly a direct effect of the confining surfaces.

Perhaps the most significant finding in our work that has yet to be further investigated or better understood is the relationship between the large length scale over which confinement is effective in our samples [19] and the size of the cooperatively rearranging groups of particles. The relationship between these two length scales could yield some sort of key to understanding the glass transition in general.

8.2.2 Rotational Diffusion

As stated above, through the good agreement of our colloidal experiments with results from molecular glass formers, our findings establish a level of abstraction that is capable of accurately describing diffusive decoupling. This accuracy may prove to be the most significant impact of this work. Our agreement with molecular fragile glass forming systems should prove interesting to the greater scientific community since the origins of decoupling are not yet well understand. Consider that rotational diffusion in molecular experiments is measured using the Debye model. Recent computer simulations by Lombardo, *et al.*[61] argue that correct calculation of rotational diffusion requires the use of an orientation vector that may span an unbounded range of angles on a unit sphere, in the same way that we have [23]. In short, by utilizing the methods and techniques recommended by Lombardo, *et al.*, we are in agreement with molecular experiments that use the Debye model.

Developing a relationship the rotational and translational trajectories, discussed in Chapter 7, may lead us to a better understanding of the relationship between translational and rotational diffusion. Fundamentally, it is access to three-dimensional particle trajectories and the ability to relate them to the fluid's bulk behavior that give colloids such a significant advantage over other experimental techniques.

A more subtle outcome of our work relates to tracer diffusion. A better experimental understanding of the relationship between the size and shape of a tracer particle and the behavior exhibited by it would be useful for future studies. Specifically, a particle significantly larger than its neighbors will provide a more coarse-grained description of local dynamics than something of similar or even smaller size. Simulations by Zangi, *et al.* have investigated this idea [174], but it would be useful to study this more closely in experiments.

Possibilities for future experiments are numerous. First and foremost, simultaneous direct observation of both the tracer and its surrounding medium is absolutely necessary to develop a more complete understanding of the relationship between cooperative rearrangements and diffusive decoupling. Next, experiments with monodisperse fluids of a single cluster type will introduce a whole new phase behavior and a rich model of different amorphous materials. Related to this would be an investigation of how the relative number of colloidal clusters, compared to the species of monomers, effects the fluid's bulk viscosity. One could even study the effect of confinement on rotational diffusion of clusters, effectively combining the work presented in this dissertation.

Bibliography

[1] C. A. Angell, "Formation of glasses from liquids and biopolymers," *Science*, vol. 267, pp. 1924–1935, Mar. 1995.

[2] P. G. Debenedetti and F. H. Stillinger, "Supercooled liquids and the glass transition," *Nature*, vol. 410, pp. 259–267, Mar. 2001.

[3] F. H. Stillinger, "A topographic view of supercooled liquids and glass formation," *Science*, vol. 267, pp. 1935–1939, Mar. 1995.

[4] M. D. Ediger, C. A. Angell, and S. R. Nagel, "Supercooled liquids and glasses," *The J. Phys. Chem.*, vol. 100, pp. 13200–13212, Jan. 1996.

[5] C. A. Angell, K. L. Ngai, G. B. McKenna, P. F. McMillan, and S. W. Martin, "Relaxation in glassforming liquids and amorphous solids," *J. App. Phys.*, vol. 88, no. 6, pp. 3113–3157, 2000.

[6] W. van Megen and S. M. Underwood, "Glass transition in colloidal hard spheres: Measurement and mode-coupling-theory analysis of the coherent intermediate scattering function," *Phys. Rev. E*, vol. 49, pp. 4206–4220, May 1994.

[7] R. M. Ernst, S. R. Nagel, and G. S. Grest, "Search for a correlation length in a simulation of the glass transition," *Phys. Rev. B*, vol. 43, p. 8070, Apr. 1991.

[8] W. van Megen and P. N. Pusey, "Dynamic light-scattering study of the glass transition in a colloidal suspension," *Phys. Rev. A*, vol. 43, pp. 5429–5441, May 1991.

[9] W. van Megen and S. M. Underwood, "Dynamic-light-scattering study of glasses of hard colloidal spheres," *Phys. Rev. E*, vol. 47, pp. 248–261, Jan. 1993.

[10] M. D. Ediger, "Spatially heterogeneous dynamics in supercooled liquids," *Annual Review of Physical Chemistry*, vol. 51, pp. 99–128, Oct. 2000.

[11] H. Sillescu, "Heterogeneity at the glass transition: a review," *J. Non-Cryst. Solids*, vol. 243, pp. 81–108, Feb. 1999.

[12] S. C. Glotzer, "Spatially heterogeneous dynamics in liquids: insights from simulation," *J. Non-Cryst. Solids*, vol. 274, pp. 342–355, Sept. 2000.

[13] S. A. Kivelson, X. Zhao, D. Kivelson, T. M. Fischer, and C. M. Knobler, "Frustration-limited clusters in liquids," *J. Chem. Phys.*, vol. 101, no. 3, pp. 2391–2397, 1994.

[14] W. Kob, C. Donati, S. J. Plimpton, P. H. Poole, and S. C. Glotzer, "Dynamical heterogeneities in a supercooled Lennard-Jones liquid," *Phys. Rev. Lett.*, vol. 79, pp. 2827–2830, Oct. 1997.

[15] G. Adam and J. H. Gibbs, "On the temperature dependence of cooperative relaxation properties in Glass-Forming liquids," *J. Chem. Phys.*, vol. 43, no. 1, pp. 139–146, 1965.

[16] P. M. Chaikin and T. C. Lubensky, *Principles of Condensed Matter Physics.* Cambridge University Press, reprint ed., Oct. 2000.

[17] E. R. Weeks, J. C. Crocker, A. C. Levitt, A. B. Schofield, and D. A. Weitz, "Three-Dimensional direct imaging of structural relaxation near the colloidal glass transition," *Science*, vol. 287, pp. 627–631, Jan. 2000.

[18] I. Chang, F. Fujara, B. Geil, G. Heuberger, T. Mangel, and H. Sillescu, "Translational and rotational molecular motion in supercooled liquids studied by NMR and forced rayleigh scattering," *J. Non-Cryst. Solids*, vol. 172-174, pp. 248–255, 1994.

[19] C. R. Nugent, K. V. Edmond, H. N. Patel, and E. R. Weeks, "Colloidal glass transition observed in confinement," *Phys. Rev. Lett.*, vol. 99, no. 2, p. 025702, 2007.

[20] K. V. Edmond, C. R. Nugent, and E. R. Weeks, "Local influence of boundary conditions on a confined supercooled colloidal liquid," *The European Physical Journal - Special Topics*, vol. 189, pp. 83–93, Oct. 2010.

[21] K. V. Edmond, C. R. Nugent, and E. R. Weeks, "Influence of confinement on dynamical heterogeneities in dense colloidal samples," *arXiv:1003.0856*, Mar. 2010.

[22] M. T. Elsesser, A. D. Hollingsworth, K. V. Edmond, and D. J. Pine, "Large CoreShell poly(methyl methacrylate) colloidal clusters: Synthesis, characterization, and tracking," *Langmuir*, vol. 27, pp. 917–927, Feb. 2011.

[23] G. L. Hunter, K. V. Edmond, M. T. Elsesser, and E. R. Weeks, "Tracking rotational diffusion of colloidal clusters," July 2011.

[24] P. N. Pusey and W. van Megen, "Phase behaviour of concentrated suspensions of nearly hard colloidal spheres," *Nature*, vol. 320, pp. 340–342, Mar. 1986.

[25] A. D. Dinsmore, E. R. Weeks, V. Prasad, A. C. Levitt, and D. A. Weitz, "Three-Dimensional confocal microscopy of colloids," *App. Optics*, vol. 40, no. 24, pp. 4152–4159, 2001.

[26] V. Prasad, D. Semwogerere, and E. R. Weeks, "Confocal microscopy of colloids," *J. Phys.: Cond. Matt.*, vol. 19, p. 113102, Mar. 2007.

[27] U. Gasser, E. R. Weeks, A. B. Schofield, P. N. Pusey, and D. A. Weitz, "Real-Space imaging of nucleation and growth in colloidal crystallization," *Science*, vol. 292, pp. 258–262, Apr. 2001.

[28] A. Yethiraj and A. van Blaaderen, "A colloidal model system with an interaction tunable from hard sphere to soft and dipolar," *Nature*, vol. 421, pp. 513–517, Jan. 2003.

[29] M. T. Sullivan, K. Zhao, A. D. Hollingsworth, R. H. Austin, W. B. Russel, and P. M. Chaikin, "An electric bottle for colloids," *Phys. Rev. Lett.*, vol. 96, no. 1, 2006.

[30] K. V. Edmond, A. B. Schofield, M. Marquez, J. P. Rothstein, and A. D. Dinsmore, "Stable jets of viscoelastic fluids and Self-Assembled cylindrical capsules by hydrodynamic focusing," *Langmuir*, vol. 22, pp. 9052–9056, Oct. 2006.

[31] A. D. Dinsmore, M. F. Hsu, M. G. Nikolaides, M. Marquez, A. R. Bausch, and D. A. Weitz, "Colloidosomes: Selectively permeable capsules composed of colloidal particles," *Science*, vol. 298, pp. 1006–1009, Nov. 2002.

[32] V. N. Manoharan, M. T. Elsesser, and D. J. Pine, "Dense packing and symmetry in small clusters of microspheres," *Science*, vol. 301, pp. 483–487, July 2003.

[33] M. T. Elsesser and A. D. Hollingsworth, "Revisiting the synthesis of a Well-Known Comb-Graft copolymer stabilizer and its application to the dispersion polymerization of poly(methyl methacrylate) in organic media," *Langmuir*, vol. 26, pp. 17989–17996, Dec. 2010.

[34] A. I. Campbell and P. Bartlett, "Fluorescent Hard-Sphere polymer colloids for confocal microscopy," *J. Colloid Interf. Sci.*, vol. 256, pp. 325–330, Dec. 2002.

[35] L. Antl, J. W. Goodwin, R. D. Hill, R. H. Ottewill, S. M. Owens, S. Papworth, and J. A. Waters, "The preparation of poly(methyl methacrylate) latices in non-aqueous media," *Colloids and Surfaces*, vol. 17, pp. 67–78, Jan. 1986.

[36] R. P. A. Dullens, "Colloidal hard spheres: cooking and looking," *Soft Matter*, vol. 2, pp. 805–810, 2006.

[37] M. E. Leunissen, C. G. Christova, A.-P. Hynninen, P. C. Royall, A. I. Campbell, A. Imhof, M. Dijkstra, R. van Roij, and A. van Blaaderen, "Ionic colloidal crystals of oppositely charged particles," *Nature*, vol. 437, pp. 235–240, Sept. 2005.

[38] R. P. A. Dullens, E. M. Claesson, D. Derks, A. van Blaaderen, and W. K. Kegel, "Monodisperse CoreShell poly(methyl methacrylate) latex colloids," *Langmuir*, vol. 19, pp. 5963–5966, July 2003.

[39] R. P. A. Dullens, E. M. Claesson, and W. K. Kegel, "Preparation and properties of Cross-Linked fluorescent poly(methyl methacrylate) latex colloids," *Langmuir*, vol. 20, pp. 658–664, Feb. 2004.

[40] S. Sacanna and D. J. Pine, "Shape-anisotropic colloids: Building blocks for complex assemblies," *Current Opinion in Colloid & Interface Science*, Jan. 2011.

[41] G. A. Caputo and E. London, "Cumulative effects of amino acid substitutions and hydrophobic mismatch upon the transmembrane stability and conformation of hydrophobic alpha-helices.," *Biochemistry*, vol. 42, pp. 3275–3285, Mar. 2003.

[42] J. N. Israelachvili, *Intermolecular and Surface Forces, Third Edition*. Academic Press, 3rd ed., Nov. 2010.

[43] L. J. Kaufman and D. A. Weitz, "Direct imaging of repulsive and attractive colloidal glasses," *J. Chem. Phys.*, vol. 125, no. 7, p. 074716, 2006.

[44] G. Brambilla, D. E. M. El Masri, M. Pierno, L. Berthier, L. Cipelletti, G. Petekidis, and A. B. Schofield, "Probing the equilibrium dynamics of colloidal hard spheres above the Mode-Coupling glass transition," *Phys. Rev. Lett.*, vol. 102, p. 085703, Feb. 2009.

[45] J. M. Lynch, G. C. Cianci, and E. R. Weeks, "Dynamics and structure of an aging binary colloidal glass," *Phys. Rev. E*, vol. 78, p. 031410, Sept. 2008.

[46] S. R. Williams and W. van Megen, "Motions in binary mixtures of hard colloidal spheres: Melting of the glass," *Phys. Rev. E*, vol. 64, no. 4, p. 041502, 2001.

[47] C. Murray, "Phases of thin colloidal layers," *MRS Bulletin*, vol. 23, no. 10, pp. 33–38, 1998.

[48] D. G. Grier and C. A. Murray, "The microscopic dynamics of freezing in supercooled colloidal fluids," *J. Chem. Phys.*, vol. 100, no. 12, pp. 9088–9095, 1994.

[49] Z. T. Németh and H. Löwen, "Freezing and glass transition of hard spheres in cavities," *Phys. Rev. E*, vol. 59, pp. 6824–6829, June 1999.

[50] L.-W. Teng, P.-S. Tu, and Lin, "Microscopic observation of Confinement-Induced layering and slow dynamics of Dusty-Plasma liquids in narrow channels," *Phys. Rev. Lett.*, vol. 90, p. 245004, June 2003.

[51] A. B. Fontecha, H. J. Schöpe, H. König, T. Palberg, R. Messina, and H. Löwen, "A comparative study on the phase behaviour of highly charged colloidal spheres in a confining wedge geometry," *J. Phys.: Cond. Matt.*, vol. 17, no. 31, pp. S2779–S2786, 2005.

[52] R. Besseling, L. Isa, E. R. Weeks, and W. C. K. Poon, "Quantitative imaging of colloidal flows," *Advances in Colloid and Interface Science*, vol. 146, pp. 1–17, Feb. 2009.

[53] J. Perrin, *Brownian Movement and Molecular Reality.* Dover Publications, Jan. 2005.

[54] A. Einstein, "On the movement of small particles suspended in a stationary liquid demanded by the molecular-kinetic theory of heat," *Annalen der Physik (Leipzig)*, vol. 17, pp. 549–560, 1905.

[55] J. Crocker, "Methods of digital video microscopy for colloidal studies," *J. Colloid Interf. Sci.*, vol. 179, pp. 298–310, Apr. 1996.

[56] J. Challis, "A procedure for determining rigid body transformation parameters," *Journal of Biomechanics*, vol. 28, pp. 733–737, June 1995.

[57] W. Sutherland, "A dynamical theory of diffusion for non-electrolytes and the molecular mass of albumin," *Phil. Mag.*, vol. 9, pp. 781–785, 1905.

[58] G. Williams, "Time-correlation functions and molecular motion," *Chem. Soc. Rev.*, vol. 7, pp. 89–131, 1978.

[59] M. G. Mazza, N. Giovambattista, H. E. Stanley, and F. W. Starr, "Connection of translational and rotational dynamical heterogeneities with the breakdown of the Stokes-Einstein and Stokes-Einstein-debye relations in water," *Phys. Rev. E*, vol. 76, p. 031203, Sept. 2007.

[60] M. G. Mazza, N. Giovambattista, F. W. Starr, and H. E. Stanley, "Relation between rotational and translational dynamic heterogeneities in water," *Phys. Rev. Lett.*, vol. 96, p. 057803, Feb. 2006.

[61] T. G. Lombardo, P. G. Debenedetti, and F. H. Stillinger, "Computational probes of molecular motion in the Lewis-Wahnstr[o-umlaut]m model for ortho-terphenyl," *J. Chem. Phys.*, vol. 125, no. 17, 2006.

[62] P. Debye, *Polar Molecules.* New York: Dover, 1929.

[63] B. J. Berne, P. Pechukas, and G. D. Harp, "Molecular reorientation in liquids and gases," *J. Chem. Phys.*, vol. 49, no. 7, pp. 3125–3129, 1968.

[64] C. A. Angell, "Ten questions on glassformers, and a real space 'excitations' model with some answers on fragility and phase transitions," *J. Phys.: Cond. Matt.*, vol. 12, no. 29, pp. 6463–6475, 2000.

[65] M. L. Williams, R. F. Landel, and J. D. Ferry, "The temperature dependence of relaxation mechanisms in amorphous polymers and other glass-forming liquids," *Journal of the American Chemical Society*, vol. 77, pp. 3701–3707, July 1955.

[66] W. K. Kegel and A. van Blaaderen, "Direct observation of dynamical heterogeneities in colloidal Hard-Sphere suspensions," *Science*, vol. 287, pp. 290–293, Jan. 2000.

[67] R. Candelier, A. W. Cooper, J. K. Kummerfeld, O. Dauchot, G. Biroli, P. Harrowell, and D. R. Reichman, "Spatiotemporal hierarchy of relaxation events, dynamical heterogeneities, and structural reorganization in a supercooled liquid," *Phys. Rev. Lett.*, vol. 105, p. 135702, Sept. 2010.

[68] C. Donati, J. F. Douglas, W. Kob, S. J. Plimpton, P. H. Poole, and S. C. Glotzer, "Stringlike cooperative motion in a supercooled liquid," *Phys. Rev. Lett.*, vol. 80, pp. 2338–2341, Mar. 1998.

[69] A. H. Marcus, J. Schofield, and S. A. Rice, "Experimental observations of non-Gaussian behavior and stringlike cooperative dynamics in concentrated quasi-two-dimensional colloidal liquids," *Phys. Rev. E*, vol. 60, pp. 5725–5736, Nov. 1999.

[70] A. Rahman, "Correlations in the motion of atoms in liquid argon," *Phys. Rev. Online Archive (Prola)*, vol. 136, pp. A405–A411, Oct. 1964.

[71] A. S. Keys, A. R. Abate, S. C. Glotzer, and D. J. Durian, "Measurement of growing dynamical length scales and prediction of the jamming transition in a granular material," *Nature Physics*, vol. 3, pp. 260–264, Mar. 2007.

[72] C. Donati, S. C. Glotzer, P. H. Poole, W. Kob, and S. J. Plimpton, "Spatial correlations of mobility and immobility in a glass-forming Lennard-Jones liquid," *Phys. Rev. E*, vol. 60, pp. 3107–3119, Sept. 1999.

[73] R. E. Courtland and E. R. Weeks, "Direct visualization of ageing in colloidal glasses," *J. Phys.: Cond. Matt.*, vol. 15, pp. S359–S365, Jan. 2003.

[74] E. R. Weeks and D. A. Weitz, "Properties of cage rearrangements observed near the colloidal glass transition," *Phys. Rev. Lett.*, vol. 89, p. 095704, Aug. 2002.

[75] F. P. Preparata and M. I. Shamos, *Computational Geometry: An Introduction (Monographs in Computer Science)*. Monographs in Computer Science, New York: Springer-Verlag, 1985.

[76] R. Candelier, O. Dauchot, and G. Biroli, "Building blocks of dynamical heterogeneities in dense granular media," *Phys. Rev. Lett.*, vol. 102, p. 088001, Feb. 2009.

[77] R. Candelier, O. Dauchot, and G. Biroli, "Dynamical facilitation decreases when approaching the granular glass transition," *EPL (Europhysics Letters)*, p. 24003, Oct. 2010.

[78] K. V. Edmond, M. T. Elsesser, G. L. Hunter, D. J. Pine, and E. R. Weeks, "Decoupling of rotational and translational diffusion in supercooled colloidal fluids," *In preparation*, 2011.

[79] C. Alba-Simionesco, B. Coasne, G. Dosseh, G. Dudziak, K. E. Gubbins, R. Radhakrishnan, and M. Sliwinska-Bartkowiak, "Effects of confinement on freezing and melting," *J. Phys.: Cond. Matt.*, vol. 18, no. 6, pp. R15–R68, 2006.

[80] M. Alcoutlabi and G. B. McKenna, "Effects of confinement on material behaviour at the nanometre size scale," *J. Phys.: Cond. Matt.*, vol. 17, pp. R461–R524, Apr. 2005.

[81] C. L. Jackson and G. B. McKenna, "The glass transition of organic liquids confined to small pores," *J. Non-Cryst. Solids*, vol. 131-133, pp. 221–224, June 1991.

[82] G. Barut, P. Pissis, R. Pelster, and G. Nimtz, "Glass transition in liquids: Two versus Three-Dimensional confinement," *Phys. Rev. Lett.*, vol. 80, pp. 3543–3546, Apr. 1998.

[83] D. Morineau, Y. Xia, and C. A. Simionesco, "Finite-size and surface effects on the glass transition of liquid toluene confined in cylindrical mesopores," *J. Chem. Phys.*, vol. 117, no. 19, pp. 8966–8972, 2002.

[84] C. B. Roth, K. L. McNerny, W. F. Jager, and J. M. Torkelson, "Eliminating the enhanced mobility at the free surface of polystyrene: fluorescence studies of the glass transition temperature in thin bilayer films of immiscible polymers," *Macromolecules*, vol. 40, pp. 2568–2574, Apr. 2007.

[85] C. J. Ellison and J. M. Torkelson, "The distribution of glass-transition temperatures in nanoscopically confined glass formers," *Nature Materials*, vol. 2, pp. 695–700, Sept. 2003.

[86] R. D. Priestley, C. J. Ellison, L. J. Broadbelt, and J. M. Torkelson, "Structural relaxation of polymer glasses at surfaces, interfaces, and in between," *Science*, vol. 309, pp. 456–459, July 2005.

[87] W. Kob, P. Scheidler, and K. Binder, "The relaxation dynamics of a simple glass former confined in a pore," *Europhysics Letters (EPL)*, vol. 52, no. 3, pp. 277–283, 2000.

[88] J. Schüller, Y. Mel'nichenko, R. Richert, and E. W. Fischer, "Dielectric studies of the glass transition in porous media," *Phys. Rev. Lett.*, vol. 73, pp. 2224–2227, Oct. 1994.

[89] P. A. Thompson, G. S. Grest, and M. O. Robbins, "Phase transitions and universal dynamics in confined films," *Phys. Rev. Lett.*, vol. 68, pp. 3448–3451, June 1992.

[90] K. Kim and R. Yamamoto, "Apparent finite-size effects in the dynamics of supercooled liquids," *Phys. Rev. E*, vol. 61, pp. R41–R44, Jan. 2000.

[91] A. van Blaaderen and P. Wiltzius, "Real-Space structure of colloidal Hard-Sphere glasses," *Science*, vol. 270, pp. 1177–1179, Nov. 1995.

[92] I. Snook, W. van Megen, and P. Pusey, "Structure of colloidal glasses calculated by the molecular-dynamics method and measured by light scattering," *Phys. Rev. A*, vol. 43, pp. 6900–6907, June 1991.

[93] A. Kasper, E. Bartsch, and H. Sillescu, "Self-Diffusion in concentrated colloid suspensions studied by digital video microscopy of CoreShell tracer particles," *Langmuir*, vol. 14, pp. 5004–5010, Sept. 1998.

[94] C. Donati, S. C. Glotzer, and P. H. Poole, "Growing spatial correlations of particle displacements in a simulated liquid on cooling toward the glass transition," *Phys. Rev. Lett.*, vol. 82, pp. 5064–5067, June 1999.

[95] E. R. Weeks and C. R. Nugent, "Structure of dense colloidal liquids in tight spaces," in *Reports of the Institute of Fluid Science*, vol. 19, pp. 45–49, Tohoku University, 2007.

[96] L. Berthier, "Time and length scales in supercooled liquids," *Phys. Rev. E*, vol. 69, p. 020201(R), Feb. 2004.

[97] P. Scheidler, W. Kob, and K. Binder, "Cooperative motion and growing length scales in supercooled confined liquids," *EPL (Europhysics Letters)*, vol. 59, pp. 701–707, Sept. 2002.

[98] K. L. Ngai, "Relaxation in nanometre-size polymers and glass formers: application of the coupling model to some current problems," *Phil. Mag. B*, vol. 82, pp. 291–303, Feb. 2002.

[99] J. S. Sharp and J. A. Forrest, "Free surfaces cause reductions in the glass transition temperature of thin polystyrene films," *Phys. Rev. Lett.*, vol. 91, p. 235701, Dec. 2003.

[100] G. Goel, W. P. Krekelberg, J. R. Errington, and T. M. Truskett, "Tuning density profiles and mobility of inhomogeneous fluids," *Phys. Rev. Lett.*, vol. 100, no. 10, pp. 106001–1–106001–4, 2008.

[101] H. B. Eral, D. van den Ende, F. Mugele, and M. H. G. Duits, "Influence of confinement by smooth and rough walls on particle dynamics in dense hard-sphere suspensions," *Phys. Rev. E*, vol. 80, p. 061403, Dec. 2009.

[102] S. A. Rice, "Structure in confined colloid suspensions," *Chem. Phys. Letters*, vol. 479, pp. 1–13, Sept. 2009.

[103] E. R. Weeks, J. C. Crocker, and D. A. Weitz, "Short- and long-range correlated motion observed in colloidal glasses and liquids," *J. Phys.: Cond. Matt.*, vol. 19, no. 20, 2007.

[104] S. Granick, "Soft matter in a tight spot," *Physics Today*, vol. 52, no. 7, pp. 26–31, 1999.

[105] J. Goyon, A. Colin, G. Ovarlez, A. Ajdari, and L. Bocquet, "Spatial cooperativity in soft glassy flows," *Nature*, vol. 454, pp. 84–87, July 2008.

[106] H. X. Zhou, G. Rivas, and A. P. Minton, "Macromolecular crowding and confinement: Biochemical, biophysical, and potential physiological consequences*," *Annual Review of Biophysics*, vol. 37, pp. 375–397, June 2008.

[107] T. Narumi, S. V. Franklin, K. W. Desmond, M. Tokuyama, and E. R. Weeks, "Spatial and temporal dynamical heterogeneities approaching the binary colloidal glass transition," *Soft Matter*, vol. 7, no. 4, pp. 1472–1482, 2011.

[108] H. Faxén, “Der widerstand gegen die bewegung einer starren kugel in einer zähen flüssigkeit, die zwischen zwei parallelen ebenen wänden eingeschlossen ist,” *Ann. Phys.*, vol. 373, no. 10, pp. 89–119, 1922.

[109] K. Svoboda and S. M. Block, “Biological applications of optical forces.,” *Annual review of biophysics and biomolecular structure*, vol. 23, no. 1, pp. 247–285, 1994.

[110] A. J. Archer, P. Hopkins, and M. Schmidt, “Dynamics in inhomogeneous liquids and glasses via the test particle limit,” *Phys. Rev. E*, vol. 75, p. 040501, Apr. 2007.

[111] R. P. A. Dullens and W. K. Kegel, “Reentrant surface melting of colloidal hard spheres,” *Phys. Rev. Lett.*, vol. 92, p. 195702, May 2004.

[112] K. W. Desmond and E. R. Weeks, “Random close packing of disks and spheres in confined geometries,” *Phys. Rev. E*, vol. 80, p. 051305, Nov. 2009.

[113] S. I. Henderson, T. C. Mortensen, S. M. Underwood, and W. van Megen, “Effect of particle size distribution on crystallisation and the glass transition of hard sphere colloids,” *Physica A*, vol. 233, pp. 102–116, Nov. 1996.

[114] G. Foffi, W. Götze, F. Sciortino, P. Tartaglia, and T. Voigtmann, “Alpha-relaxation processes in binary hard-sphere mixtures,” *Phys. Rev. E*, vol. 69, no. 1, p. 011505, 2004.

[115] E. Rabani, D. J. Gezelter, and B. J. Berne, “Calculating the hopping rate for self-diffusion on rough potential energy surfaces: Cage correlations,” *J. Chem. Phys.*, vol. 107, no. 17, pp. 6867–6876, 1997.

[116] B. Doliwa and A. Heuer, “Cage effect, local anisotropies, and dynamic heterogeneities at the glass transition: A computer study of hard spheres,” *Phys. Rev. Lett.*, vol. 80, pp. 4915–4918, June 1998.

[117] P. M. Reis, R. A. Ingale, and M. D. Shattuck, “Crystallization of a Quasi-Two-dimensional granular fluid,” *Phys. Rev. Lett.*, vol. 96, no. 25, 2006.

[118] E. Weeks and D. Weitz, “Subdiffusion and the cage effect studied near the colloidal glass transition,” *Chem. Phys.*, vol. 284, pp. 361–367, Nov. 2002.

[119] M. Tokuyama, “Similarities in diversely different glass-forming systems,” *Physica A*, vol. 378, pp. 157–166, May 2007.

[120] J. Mittal, J. R. Errington, and T. M. Truskett, “Thermodynamics predicts how confinement modifies the dynamics of the equilibrium Hard-Sphere fluid,” *Phys. Rev. Lett.*, vol. 96, no. 17, 2006.

[121] J. Mittal, V. K. Shen, J. R. Errington, and T. M. Truskett, "Confinement, entropy, and single-particle dynamics of equilibrium hard-sphere mixtures," *J. Chem. Phys.*, vol. 127, no. 15, p. 154513, 2007.

[122] J. Mittal, T. M. Truskett, J. R. Errington, and G. Hummer, "Layering and Position-Dependent diffusive dynamics of confined fluids," *Phys. Rev. Lett.*, vol. 100, p. 145901, Apr. 2008.

[123] E. R. Dufresne, T. M. Squires, M. P. Brenner, and D. G. Grier, "Hydrodynamic coupling of two brownian spheres to a planar surface," *Phys. Rev. Lett.*, vol. 85, pp. 3317–3320, Oct. 2000.

[124] R. P. A. Dullens and W. K. Kegel, "Topological lifetimes of polydisperse colloidal hard spheres at a wall," *Phys. Rev. E*, vol. 71, p. 011405, Jan. 2005.

[125] V. N. Michailidou, G. Petekidis, J. W. Swan, and J. F. Brady, "Dynamics of concentrated Hard-Sphere colloids near a wall," *Phys. Rev. Lett.*, vol. 102, no. 6, p. 068302, 2009.

[126] W. Kob and J. L. Barrat, "Aging effects in a Lennard-Jones glass," *Phys. Rev. Lett.*, vol. 78, pp. 4581–4584, June 1997.

[127] A. Widmer-Cooper, P. Harrowell, and H. Fynewever, "How reproducible are dynamic heterogeneities in a supercooled liquid?," *Phys. Rev. Lett.*, vol. 93, no. 13, p. 135701, 2004.

[128] J. D. Stevenson, J. Schmalian, and P. G. Wolynes, "The shapes of cooperatively rearranging regions in glass-forming liquids," *Nat Phys*, vol. 2, pp. 268–274, Apr. 2006.

[129] M. D. Haw, "Jamming, Two-Fluid behavior, and Self-Filtration in concentrated particulate suspensions," *Phys. Rev. Lett.*, vol. 92, no. 18, p. 185506, 2004.

[130] P. Poole, C. Donati, and S. Glotzer, "Spatial correlations of particle displacements in a glass-forming liquid," *Physica A: Statistical and Theoretical Physics*, vol. 261, pp. 51–59, Dec. 1998.

[131] C. J. Ellison, M. K. Mundra, and J. M. Torkelson, "Impacts of polystyrene molecular weight and modification to the repeat unit structure on the glass TransitionNanoconfinement effect and the cooperativity length scale," *Macromolecules*, vol. 38, pp. 1767–1778, Mar. 2005.

[132] P. Scheidler, W. Kob, K. Binder, and G. Parisi, "Growing length scales in a supercooled liquid close to an interface," *Phil. Mag. B*, vol. 82, pp. 283–290, Feb. 2002.

[133] B. R. Aïm and L. P. Goff, “Effet de paroi dans les empilements désordonnés de sphères et application à la porosité de mélanges binaires,” *Powder Technology*, vol. 1, no. 5, pp. 281–290, 1967.

[134] H. König, R. Hund, K. Zahn, and G. Maret, “Experimental realization of a model glass former in 2D,” *Euro. Phys. J. E*, vol. 18, pp. 287–293, Nov. 2005.

[135] P. S. Sarangapani, A. B. Schofield, and Y. Zhu, “Direct experimental evidence of growing dynamic length scales in confined colloidal liquids,” *Phys. Rev. E*, vol. 83, p. 030502, Mar. 2011.

[136] F. Fujara, B. Geil, H. Sillescu, and G. Fleischer, “Translational and rotational diffusion in supercooled orthoterphenyl close to the glass transition,” *Zeitschrift für Physik B Condensed Matter*, vol. 88, pp. 195–204, June 1992.

[137] M. T. Cicerone and M. D. Ediger, “Photobleaching technique for measuring ultraslow reorientation near and below the glass transition: tetracene in o-terphenyl,” *The J. Phys. Chem.*, vol. 97, pp. 10489–10497, Oct. 1993.

[138] M. T. Cicerone, F. R. Blackburn, and M. D. Ediger, “How do molecules move near t[sub g]? molecular rotation of six probes in o-terphenyl across 14 decades in time,” *J. Chem. Phys.*, vol. 102, no. 1, pp. 471–479, 1995.

[139] F. H. Stillinger and J. A. Hodgdon, “Translation-rotation paradox for diffusion in fragile glass-forming liquids,” *Phys. Rev. E*, vol. 50, no. 3, p. 2064, 1994.

[140] G. Tarjus and D. Kivelson, “Breakdown of the Stokes–Einstein relation in supercooled liquids,” *J. Chem. Phys.*, vol. 103, no. 8, pp. 3071–3073, 1995.

[141] J. Kim and T. Keyes, “On the mechanism of reorientational and structural relaxation in supercooled liquids: The role of border dynamics and cooperativity,” *J. Chem. Phys.*, vol. 121, no. 9, pp. 4237–4245, 2004.

[142] M. C. Ribeiro, “Translational and reorientational heterogeneity in the glass-forming liquid $ca_{0.4}k_{0.6}(no_3)_{1.4}$,” *Phys. Chem. Chem. Phys.*, vol. 6, pp. 771–774, 2004.

[143] B. Jana, D. Chakrabarti, and B. Bagchi, “Glassy orientational dynamics of rodlike molecules near the isotropic-nematic transition,” *Phys. Rev. E*, vol. 76, p. 011712, July 2007.

[144] S. Bhattacharyya, A. Mukherjee, and B. Bagchi, “Correlated orientational and translational motions in supercooled liquids,” *J. Chem. Phys.*, vol. 117, no. 6, pp. 2741–2746, 2002.

[145] G. R. Yi, V. . N. Manoharan, E. Michel, M. . T. Elsesser, S. M. Yang, and D. . J. Pine, “Colloidal clusters of silica or polymer microspheres,” *Advanced Materials*, vol. 16, no. 14, pp. 1204–1208, 2004.

[146] G. L. Hunter and E. R. Weeks, “The physics of the colloidal glass transition,” June 2011.

[147] W. van Megen and S. M. Underwood, “Change in crystallization mechanism at the glass transition of colloidal spheres,” *Nature*, vol. 362, pp. 616–618, Apr. 1993.

[148] B. Doliwa and A. Heuer, “Cooperativity and spatial correlations near the glass transition: Computer simulation results for hard spheres and disks,” *Phys. Rev. E*, vol. 61, pp. 6898–6908, June 2000.

[149] H. Sillescu, R. Bohmer, G. Diezemann, and G. Hinze, “Heterogeneity at the glass transition: what do we know?,” *J. Non-Cryst. Solids*, vol. 307-310, pp. 16–23, Sept. 2002.

[150] W. Gotze and L. Sjogren, “Relaxation processes in supercooled liquids,” *Rep. Prog. Phys.*, vol. 55, pp. 241–376, Mar. 1992.

[151] H. Sillescu, “Comment on “translation-rotation paradox for diffusion in fragile glass-forming liquids”,” *Phys. Rev. E*, vol. 53, p. 2992, Mar. 1996.

[152] L. Andreozzi, D. A. Schino, M. Giordano, and D. Leporini, “A study of the Debye - Stokes - Einstein law in supercooled fluids,” *J. Phys.: Cond. Matt.*, vol. 8, pp. 9605–9608, Nov. 1996.

[153] L. Andreozzi, A. Dischino, M. Giordano, and D. Leporini, “Evidence of a fractional Debye-Stokes-einstein law in supercooled o-terphenyl,” *Europhys. Lett.*, vol. 38, pp. 669–674, 1997.

[154] L. Andreozzi, M. Faetti, and M. Giordano, “On the scaling in the rotational dynamics of molecular probes in salol and ortho-terphenyl: a possible role of the energy landscape basins,” *J. Phys.: Cond. Matt.*, vol. 18, no. 3, pp. 931–940, 2006.

[155] I. Chang and H. Sillescu, “Heterogeneity at the glass transition: Translational and rotational Self-Diffusion,” *J. Phys. Chem. B*, vol. 101, pp. 8794–8801, Oct. 1997.

[156] S. R. Becker, P. H. Poole, and F. W. Starr, “Fractional Stokes-Einstein and Debye-Stokes-einstein relations in a Network-Forming liquid,” *Phys. Rev. Lett.*, vol. 97, no. 5, 2006.

[157] S. H. Bielowka, T. Psurek, J. Ziolo, and M. Paluch, “Test of the fractional Debye-Stokes-einstein equation in low-molecular-weight glass-forming liquids under condition of high compression,” *Phys. Rev. E*, vol. 63, p. 062301, May 2001.

[158] A. J. Moreno and W. Kob, “Dynamics of a rigid rod in a glassy medium,” *Europhys. Lett.*, vol. 67, pp. 820–826, 2004.

[159] M. Paluch, M. Sekula, S. Pawlus, S. J. Rzoska, J. Ziolo, and C. M. Roland, “Test of the Einstein-Debye relation in supercooled dibutylphthalate at pressures up to 1.4 GPa,” *Phys. Rev. Lett.*, vol. 90, p. 175702, May 2003.

[160] P. J. Yunker, K. Chen, Z. Zhang, W. G. Ellenbroek, A. J. Liu, and A. G. Yodh, “Rotational and translational phonon modes in glasses composed of ellipsoidal particles,” *Phys. Rev. E*, vol. 83, p. 011403, Jan. 2011.

[161] A. van Blaaderen, “CHEMISTRY: Colloidal molecules and beyond,” *Science*, vol. 301, pp. 470–471, July 2003.

[162] S. Adhikari, M. Selmke, and F. Cichos, “Temperature dependent single molecule rotational dynamics in PMA,” *Phys. Chem. Chem. Phys.*, vol. 13, pp. 1849–1856, 2011.

[163] S. I. Henderson and W. van Megen, “Metastability and crystallization in suspensions of mixtures of hard spheres,” *Phys. Rev. Lett.*, vol. 80, pp. 877–880, Jan. 1998.

[164] R. Kurita and E. R. Weeks, “Glass transition of two-dimensional binary soft-disk mixtures with large size ratios,” *Phys. Rev. E*, vol. 82, p. 041402, Oct. 2010.

[165] Z. Cheng, J. Zhu, P. M. Chaikin, S. E. Phan, and W. B. Russel, “Nature of the divergence in low shear viscosity of colloidal hard-sphere dispersions,” *Phys. Rev. E*, vol. 65, p. 041405, Apr. 2002.

[166] Y. S. Elmatad, D. Chandler, and J. P. Garrahan, “Corresponding states of structural glass formers,” *The J. Phys. Chem. B*, vol. 113, pp. 5563–5567, Apr. 2009.

[167] Y. Jung, J. P. Garrahan, and D. Chandler, “Excitation lines and the breakdown of Stokes-Einstein relations in supercooled liquids,” *Phys. Rev. E*, vol. 69, p. 061205, June 2004.

[168] M. Hoffmann, C. S. Wagner, L. Harnau, and A. Wittemann, “3D brownian diffusion of Submicron-Sized particle clusters,” *ACS Nano*, vol. 3, pp. 3326–3334, Oct. 2009.

[169] J. Mattsson, H. M. Wyss, A. Fernandez-Nieves, K. Miyazaki, Z. Hu, D. R. Reichman, and D. A. Weitz, “Soft colloids make strong glasses,” *Nature*, vol. 462, pp. 83–86, Nov. 2009.

[170] P. Scheidler, W. Kob, and K. Binder, “The relaxation dynamics of a supercooled liquid confined by rough walls†,” *The J. Phys. Chem. B*, vol. 108, pp. 6673–6686, May 2004.

[171] S. Lang, V. Boţan, M. Oettel, D. Hajnal, T. Franosch, and R. Schilling, “Glass transition in confined geometry,” *Phys. Rev. Lett.*, vol. 105, p. 125701, Sept. 2010.

[172] K. Watanabe, T. Kawasaki, and H. Tanaka, “Structural origin of enhanced slow dynamics near a wall in glass-forming systems,” *Nature Materials*, vol. 10, pp. 512–520, July 2011.

[173] K. Pickrahn, B. Rajaram, and A. Mohraz, “Relationship between microstructure, dynamics, and rheology in Polymer-Bridging colloidal gels,” *Langmuir*, vol. 26, pp. 2392–2400, Feb. 2010.

[174] R. Zangi, S. A. Mackowiak, and L. J. Kaufman, “Probe particles alter dynamic heterogeneities in simple supercooled systems,” *J. Chem. Phys.*, vol. 126, no. 10, p. 104501, 2007.